**Sebastian Schuh, BSc**

# Application of Blue-Light-Emitting Polyfluorene Derivatives in Solution Processed Multi Layer Devices Fabricated from Orthogonal Solvents

## MASTER THESIS

For obtaining the academic degree
Diplom-Ingenieur

Master Programme of
Technical Physics

**TU Graz**
Graz University of Technology

**Graz University of Technology**

Supervisor:

Ao.Univ.-Prof. Dipl.-Ing. Dr.techn. Emil J. W. List
Institute of Solid State Physics

in cooperation with:
NanoTecCenter Weiz Forschungsgesellschaft mbH

Graz, Juli 2012

# Acknowledgement

I would like to thank my supervisor Emil J. List for having supported my education for three years, starting with my Bachelor thesis, continuing with the opportunity of OLED research, in addition to my studies, and finally for making it possible to work on my master thesis at the NanoTecCenter Weiz.

I also want to thank Alfred Neuhold and Wolfgang Widermair for introducing me to the world of manufacturing OLEDs at the beginning of my Bachelor thesis and for all their advice and practical support.

I would also like to thank Stefan Sax, Sebastian Nau, Roman Tratting and Markus Postl for introducing me to the laboratory equipment required for the fabrication of OLEDs in the NanoTecCenter Weiz and for being available for helpful discussions. Furthermore, my thanks go to my work colleagues Peter Krabb, Markus Seidl, Johannes Kofler and Kerstin Schmoltner. Even though they were all working in other professional fields, discussions with them often helped me to understand the bigger picture when I myself couldn't see the wood for the trees. Also thanks to Alexander Blümel for investing his time in taking AFM measurements for my thesis. Herewith, my gratitude for the support of Cornelia Ranz for helping me whenever I had a question concerning chemicals.

A big thanks goes out to my girlfriend Andrea, for her support, understanding and for giving me mental strength and energy whenever necessary and finally for giving me a new home in Vienna.

Furthermore, I would like to send a thank you to England, to my friend Plum for her support in helping me to correct my "Austrian English" into British English.

Last, but by no means least, I would like to thank my family. Throughout my life, I have been fortunate enough to receive support from my parents, whatever the situation. The knowledge that they were always there for me when I needed someone to listen to me, a spiritual adviser or a place of refuge, made it possible for me to develop as a person in the way that I did. I would also like to emphasize one of the most important people in my life: my sister. Even though we are very different in many ways, with many characteristics, we could be twins. During my time in Graz she was a very important point of contact for me, but also now, since I have moved to Vienna and the possibility for us to spend time together has dramatically reduced, our relationship remains just as important and she will always be a very important person in my life.

# Abstract

Over the last few years, discernible attention has increased concerning the use of Organic Light Emitting Diodes (OLEDs). The technology of OLEDs shows great potential for them to become the most desirable technology for displays in the future. Apart from the possibility of cheap bulk production, OLED displays impress with their brightness and contrast ratio, wide viewing angle, rich color saturation and fast response time.

To perform successfully on the market, OLEDs need a long life expectancy and a high efficiency. For displaying a picture on an OLED screen, OLEDs with the emission colors red, green and blue are required. Active fluorescent and phosphorescent emitters, that emit in red and green are already well established, whereas deep blue emitting materials are still underdeveloped due to unsatisfying life expectancy and efficiency.

During the course of this thesis, two novel blue emitting polymers are investigated concerning their properties. These investigations include, inter alia, the analysis of the photoluminescence quantum yield and measurements of the photoluminescence and absorption behavior. However, the main point of this thesis is the investigation of OLEDs, especially multi layer OLEDs. By the combination of the novel polymers by already determined polymers, the target is to achieve a switch of the emission color. Another pursued objective is to increase the device efficiency and luminance values of the OLEDs by using a multi layer configuration. Due to the fact that the multi layer OLEDs are fabricated by solution based manufacturing, measurements for the determination of the resistivity (concerning dissolving) and the wettability of the individual polymer layers with regard to different solvents are performed and explained in detail.

The last chapter of this thesis deals with the topic of flexible OLEDs, where a polyester film is used as a flexible substrate. In addition, the combination of an 8 mm thick gold layer and a high conductive poly(3,4-ethylenedioxythiophene) poly(styrenesulfonate) layer is used as transparent bottom electrode. This electrode replaces the today often used material indium tin oxide, which shows a large price increase during the last few years due to the very limited deposits of indium.

# Kurzfassung

In den letzten Jahren ist ein immer größer werdendes Interesse an organischen Leuchtdioden (OLEDs) zu erkennen. Besonders der Einsatz von OLEDs in der Displaytechnologie zeigt große Fortschritte. Nicht nur auf Grund der hohen Brillanz, des großen Seitenbetrachtungswinkels und einer extrem schlanken Bauweise von OLED-Displays wird vermehrt auf diese Technologie gesetzt, auch das Potential für kostengünstige Massenproduktion trägt ihren Teil zur schnellen Entwicklung bei.

Zur Darstellung eines Bildes auf einem Bildschirm benötigt man die Farben Rot, Grün und Blau. Die Entwicklung roter und grüner fluoreszierender Farbstoffe ist bereits sehr weit fortgeschritten, wohingegen blaue Emitter noch das Problem der nicht zufriedenstellenden Effizienz und Stabilität aufweisen.

Im Zuge dieser Arbeit werden zwei neuartige blau emittierende Polymere auf ihre Eigenschaften hin untersucht. Diese Untersuchungen bestehen aus der Analyse der Photolumineszenz-Quantenausbeute, der Messung des Photolumineszenz- und Absorptionsverhaltens der Polymere in Film und in Lösung, sowie der Untersuchung der Veränderung des Emissions- und Absorptionsspektrums der Polymerfilme auf Grund thermischer Belastung oder UV-Bestrahlung. Das Hauptaugenmerk der Arbeit liegt jedoch auf der Herstellung und Untersuchung von OLEDs, im Speziellen von Mehrschicht-OLEDs. Durch die Kombination der neuartigen Polymere mit kommerziell erhältlichen Polymeren werden Ziele wie die Veränderung der Emissionsfarbe durch Veränderung des Kathodenmaterials und/oder der angelegten Spannung, sowie der Effizienz- und Helligkeitserhöhung im Vergleich zu Einschicht-OLEDs verfolgt. Da zur Herstellung der Mehrschicht-OLEDs die einzelnen Schichten durch Auftragen von in Lösungsmittel gelösten Polymeren erzeugt werden, ist besonders die Fragen nach der Benetzbarkeit der verwendeten Polymerfilme mit den entsprechenden Lösungsmitteln und das Anlösen der Filme durch das Auftragen der Lösungsmittel von großem Interesse. Messungen der Oberflächenenergien und Kontaktwinkel, sowie Untersuchungen zur Erhebung der Beschädigung der Polymerschichten durch das Auftragen der Lösungsmittel werden ausführlich erläutert.

Im letzten Abschnitt dieser Arbeit wird das Thema „flexible OLED" aufgegriffen, wobei ein Polyester-Kunststofffilm als flexibles Basismaterial dient. Ein besonderes Merkmal bei der Herstellung der flexiblen OLED ist die Verwendung der Kombination aus einer 8 nm dicken Goldschicht und einer Schicht aus hochleitendem Poly(3,4-ethylenedioxythiophene) poly(styrenesulfonate) als transparente Elektrode. Diese ersetzt das heutzutage oft verwendete Indiumtinnoxid, welches in letzter Zeit auf Grund des immer geringeren Vorkommens von Indium enorme Preiszuwächse verzeichnet.

# List of abbreviations

| | |
|---|---|
| AFM | Atomic force microscope |
| CB | Conduction band |
| EL | Electroluminescence |
| ETL | Electron transport layer |
| FEMO | Free electron molecular orbital |
| HC-PEDOT:PSS | High conductive poly(3,4-ethylenedioxythiophene) poly(styrenesulfonate) |
| HOMO | Highest occupied molecule orbital |
| HTP | Copolymere with hole transport characteristic (equal amounts of poly(indenofluorene) and triphenylamine based units in its backbone) |
| ISC | Inorganic semiconductor |
| ITO | Indium tin oxide |
| IV characteristic | Current-voltage-luminance characteristic |
| LUMO | Lowest unoccupied molecule orbital |
| MEHPPV | Poly[2-methoxy-5-(2'-ethyl-hexyloxy)-1,4-phenylene vinylene] |
| OLED | Organic light emitting diode |
| OSC | Organic semiconductor |
| PEDOT:PSS | Poly(3,4-ethylenedioxythiophene) poly(styrenesulfonate) |
| PEG | Polyethylene glycol |
| PEGPIF | PEGylated polyfluorene |
| PF | Polyfluoren |
| PIF | Poly(indenofluoren) |
| PL | Photoluminescence |
| rpm | Rotations per minute |
| RVP | Rotary vane pumpe |
| SI | Système international d'unités (International System of Units) |
| TFT | $\alpha,\alpha,\alpha$-trifluorotoluene |
| TMP | Turbomolecular pump |
| TPBi | 1,3,5-tri(phenyl-2-benzimidazole)-benzene |
| VB | Valence band |
| VDU | Vapor deposition unit |

# Table of contents

# 1 Introduction

In 1967, Mehl and Funk published a paper on the topic of *" Dark injection of electrons and holes and radiative recombination in anthracene with metallic contacts: A sodium-potassium alloy makes an electron injecting contact to anthracene, evaporated gold forms a hole injecting contact. The simultaneous injection of electrons and holes leads to radiative recombination at room temperature"*. [1] Already two years before, Helfrich and Schneider reported on recombination radiation in anthracene crystals, but utilizing electrolytes as contacts in contrast to Mehl and Funk. [2] In 1977 a paper with the title *"Electrical Conductivity in Doped Polyacetylene"* was published by H. Shirakawa, et al. [3]. This discovery can be regarded as the beginning of the rapid development of organic semiconductor technology and was awarded with a Nobel prize. [4] In 1987 C.W. Tang et al. reported on the first thin film organic light emitting diodes (OLEDs) based on small molecules, which showed green emission. [5] Three years later, the first light emitting diode based on conjugated polymers (PLEDs) was presented by Friend et al. [6] Since that scientists all over the world made and still make a lot of efforts concerning the development of different applications of organic semiconductors such as OLEDs, organic field effect transistors (OFET), organic solar cells and many more. Today's display market is mainly represented by liquid crystal device (LCD) and plasma monitors. The technology of OLEDs shows a high potential to be the most used in technology for displays in future. Beside the possibility of cheap bulk production, like roll-to-roll processing or inkjet printing, OLED displays impress with their high brightness and contrast ratio, wide viewing angle, rich color saturation and a fast response time. The possibility of using bendable substrates opens up new possibilities too, so that for example buying a flexible television screen will soon become a reality. In the future when the use of filament lamps is forbidden and the disposal of energy saving lamps containing mercury are not tackled completely, OLEDs are also potential candidates for solid state lightning applications. In contrast to a Planckian radiator like a filament lamp, an OLED shows a much more narrow emission spectrum why it is not possible to create white light with only one OLED. By the combination of three OLEDs with the emission colors red, green and blue one can generate every color (including the achromatic color white) just by changing the emission intensities of the individual OLEDs. This technique for the creation of different colors is also used for the visualization of a picture by a monitor, where the pixels of the display are divided into red, green and blue subpixels. To perform successfully on the market, a long life expectancy (in excess often thousands of hours) and an as high as possible efficiency of OLEDs is required. Active fluorescent and phosphorescent emitters that emit in the red and green are already well established, whereas deep blue emitting materials are still underdeveloped due to unsatisfying life expectancy and efficiency. [7] Nevertheless, first commercial OLED-based products are already on the market. 2008, Sony presented the first OLED-TV XEL, also many manufacturers of panels for cell- and smart-phones already rely on OLED displays. So for example Samsung produces about 30 million panels per month. Despite this first success of OLED-based products, the research for materials with higher stability, higher device efficiency

and easier methods of synthetization goes on to prevail this technology on the market in the long term.

With regard to research of new synthesized conjugated polymers with an emission color in the blue spectral region, this thesis investigates two novel polyfluorene-type polymers and their applications in multi layer devices. In the following a short overview about the chapters of this thesis will be given.

In chapter 2, fundamentals about organic semiconductors (OSC) are discussed. At the beginning, the theory of conjugated systems and required basic knowledge concerning this topic is presented, followed by an explanation of the electrical properties of OSC. Moreover an overview about the excited states and excitation and recombination processes within OSCs is given.

Chapter 3 deals with the working principle of OLEDs including the assembly of an OLED and the descriptions of the function of the individual layers. Afterwards the more complex working principle of multi layer OLEDs is discussed. In this respect, different possibilities for an enhancement of the device efficiency by using the concept of multi layer OLEDs, are presented.

Chapter 4 deals with the topic of experimental methodology, including the preparation of the different layers of an OLED, as well as the characterization and determination of the properties of the assembled OLEDs, polymer films and polymer solutions. Furthermore an overview about the methods of measurements for the determination of the resistivity (concerning dissolving) and the wettability of the individual polymer layers with regard to different solvents is shown.

Chapter 5 discusses the measurements results of the assembled single and multi layer systems. In the first instance, the new synthesized conjugated polymers (fluorinated polyfluorene and PEGylated polyfluorene) are used as active layers in a single layer configuration, where different processing parameters are optimized to reach an as high as possible device efficiency of the single layer OLEDs. For the manufacturing of multi layer OLEDs, fluorinated polyfluorene is combined with a red emitter with the target to cause a color switch of the emission color between blue and red by changing the applied voltage and the used electrode materials. A further experiment is the combination of the fluorinated polyfluorene with a blue emitting polymer with hole transport characteristic to reach an enhancement of the device efficiency. When investigating PEGylated polyfluorene in a multi layer configuration, the PEGylated polyfluorene is combined with a blue emitting poly(indenofluoren)-based polymer again with the target to reach an enhancement of the device efficiency.

Chapter 6 gives attention to flexible OLEDs by introducing polyester films as substrates. In addition, the combination of an 8 mm thick gold layer and a high conductive Poly(3,4-ethylenedioxythiophene) poly(styrenesulfonate) layer (HC-PEDOT:PSS) is used as the transparent bottom electrode instead of the often used indium tin oxide. In order to compare the

conductivity of the bottom electrode, the results of flexible OLEDs with indium tin oxide and with HC-PEDOT:PSS as bottom electrodes are listed too.

# 2  Organic semiconductors

## 2.1  Fundamentals

The discovery of inorganic semiconductors (ISC) and their applications had an enormous impact to the economic development. Our modern civilization is not conceivable without the use of ISCs. In recent years, more and more electronics manufacturers focus on the use of organic semiconductors (OSC) in their products. The semiconducting behavior of the organic compounds originates in the special structure of this class of materials. To understand the electronic and optical properties of OSC, one has to be familiar with some basics of atomic and molecular physics. In the follows, a short introduction to the most important topics, necessary for the explanation of OSC, are shown.

### 2.1.1  Atomic structure and quantum mechanical description

Atom, deduced from the Greek word *átomos*, stands for indivisibility, because the ancient Greeks proceeded on the assumption that atoms are the smallest units which are the basic modules of matter. Today it is well known that an atom is divided into an atomic shell that comprises of negatively charged electrons and an atomic nucleus, made of positively charged protons and neutral neutrons. Protons and neutrons can be divided further into up and down quarks, but this consideration would go too much into detail. Due to electromagnetic forces, the electrons are bound to the nucleus. An often used model for the description of the atomic shell configuration is the so called shell model, which assumes that the electrons orbit the nucleus on different shells which are arranged like the rings of an onion. The shells represent zones of electrons with similar energies, where the shell number indicates the energy of the electrons. The innermost shell, which can accept two electrons, is filled first, followed by the outer shells that can accept eight electrons in each case. To take carbon, for instance, the nucleus consists of eight protons and because the whole atom is neutral, the atomic shell contains eight electrons. For the innermost shell this means that it is completely filled, in the second shell, six of eight possibilities are occupied. Electrons in the outermost shell are called the valence electrons. They are crucial for the chemical properties of an atom because the valence electrons are involved in chemical bonding. With the shell model, many properties and behaviors of atoms and molecules can be explained, but this model also has flaws. For example, some spatial shapes of molecules cannot be explained with the shell model. In these cases, one is dependent on using the atomic orbital model. In contrast to the shell model whereat the electrons orbit the nucleus on different shells, the orbitals represent the spatial shape of probability to meet an electron there. The orbitals have circular, dumbbell-shaped, double dumbbell-shaped or rosette-shaped forms. The classification of the orbitals is founded on four quantum numbers:
The main quantum number $n$ describes the main energy state of an electron. One can say that it is the equivalent to the shell number of the shell model. Consequently, the higher the number is, the

bigger the distance between the nucleus and electron and the higher the potential energy. The range of $n$ starts at one and rises in integer steps $(n = 1, 2, 3, ...)$.

The azimuthal quantum number $l$ labels the angular momentum of the electron and is accountable for the shape of the orbital. The range of values is $l = 0, 1, ..., (n-1)$.

The magnetic quantum number $m_l$ describes the spatial orientation of the orbital and ranges from $m_l = -l, (-l+1), ..., (l-1), l$.

The last quantum number is the spin quantum number $m_s$, which determines the spin orientation of the electron. $m_s$ can take two values, +1/2 and -1/2.

In Figure 2.1 the shapes of the orbitals with a main quantum number $n = 1, ..., 4$ and all combinations of the other quantum numbers are shown.

| | s ($l$=0) | p ($l$=1) | | | d ($l$=2) | | | | | f ($l$=3) | | | | | | |
|---|---|---|---|---|---|---|---|---|---|---|---|---|---|---|---|---|
| | m=0 | m=0 | m=±1 | | m=0 | m=±1 | | m=±2 | | m=0 | m=±1 | | m=±2 | | | m=±3 |
| | s | $p_z$ | $p_x$ | $p_y$ | $d_{z^2}$ | $d_{xz}$ | $d_{yz}$ | $d_{xy}$ | $d_{x^2-y^2}$ | $f_{z^3}$ | $f_{xz^2}$ | $f_{yz^2}$ | $f_{xyz}$ | $f_{z(x^2-y^2)}$ | $f_{x(x^2-3y^2)}$ | $f_{y(3x^2-y^2)}$ |
| n=1 | | | | | | | | | | | | | | | | |
| n=2 | | | | | | | | | | | | | | | | |
| n=3 | | | | | | | | | | | | | | | | |
| n=4 | | | | | | | | | | | | | | | | |

Figure 2.1: Shapes of the atomic orbitals depend on the quantum numbers $n$, $l$ and $m_l$ (taken from [8]).

Due to the Pauli Exclusion Principle, which says that two identical electrons cannot occupy the same quantum state simultaneously, the maximal number of electrons in an orbit is two, one electron with spin up and one electron with spin down.

To explain how one can calculate the shape of the orbitals, one has to make a short excursion to quantum mechanics. In 1924, Louise de Broglie postulated that massive particles (like electrons) also exhibit a wave character. In quantum mechanics every particle can be explained by its wave function, which is a solution of the time independent Schrödinger equation

$$H \Psi(x) = E \Psi(x) \; .$$ (1)

$H$ is the Hamiltonian operator, $E$ the energy eigenvalue and $\Psi(x)$ the time independent wave function. Calculating the absolute square of the wave function, represents the probability density of the particle that, in turn, defines the shape of the orbital. The question arises, what happens with the orbital shapes of two individual atoms if they form a chemical compound. In theory one just has to define the appropriate Hamiltonian for this quantum mechanical system and solve the

Schrödinger equation (1). Due to the complexity of this arithmetic problem an analytical solution cannot be found and it is necessary to use approximation procedures like the molecular orbital theory.

## 2.1.2 Molecular orbital theory

The molecular orbital theory was developed primarily by Friedrich Hund and Robert Mulliken in 1928 for the calculation of molecule orbitals. The idea was to use a linear combination of atomic orbitals (LCAO) to represent molecular orbitals involving the whole molecule. As a simplification, only the electrons of the outermost shells are used as the electrons of the total system. [9]

The molecular orbital theory will now be explained in more detail with help of the $H_2$-molecule as an example.

As starting point one has to consider two independent hydrogen atoms, where the eigenfunctions of the individual atoms are called $\psi_A$ and $\psi_B$. Bringing the atoms closer together leads to an overlap of the orbitals and as an simple approximation, the molecular orbital wavefunction is approximated by the linear combination

$$\Psi = c_A \psi_A + c_B \psi_B .$$

(2)

The constants $c_A$ and $c_B$ consider the influence of the atomic eigenfunctions to the molecular orbital wavefunction. Due to the fact that both atoms are identical, the constants must have the same absolute value, but can differ in their signs.

The approximation of the molecular orbital wavefunction can also be written in the general form

$$\Psi = \sum_{i=1}^{n} c_i \psi_i ,$$

(3)

where $n$ is the number of atoms that are involved into the formation of the molecular orbital.

Coming back to the example of the $H_2$-molecule, the electron probability density is achieved by calculating the absolute square of equation (2). This leads to the equation

$$\left| \Psi^2 \right| = \left( c_A \psi_A \right)^2 + \left( c_B \psi_B \right)^2 + 2 c_A \psi_A c_B \psi_B .$$

(4)

Depending on the signs of $c_A$ and $c_B$, the expression $2 c_A \psi_A c_B \psi_B$ is positive or negative, leading to two solutions of equation (4). If $c_A$ and $c_B$ are either positive or negative, the orbitals of the two hydrogen atoms have the same sign and an overlap of the atom orbitals leads to a higher electron probability density between the two hydrogen atoms. Due to the attracting effect of the electrons to the positive charged nucleus, the energy level of the formed molecule orbital is lower

(difference $E_\sigma$) compared to the atomic orbitals of the hydrogen atoms ($1s_H$) and is called the bonding molecular orbital ($\sigma_{H\text{-}H}$; see Figure 2.2).
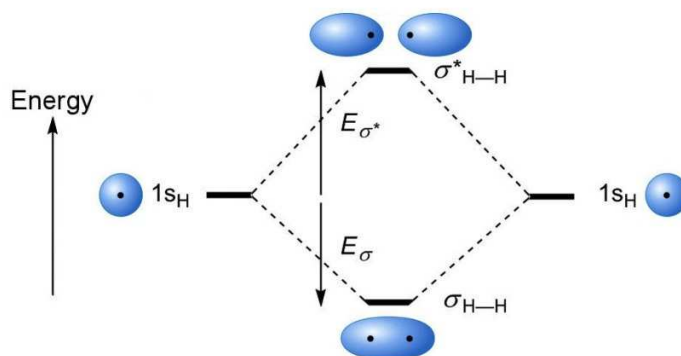


Figure 2.2: Atomic and molecular orbitals and energy levels of atomic and molecular hydrogen (taken from **[10]** and **[11]** and modified).

On the other side, when $c_A$ and $c_B$ have opposite signs, the overlap of the atom orbitals leads to the molecular orbital $\sigma^*_{H\text{-}H}$, which has a nodal plane between the two nucleuses where the electron probability density is zero. The energy level of the $\sigma^*_{H\text{-}H}$ orbital is higher compared to the atomic orbitals $1s_H$ of hydrogen atoms (difference $E_{\sigma^*}$), due to lower electron probability density between the nucleus and the resulting enhanced repulsion of the nucleus. The $\sigma^*_{H\text{-}H}$ orbital is called the antibonding molecular orbital. [10]

Whether the formation of a molecule is energetically favorable, is determined by the energy levels of the formed molecular orbitals, and if they are occupied or not occupied. In the case of hydrogen, the electrons of the two hydrogen atoms occupy the bonding $\sigma_{H\text{-}H}$ orbital, the energy is lowered and a molecule is formed. When doing the same consideration for helium, one can see that the formation of a helium molecule is not favorable. Due to the fact that the four electrons of the two helium atoms occupy the bonding and also the antibonding molecule orbital, the total energy is higher compared to energy of the helium atoms ($|E_\sigma| < |E_{\sigma^*}|$). As a result it is not possible to determine helium molecules in nature.

## 2.1.3  Different types of chemical bonding

Noble gases, like argon or neon, are nonreactive elements that appear monoatomic. A characteristic of noble gases is their fully filled outermost shell. The low reactivity concerning chemical reactions is an indication that this behavior exhibits an energetically favorable state, which corresponds to a minimum of the total energy. The physicist, Walter Kossel and the physical chemist Gilbert Lewis expected that atoms of other elements also aspire noble gas configuration (also known as the octet rule [12]) and try to reach this configuration by forming chemical compounds. [13] Generally one distinguishes between three types of chemical bonding:

ionic bonding, covalent bonding and metal bonding. Between these types of bonding, transitional forms exist.

**Ionic bonding**

The ability of an atom to attract electrons can be described by the so called electronegativity. Atoms with a low electronegativity release electrons from the outermost shell easily, in contrast to this, atoms with high electronegativity accept electrons effortlessly. Bringing two atoms with big differences in their electronegativity together causes the atom with the low electronegativity to release an electron to the other atom. After releasing the electron, the atom is charged positive, the electron receiving atom achieves a negative charge. Due to electrostatic forces, both charged atoms get bound together. This type of bonding is called heteropolar bonding, which is also known as ionic bonding. A well-known representative for ionic bonding is sodium chloride. Chloride, an element with seven valence electrons, collects the electron released from the sodium atom and therefore reaches noble gas configuration. Also sodium, which has one electron in its outer shell, achieves the favored noble gas configuration when releasing an electron.

**Covalent bonding in atoms and molecules**

In the case of ionic bonding, atoms try to reach noble gas configuration by releasing or collecting electrons. When considering the covalent bonding, the binding partners also attempt to achieve noble gas configuration, but in this case no electron exchange takes place, the target is achieved by the sharing of valence electrons. For a more detailed explanation, one considers the chloride molecule $Cl_2$. The chloride atom has, as already mentioned, seven valence electrons. Bringing two Cl-atoms closer together, atomic orbitals of the Cl-atoms start to overlap. As a result of this overlap, both Cl-atoms can reach noble gas configuration by "lending" an electron to each other. The shared electrons, which are also called binding electron pair, are responsible for the bonding, because these electrons, which are located between the nucleuses, are attracted by both nucleuses. In addition, the electron pair is responsible for reciprocal shielding of the nucleus, so that the repulsion of the nucleus is decreased. All in all, that results in a force which leads to a binding of the Cl-atoms.

In chapter 2.2, two particular types of covalent bonds will be used for the explanation of the behavior of organic semiconductors, the so called $\sigma$-bond and $\pi$-bond. If the bond has a rotational symmetry with respect to the bond axis, it is called $\sigma$-bond. The condition of rotational symmetry is fulfilled, if the two overlapping orbitals are two s-orbitals, an *s*- and *p*-orbital or two *p*-orbitals (left side of Figure 2.3). If two *p*-orbitals have the same spatial orientation and the symmetry axis of the *p*-orbitals is perpendicular to the bond axis, an overlap leads to the formation of a $\pi$-bond. Looking at the right side of Figure 2.3, one should not misinterpret that two bonds have formed. The probability to meet an electron at the nucleus connecting axis is zero, so the $\pi$-bond is only one bond with two orbital lobes.
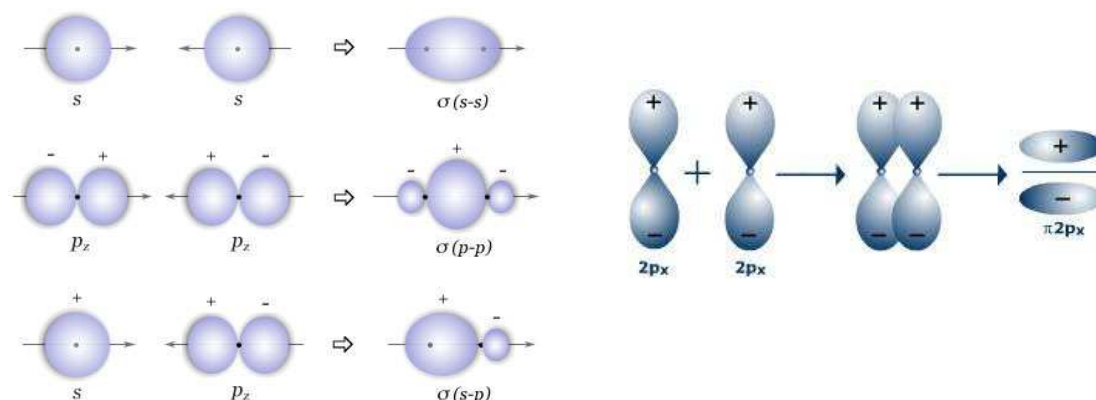
Figure 2.3: Left: three types of $\sigma$-bonds formed by overlapping of two *s*-orbitals, an *s*- and *p*-orbital or two *p*-orbitals (taken from [14]); right: $\pi$-bond formed by the overlap of two *p*-orbitals (taken from [15]).

**Metal bonds**

In metals, every atom delivers its valence electron(s), thereby becoming a positive charged metal ion. The ions build a crystal lattice, the electrons move almost freely between the ions and form the so called electron gas. Due to the electrostatic forces between the ions and the electron gas, the whole metal crystal is held together. Typical characteristics of metal, like electric conductivity, conduction of heat, metallic gloss or ductility can be explained by the model of electron gas.

## 2.2 Conjugation and hybridization

As already mentioned at the beginning of this chapter, the semiconducting behavior of OSC originates in the special structure of this class of materials. OSC, whether they are small molecules or long chained polymers, are mainly composed of carbon. A crucial feature that has an enormous influence to the behavior of the OSC, is the occurrence of so called conjugated double-bonds. This describes an alternating sequence of double-bonds and single-bonds between the carbon atoms. Examples of molecules containing conjugated double-bonds can be seen in Figure 2.4.



Figure 2.4: Examples of molecules containing conjugated double-bonds; left: polyacetylene; right: pentacene (taken from [16] and [17] and modified).

Another example of a molecule containing a conjugated double-bond is benzene. It consists of six carbon atoms arranged in a ring, whereas every carbon atom is linked to a hydrogen atom too. For the linkage between two elements, half occupied orbitals are needed to enable an overlap. As depicted in Figure 2.5 on the left side, carbon has two half occupied *p*-orbitals. Only two bondings with other elements are therefore possible, but a carbon atom in benzene is linked to two carbon atoms and one hydrogen atom. To enable the possibility of this third linkage, an electron from the *2s*-orbital has to be lifted to an unoccupied *2p*-orbit by the expansion of energy (middle of Figure 2.5). After this process, two *2p*-orbits and one *2s*-orbit form three *sp$^2$*-orbits by obtaining energy (right side of Figure 2.5). The whole process is called *sp$^2$*-hybridization [12]. The chemical structure and an enlarged presentation of the hybrid orbitals of benzene are shown in Figure 2.6.
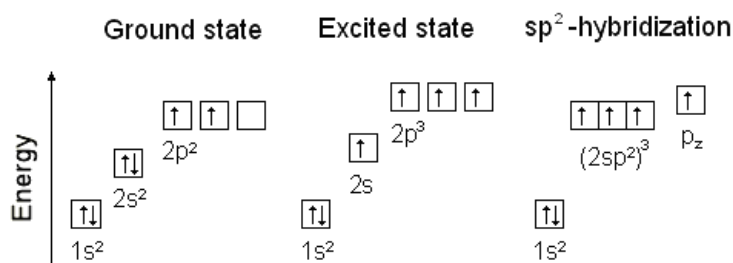


Figure 2.5: Left: electronic configuration of carbon in the ground state; middle: excitation of an electron from a *2s*-orbit to a *2p*-orbit by expending energy; right: formation of three *sp$^2$*-orbits by obtaining energy (taken from **[18]**).
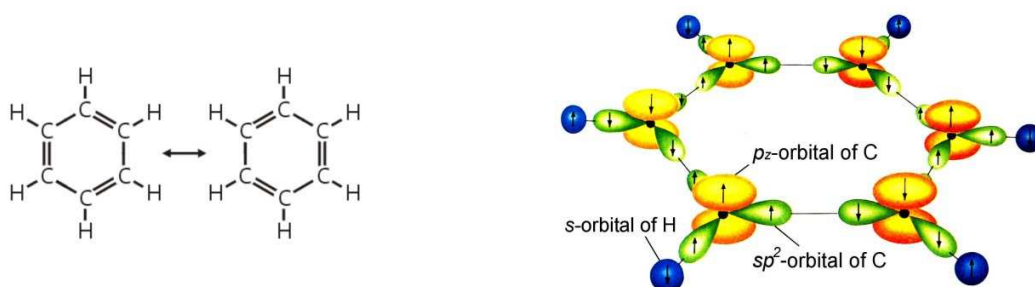


Figure 2.6: Left: chemical structure of benzene; right: enlarged presentation of hybrid orbitals of benzene (taken from **[19]** and **[12]** and modified).

The binding between the carbon atoms in benzene goes along with the overlap of the *sp$^2$*-orbitals that causes the formation of $\sigma$(C-C)-bonds between the carbon atoms. Furthermore, the overlap of the *sp$^2$*-orbitals of the carbon atoms and the *s*-orbitals of the hydrogen atoms forms $\sigma$(C-H)-bonds. As a result of the bonding between the six carbon and six hydrogen atoms, the ring-shaped benzene molecule is formed. The ring form in turn leads to an approach of the *p$_z$*-orbitals so that they are able to overlap and to form $\pi$-bonds. In a thought experiment one can allocate the carbon

atoms numbers from one to six. Due to the overlap of the $p_z$-orbitals, $\pi$-bonds can be formed between the carbon atoms one and two, three and four, five and six, but at the same time it is possible to say, that the $\pi$-bonds can be formed between the carbon atoms two and three, four and five, six and one. In Quantum mechanics, the carbon atoms are identical and it is not possible to number them, so that the six $\pi$-electrons cannot be allocated to the particular carbon atoms. The consequence is that the probability density of the $\pi$-electrons ranges over the whole molecule. The result is a so called delocalized $\pi$-orbital, or more precisely, a system of delocalized $\pi$-orbitals. As explained in chapter 2.1.2 about the molecular orbital theory, the result of the overlap of two atomic orbitals is the formation of a bonding and antibonding molecule orbital. In the case of benzene, the overlap of the three $p_z$-orbitals overlap leads to the formation of six molecular orbitals, three bonding ($\pi_1$, $\pi_2$, $\pi_3$) and three antibonding ($\pi_4$, $\pi_5$, $\pi_6$) molecule orbitals (see Figure **2.7**). The six $\pi$-electrons completely fill the three bonding orbitals. The molecular orbitals $\pi_2$, $\pi_3$ have the same energy and are called the **H**ighest **O**ccupied **M**olecular **O**rbitals (HOMO). The molecular orbitals $\pi_4$ to $\pi_6$ are unoccupied, $\pi_4$ and $\pi_5$, which have the same energy, are called the **L**owest **U**noccupied **M**olecular **O**rbitals (LUMO). If the energy gap between HOMO and LUMO levels reaches values within the range of 1 to 3 eV, semiconducting behavior results. In this content, one is not allowed to hide the fact, that also during the formation of the $\sigma$-bonds, bonding and antibonding molecular orbitals are formed, where only the bonding orbitals are occupied. Due to the fact, that the energy level of the bonding $\sigma$-orbitals is lower than the energy level of the $\pi_1$-orbital and the energy level of the antibonding $\sigma$-orbitals is higher than the energy level of the $\pi_6$-orbital, the $\sigma$-bonds have no influence to the HOMO and LUMO level of the benzene molecule.
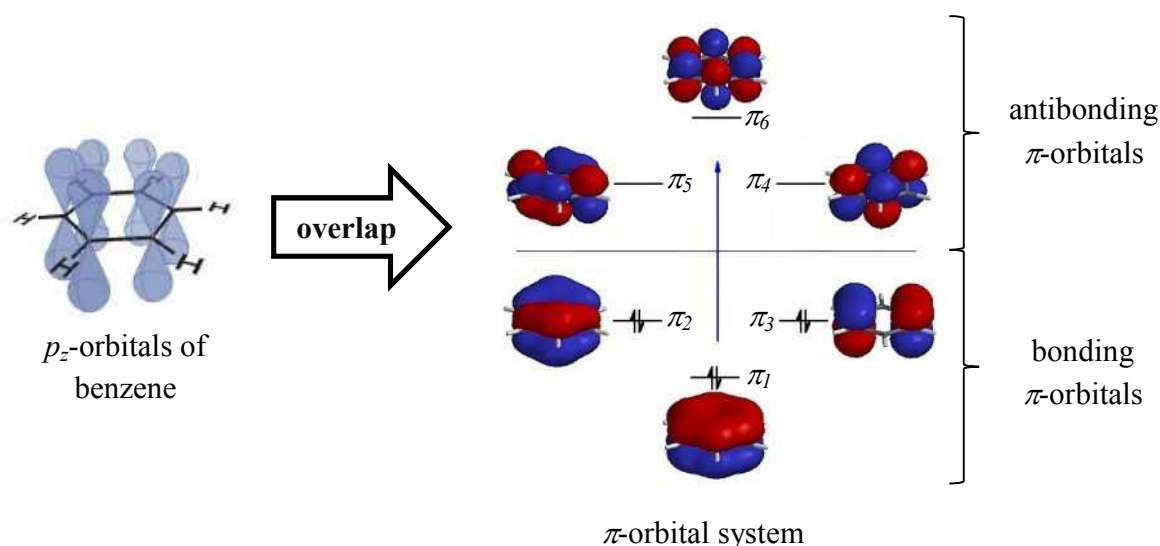


Figure 2.7: The overlap of the $p_z$-orbitals of benzene leads to the formation of three bonding ($\pi_1$, $\pi_2$, $\pi_3$) and three antibonding ($\pi_4$, $\pi_5$, $\pi_6$) molecular orbitals, where the bonding $\pi$-orbitals are fully occupied by the six $\pi$-electrons (taken from **[19]** and **[20]** modified).

Due to the conjugation and the formation of a system of delocalized $\pi$-orbitals, a stabilization of the molecule can be achieved. The reason is that the energies of the electrons in the delocalized $\pi$-orbital are decreased compared to the system where the electrons are arranged in localized orbitals. [12] This behavior can be explained by the free electron molecular orbital, which will be discussed in the following chapter.

## 2.3 Formation of band gaps and influencing factors

In purely quantitative terms, the formation of a band gap was described with the molecular orbital theory and the definition of the HOMO and LUMO level in the previous chapter. In the following, the model of free electron molecular orbital (FEMO) will be used for a simple approximation to explain the occurrence of band gaps of molecules containing conjugated double bonds in a mathematical way. An additional approach will be given, where the existence of a band gap will be explained by the Peierls transition. The Peierls transition is also used for the explanation of a band gap of molecules with very long conjugated carbon chains, where the FEMO model would predict the disappearance of the band gap. Finally, influencing factors to the band gap will be discussed.

### 2.3.1 FEMO model - a simplified quantum mechanical picture

In Figure 2.8 on the left side, the one-dimensional potential distribution of a series of carbon atoms with periodic distance in between is shown. The first step of the FEMO model is to simplify the shape of the potential distribution. Making this simplification, the potential "inside" the molecule is assumed as zero and "outside" of the molecule is assumed as infinitely high. The simplification certainly can be justified for electrons in the $\pi$-orbital, which are delocalized over the whole molecule. This leads to a simplified quantum mechanical picture: the electron in a box.
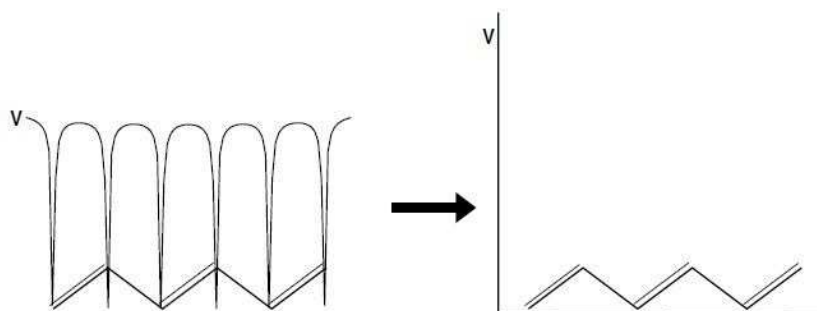


Figure 2.8: FEMO-model: simplification of the potential in the molecule (taken from [21]).

As already mentioned in chapter 2.1, in quantum mechanics, electrons can be described via its wave functions. By the formulation of this wave function and the definition of the Hamiltonian for the particular quantum mechanical system, one can calculate the energy-eigenvalues of the system by solving the Schrödinger equation (1). The result of the calculation, as shown in [21], is

$$E_n = \frac{h^2}{8m_e L^2} n^2, \quad n \in \aleph,$$
(5)

where $h$ is the Planck constant, $m_e$ the mass of the electron, $L$ the length of the box (potential well) and $n$ is a quantum number. One notices immediately that the energy values (depending on the quantum number $n$) are not continuous but discrete. The result of the calculation can be applied to explain the electronic behavior in delocalized $\pi$-orbitals, for example the $\pi$-orbital system of benzene. When using the FEMO-model for highly symmetrical molecules and planar molecules like benzene, one has to choose a two-dimensional squared potential well for the calculation instead of a one-dimensional potential well that is used for elongate molecules. Solving the Schrödinger equation (1) for this system, one achieves a similar equation for the energy levels compared to equation (5), but with an additional quantum number $m$ due to the usage of the two-dimensional potential.

$$E_{nm} = \frac{h^2}{8m_e L^2} \left( n^2 + m^2 \right), \quad n, m \in \aleph.$$
(6)

A consequence of the additional quantum number $m$ is the occurrence of degenerated energy levels. For example the calculated energy for $n = 1$ and $m = 2$ is the same than calculating the energy for $n = 2$ and $m = 1$. Due to the principle of Pauli, every quantum mechanical state with the energy level $E_{nm}$ can be occupied by two electrons, one with spin up and one with spin down. Consequently, the six $\pi$-electrons of benzene occupy the states with the corresponding energy levels $E_{11}$, $E_{12}$ and $E_{21}$. $E_{12}$ and $E_{21}$, which have the same energy, represent the HOMO energy level of benzene. The next energy level $E_{22}$ is unoccupied and presents the energy level of the HOMO. In contrast to the graphical view of the $\pi$-orbital system in Figure 2.7, $E_{22}$ is not degenerated. This discrepancy can be explained as a subsequent error due to the severe simplification when using a squared potential well as an assumption for the probability density of the delocalized $\pi$-electrons, but to gain an overview, this calculation is quite useful.

In a concluding example, the FEMO-model is used for the calculation of the size of beta-carotene, a molecule with 11 conjugated double bonds (see Figure 2.9). Due to the elongate shape of the molecule, the one-dimensional potential well has to be used for the FEMO calculation. The measured absorption spectrum of beta carotene shows a maximum at 450 nm. With this value it is possible to make a very general approximation of the energy difference between the LUMO and HOMO level by the equation

$$\Delta E_{LUMO-HOMO} = h \frac{c}{\lambda_{ABS-\max}}, \qquad (7)$$

where $h$ is the Planck constant, $c$ the vacuum speed of light and $\lambda_{ABS-max}$ the wavelength at the absorption maximum of beta carotene. The system of delocalized $\pi$-orbitals of beta carotene contains 22 $\pi$-electrons as a consequence of the 11 conjugated double bonds. Due to this, the quantum mechanical states with the corresponding energy levels $E_1$ to $E_{11}$ are occupied. $E_{11} = E_{HOMO}$ is the energy level of the HOMO and $E_{12} = E_{LUMO}$ the energy level of the LUMO. Applying equation (5), the energy difference between the LUMO and HOMO level can also be calculated with

$$\Delta E_{LUMO-HOMO} = \frac{h^2}{8m_e L^2}\left(n_{LUMO}^2 - n_{HOMO}^2\right) \quad , \quad n \in \aleph. \qquad (8)$$

By equalizing equation (7) and (8), it is possible to calculate the size $L$ of the potential well, which is an assessment for the size of the beta carotene molecule. Doing the calculation, a size of $L$=17,7 Å results, which is the right order of magnitude compared to the real size of the molecule. [22]
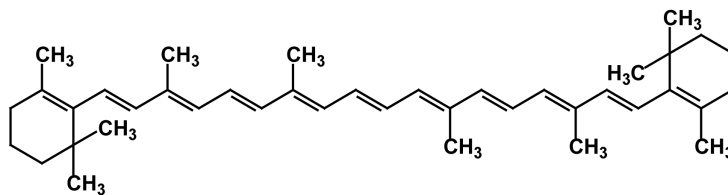


Figure 2.9: Structural formula of beta-carotene (taken from **[23]**).

When considering again equation (8), one can see that the longer the conjugated polymer is, the smaller is the size of the band gap. In limiting case of very long conjugated polymers, the FEMO model would predict the disappearance of the band gap. Due to the fact that experimental data do not correspond with this prediction, a modification of the model has to be done, that is shown in the next chapter. [9]

## 2.3.2 Formation of band gap due to Peierls transition

Rudolf Peierls asserted in the 1930s that a one dimensional chain of metal atoms with one electron per ion is more stable, if the distances of the atoms alternate between long and short distances instead of being arranged equally spaced. [24] If the metal atoms are equally spaced and every atom delivers one electron to the electron gas, the dispersion relation shows a half filled band (see left side of Figure 2.10). In this case one obtains a metallic behavior. A lattice

deformation that leads to a alternation of the distances between the atoms (as shown in the middle of Figure 2.10), causes a formation of a band gap at the wave vector value $k = \pi/(2a)$. Now all states between the $k$-values $0$ and $\pi/(2a)$ are occupied, the states above $k = \pi/(2a)$ are not filled. Taking a closer look to the $k$-values, which are a little bit smaller than $\pi/(2a)$ (see right side of Figure 2.10), one can see, that this occupied $k$-values correspond now to a bit lower energies compared to the dispersion relation on the left side of Figure 2.10. Finally, this arrangement of atoms has a lower total energy and is therefore preferred. [25]

The change of the periodicity has also another effect. As said before, the band below the band gap is fully filled, the band above is empty. Depending on the gap size, the change of the lattice period leads from a metallic to a semiconducting or isolating behavior.
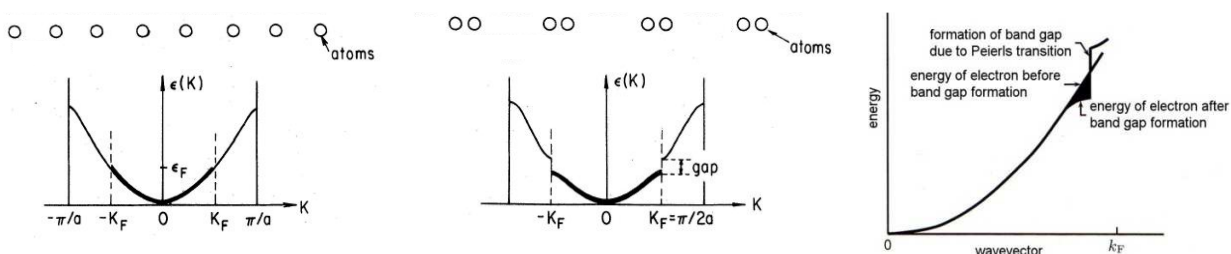


Figure 2.10: Left: dispersion relation of a chain of equally spaced metal atoms with period $a$, where every atom delivers one electron to the electron gas leading to a half filled band; middle: dispersion relation of metal atom chain with alternating distances between the atoms, resulting in a band gap at the wave vector value $\pi/(2a)$; right: decrease of the total energy due to lower energies of occupied states with $k$-values in the region of $\pi/(2a)$. (taken from **[26]** and **[24]** and modified).

A Peierls transition can also be found in conjugated polymers, for example polyacetylene (see Figure 2.4). The polymer has one conduction electron per carbon atom. Without a lattice distortion, the polymer would have a half filled band that would lead to a metallic behavior. Due to the fact that carbon atoms which are bound together by double-bonds are closer than the carbon atom which are bound by single-bonds, a distortion results, leading to a band gap of about 1,5 eV, so that polyacetylene is a semiconductor. [24]

### 2.3.3  Influences on the band gap

The size of the band gap can be influenced by several factors like the bond length alternation (as shown before), the resonance energy, the torsion of the molecule and the presence of substituents [27].
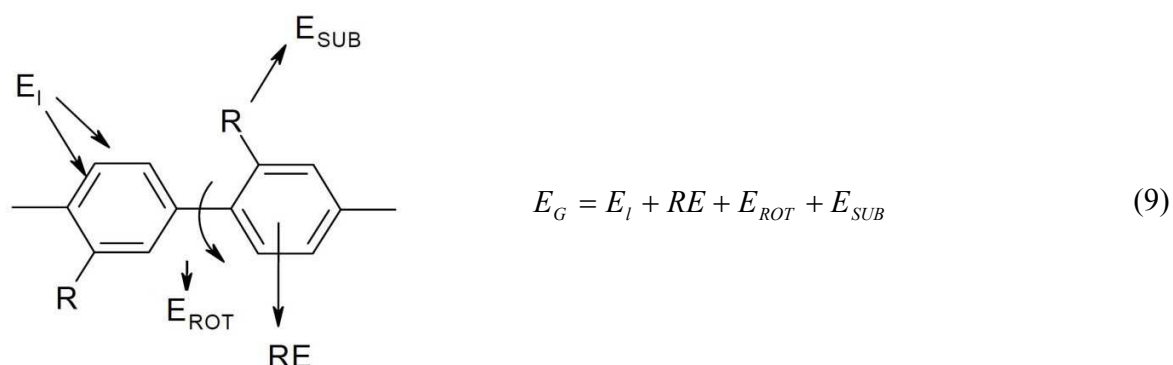
$$E_G = E_l + RE + E_{ROT} + E_{SUB} \tag{9}$$

Figure 2.11: Illustration of the different influences to the band gap, demonstrated at poly paraphenylene (taken from **[27]**).

**Bond length alternation ($E_l$)**

The bond length alternation is a very important factor for the band gap formation. In chapter 2.3.1 and 2.3.2, the influence to the band gap was already discussed in detail.

**Resonance energy ($RE$)**

For some molecules it is not possible to describe them by only one single Lewis formula, but by several contributing structures (also called resonant structures). None of those contributing structures describe the bonding characteristic and so the electron distribution in the molecule in a sufficient way. The real structure is given by a so called resonance hybrid, which has a structure that is intermediate between the contributing structures. An example of such a molecule is benzene. The first contributing structure shows a ring of six carbon atoms with an alternation of single and double bonds between the carbon atoms. When exchanging the sequence of the single and double bonds, one obtains the second contributing structure. Both structures are depicted on the left side of Figure 2.6. As shown in chapter 2.2, the $p_z$-orbitals of the six carbon atoms of benzene do not form three localized $\pi$-orbitals as it is described by the contributing structures, but form an over the whole molecule delocalized system of $\pi$-orbitals. The total energy of benzene with the system of localized $\pi$-orbitals (the resonance hybrid) is lower compared to the potential energies of the contributing structures as already explained in chapter 2.2. Generally one can say that the hybrids are therefore always more stable than any of the contributing structures would be. The difference between the potential energy of the resonance hybrid and the potential energy of the contributing structure is called the resonance energy. [27] [28] [29] [30]

**Change of band gap due to torsion ($E_{ROT}$)**

As shown in chapter 2.3.1, the size of the band gap depends on the length of the conjugated system and decreases with increasing length. This results due to the fact that the longer the conjugated system is, the more orbitals overap and the smaller is the band gap. The overlap can be affected by torsion of the molecule, leading to a larger band gap. Due to this reason, the stiffness of a molecule has a direct influence to the band gap: The stiffer the molecule, the smaller the band gap. [27]

**Influence of substituents to the band gap ($E_{SUB}$)**

Substituents (R in Figure 2.11) can affect the energetic position of the HOMO and LUMO level of a molecule. In general one can say, that electron donating substituents increase the HOMO level, whereas electron withdrawing groups lower the LUMO level. [27]

## 2.4 Excited states in organic semiconductors

### 2.4.1 Polarons

Looking at an inorganic semiconductor (ISC) in its ground state, it exhibits a filled valence band (VB) and an empty conduction band (CB). Due to electrical or photo physical processes, an excitation of the semiconductor can be achieved by raising an electron from the VB to the CB. In the CB, the electron is completely delocalized over the whole three dimensional lattice and can almost move freely. In organic semiconductors (OSC), this basic principle is similar, but some noteworthy differences exist. The equivalents to the VB and CB of an ISC are the HOMO and LUMO levels of the OSC. The excitation of an OSC leads to a lift of an electron from the HOMO to the LUMO. An OSC exhibits strong electron-lattice coupling. Due to this coupling, an excitation of an electron (which is a change of the electronic configuration) has the consequence that the polymer reacts by a structural change to achieve an energetically favorable configuration. This structural change also results in a slight variation of the HOMO and LUMO level (see polaron (POL) and bipolaron (BP)-levels in Figure 2.12). Additionally, in contrast to an ISC, the excited charges in an OSC cannot move freely, but are in strongly localized states, which means that the charges may be found anywhere within a region of the molecule of linear extent smaller than that of the molecule. These quasiparticles (quantums of energy which have positions and momentums and can in some respects be regarded as particles) are called polarons. More precisely, an additional electron in the LUMO is called negative polaron, if an electron is missing in the HOMO, one speaks about a positive polaron. Two additional electrons in the LUMO are called negative bipolarons, consequently two missing electrons in the HOMO are indicated as positive bipolarons. [31] [9] In Figure 2.12, a sketch of the energetic states of polarons and bipolarons is depicted.
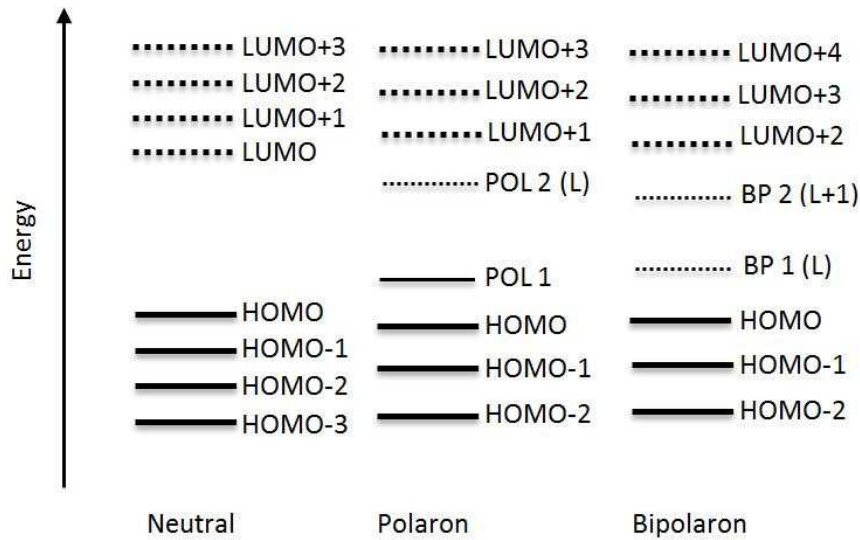
Figure 2.12: Overview of the energy levels of different quasi particles in conjugated polymers; ground state (neutral), polarons and bipolarons (taken from [32] and modified).

## 2.4.2 Singlet and triplet excitons

The quasiparticle exciton is formed by two polarons with opposite charges that are bound together by Coulomb forces. Depending on the distance $R$ between the polarons, one differs between Wannier-Mott-excitons with $R$ in the range of 40 to 100 Å, Frenkel-excitons with $R$ smaller than 5 Å and, between these two extreme cases, the charge transfer complexes (CT-complex). [33] In Figure 2.13 the different types are shown.
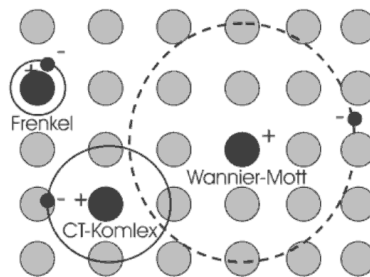


Figure 2.13: The different types of excitons in an organic and inorganic semiconductor, Wannier-Mott-exciton, Frenkel-exciton and the CT-complex (taken from **[33]**).

For OSC, the Frenkel-excitons are dominating. With the formula

$$E_{Exciton-binding} = \frac{e^2}{4\pi \cdot \varepsilon_0 \cdot \varepsilon_R \cdot R}$$ (10)

one can calculate the binding energy of an exciton approximately with the elementary charge $e$, electric constant $\varepsilon_0$, the permittivity $\varepsilon_R$ and the exciton distance $R$. Frenkel-excitons exhibit bindings energies in the range of 0,3 to 0,5 eV. In addition to the radius, the overall spin of an exciton is an important property.

Since excitons are formed by the combination of two polarons (which are fermions with a spin of $\pm\frac{1}{2}$), the total spin of an exciton is zero or one. Additionally, excitons are quasiparticles and therefore they can be described by wavefunctions. Due to Pauli's principle, the wavefunctions of excitons have to be antisymmetric concerning particle exchange. The wavefunction is divided into a spatial part and a spin part. If the spatial part is antisymmetric, the spin part has to be symmetric with total spin of one. There are three possibilities of spin combinations to fulfill this criteria: $(\uparrow\uparrow)$, $(\downarrow\downarrow)$ and $\frac{1}{\sqrt{2}}[(\uparrow\downarrow) + (\downarrow\uparrow)]$. These excitons are called triplet excitons. If the spatial part is symmetric, the spin part has to be antisymmetric, leading to a so called singlet exciton with a total spin of zero: $\frac{1}{\sqrt{2}}[(\uparrow\downarrow) - (\downarrow\uparrow)]$. [9]

Important for the operation of OLEDs is the fact that due to the statistical distribution of the fermion spins of the injected charge carriers (50% spin up, 50% spin down), 25% of the formed excitons in OLEDs are singlet excitons and 75% are triplet excitons.

Figure **2.14** summarizes the possible spin combinations graphically and as formula. Recent reports indicate that the fraction of formed singlet excitons in OLEDs can achieve values up to 63%, but discussions concerning this topic still go on. [34] [35] [36] [37]



$$|\Psi_t\rangle = |\uparrow\uparrow\rangle$$

$$|\Psi_t\rangle = |\downarrow\downarrow\rangle$$

$$\left.\begin{array}{l} |\Psi_t\rangle = \frac{1}{\sqrt{2}}(|\uparrow\downarrow\rangle + |\downarrow\uparrow\rangle) \end{array}\right\} \text{Triplet Excitons}$$

$$|\Psi_s\rangle = \frac{1}{\sqrt{2}}(|\uparrow\downarrow\rangle - |\downarrow\uparrow\rangle) \quad\} \text{ Singlet Exciton}$$
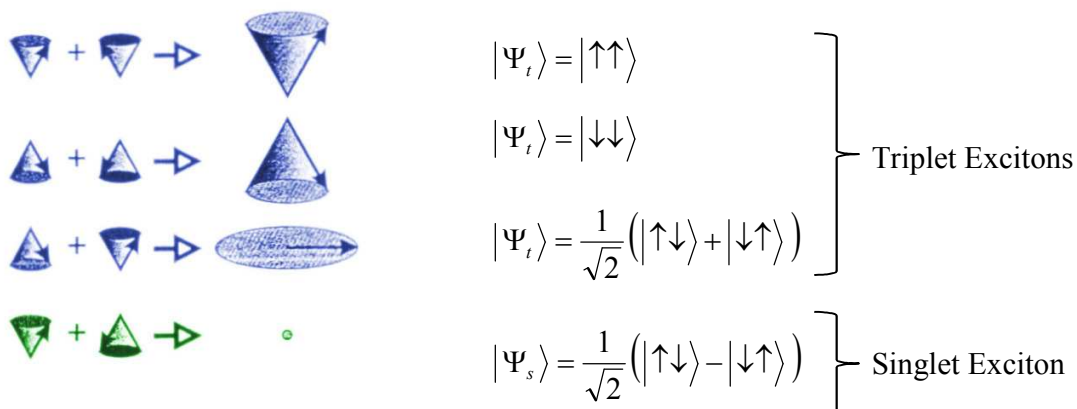
Figure 2.14: Schematic representation of the formation of singlet (green) and triplet (blue) excitons from polarons with different spin-polarization (taken from **[18]** and modified).

### 2.4.3 Charge transport in organic semiconductors

As explained before, in ISC an excited charge can almost move freely through the three dimensional lattice of the semiconductor. In contrast, excited charges in an OSC (polarons) are strongly localized. Therefore the charge transport looks quite different. It is a kind of hopping process, wherein a polaron hops from one localized state to another one of the same or an adjacent polymer unit. Associated with this charge transport (which is a change of the electronic configuration) is a structural change of the polymer. The energy that is needed for this structural change is the so called reorganization energy. [38] The whole process is driven by lattice vibrations. A detailed explanation of this process and the resulting charge transfer rate is given by the Marcus theory. [31] [39]

## 2.5 Excitation and recombination dynamics - Jablonski diagram

The Jablonski diagram (see Figure 2.15) is a graphical scheme of excitation and relaxation processes within atoms or molecules in an easily readable form. In vertical direction, the different electronic states with their vibrational levels are shown. $S_0$ depicts the singlet ground state, $S_1$ and $S_2$ are excited singlet states and $T_1$ describes a triplet state. Between these states, different kinds of physical processes can occur, which will be explained in the following:
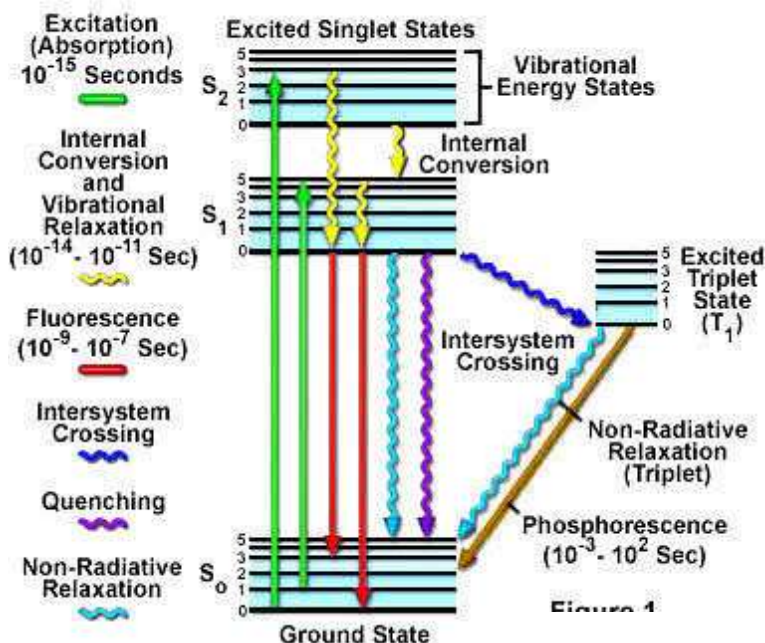


Figure 2.15: Jablonski diagram of radiative and non-radiative processes. The waved arrows illustrate the non-radiative processes like intersystem crossing, internal conversion and quenching processes, wherein the energy is released for example in form of heat. The straight arrows illustrate radiative processes, fluorescence and phosphorescence, leading to the emission of photons (taken from [40] and modified).

**Absorption and Franck-Condon-principle**

One way to form an exciton is to inject an electron into the LUMO, leading to a negative polaron and to inject a hole into the HOMO, leading to a positive polaron. As explained before, these two quasi particles can (due to electrostatic forces) form a singlet or triplet exciton. Another possibility of singlet exciton creation is the excitation of an electron from the HOMO to the LUMO by absorption of a photon, whereby a hole is left in the HOMO. This is possible if the incident photon possesses an energy which is equal or higher than the energetically difference between the HOMO and LUMO level. After this transition, the excited electron and the left hole can create an exciton. The excitation of the electron into the LUMO takes place within the timescale of $10^{-15}$ s [41]. It was already mentioned that an excitation of an electron is a change of the electronic configuration and the molecule responds to this change by a structural modification. The response time is in the range of about $10^{-13}$ s. In comparison to $10^{-15}$ s (time, one needs to lift the electron from the HOMO to the LUMO), the position of the atoms in the molecule is assumed to be constant during the excitation process and the physics of this process can be described by the Franck-Condon-principle [42]. The excited electron does not necessary have to populate the lowest vibrational level of an excited state, but can also end up in a higher vibrational level of an excited state according to the energy of the absorbed photon and the integral overlap of the vibronical wave functions. After the excitation, the electron relaxes radiationless to the lowest vibrational level of the excited state which is called vibrational relaxation. The typical time scale for these process is in the range of $10^{-13}$ to $10^{-9}$ s. Between upper excited electronic states and lower electronic states, a rapid radiationless process, called internal conversion, can take place. The time scale of this process depends on the energy difference between the electronic states. Generally speaking one can say, that the lower the energy difference, the faster the internal conversion process. For example, the time scales of internal conversions between excited states are in the order of $10^{-14}$ to $10^{-11}$ s. In contrast to this, the time scale of an internal conversion process between the first excited state $S_1$ and the ground state $S_0$ is in the range of $10^{-9}$ to $10^{-7}$ s. Therefore, an excited state will rapidly relax to the lowest vibrational state of the excited electronic state $S_1$ due to vibrational relaxation and internal conversion (shown as yellow waved arrows in Figure 2.15). From this point, several competing processes are now possible: fluorescence, phosphorescence, intersystem crossing, internal conversion and quenching processes.
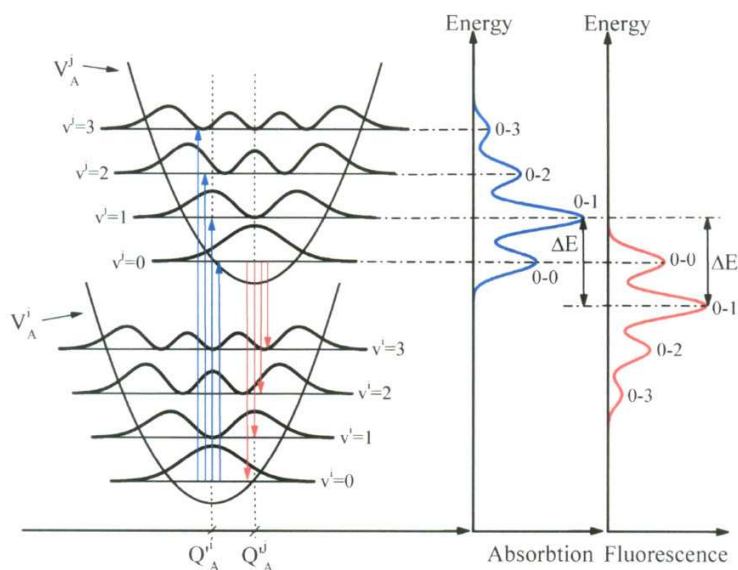
Figure 2.16: Frank-Condon principle energy diagram: excitation processes (blue arrows) and radiative relaxation processes (red arrows) between ground state and excited state and the resulting absorption spectrum, emission spectrum, and Stoke shift $\Delta E$ (taken from [43]).

**Fluorescence**

Depending on the spin directions of the electron and hole which form an exciton, different optical relaxation processes are possible. If there is no difference between the spin direction of an electron in the ground state and (after the excitation) in the excited state, a direct optical recombination into the ground state by emitting a photon is quantum mechanically allowed and is called fluorescence (red arrows in Figure 2.15). The selection rule concerning spin direction is fulfilled by the recombination process of a singlet exciton. The life time of a singlet exciton is in the range of $10^{-9}$ to $10^{-7}$ s. Also in the case of relaxation processes, the integral overlap of the vibronical wave functions in the ground state and the excited state is responsible for the probability of a transition. Due to this fact, the emission spectrum exhibits the inverse shape of the absorption spectrum. In practice, the absorption spectrum often is not the exact mirror image of the emission spectrum. Heimel et al. [44] showed that between the torsional degree of freedom of a molecule and the breakdown of the mirror image symmetry, a correlation can be established. In general it can be said: the more rigid a molecule is, the more the absorption spectrum corresponds to the mirror image of the emission spectrum. The difference in energy between the maximum of the emission spectrum and the maximum of the absorption spectrum (labeled with $\Delta E$ in Figure 2.16) is called the Stokes-shift. After the relaxations process, the electron does not necessarily end up in the lowest vibrational level of the electronic ground state, but due to internal conversion processes (see below), it quickly relaxes to the lowest vibrational state. [45]

**Phosphorescence**

When using the Born–Oppenheimer approximation, a relaxation of an excited state to the ground state is only quantum mechanically allowed, if a flip or rephrasing of the spin into the other direction is not necessary during the relaxations process. As a consequence, an optical recombination of a triplet exciton is forbidden and the excitation energy has to be released by non-radiative relaxation processes. However, under certain conditions it is possible to "circumvent" the selection rule for radiation. One example is the usage of molecules containing heavy atoms with strong spin orbit coupling, where it is possible to change the conserved quantities in the quantum mechanical system in that way that a spin flip during the relaxation can occur. In such a case an optical recombination can be achieved, which is called phosphorescence (orange arrow in Figure 2.15). Due to this reason, phosphorescence can hardly been seen in molecules that only contain low mass atoms. The typical life time of a triplet exciton is in the range of $10^{-3}$ to $10^{2}$ s. [45]

**Photoluminescence quantum yield**

An important property of a light emitting material is its photoluminescence quantum yield $\Phi$ (PLQY). It is defined by the ratio of radiative decays to the total number of decays (radiative and non-radiative). Another definition of the PLQY is the ratio of the number of emitted photons to the number of absorbed photons. Writing this definition as an equation, the following expression can be obtained:

$$\Phi = \frac{number\ of\ emitted\ photons}{number\ of\ absorbed\ photons} = \frac{k_R}{k_R + k_{NR}} \quad .$$
(11)

$k_R$ is the rate of radiative decays and $k_{NR}$ is the number of non-radiative decays. [9] [31]

**Intersystem crossing**

A radiationless transition between excited electronic states with different spin multiplicity is called an intersystem crossing. An example would be a transition between the singlet state S1 and the triplet state T1 (dark blue waved arrow in Figure 2.15). This transition is not allowed due to the forbiddances of spin conversion. As a result of spin-orbit coupling that can be determined at molecules containing atoms with higher masses, the rule of spin conservation can be weakened so that an intersystem crossing can occur. The time scale of this transition is in the order of $10^{-11}$ to $10^{-8}$ s. [31] [45]

**Quenching**

Quenching of fluorescence or phosphorescence refers to all processes that reduce the fluorescence or phosphorescence intensity of a material. In most cases, an intermolecular deactivation of an excited molecule by another molecule of the same or different type is the origin of quenching. [46] One has to notice that quenching considers only photo physical processes where no permanent chemical change takes place. [47] In the following, two important types of quenching, dynamic quenching and static quenching, will be explained in more detail. Additionally a short overview about SE-polaron-quenching and SE-TE-quenching will be shown, which play an essential role at high excitation densities.

*Dynamic quenching*

The basic prerequisite of dynamic quenching is a relatively close contact (collision) of the excited molecule and the quencher to enable the possibility of an energy transfer. [47] Due to this it is also called collisional quenching. The reduction of fluorescence due to dynamic quenching can be described by the Stern-Volmer-equation:

$$\frac{\Phi_0}{\Phi} = \frac{F_0}{F} = 1 + \tau_0 \cdot k_q \cdot [Q] \quad . \tag{12}$$

$\Phi_0$ and $\Phi$ are the PLQYs in absence and in presence of quenchers respectively, $F_0$ and $F$ the intensities of fluorescence in absence and in presence of quenchers respectively, $\tau_0$ the life time of the excited fluorophor in absence of quenchers, $k_q$ the quenching rate and $[Q]$ the concentration of quenchers. In gases and liquids, molecules show an enhancement of the average speed when increasing the temperature. The probability of collisions increases and an enhancement of the quenching rate can be observed. In solids, the molecules cannot move freely, but the higher the temperature, the more phonons exist which, in turn, lead to a higher quenching rate. [48]

*Static quenching*

Static quenching describes the decrease of the fluorescence intensity, if it is related to the formation of a less or non-radiative complex by the fluorophor and the quencher in the ground state. Due to the formation of the complex, the number of available radiative fluorophors decrease which leads to a decrement of the fluorescence intensity. The remaining fluorophors stay unaffected, so that the life time of the excited states is not changed. [49]

### SE-polaron-quenching

As observed in molecular crystals in the 1960's [50], trapped or free polarons can act as quenchers of SE during the migration process of the SE in disordered small molecules and conjugated polymer films, light emitting devices [51] and LASER applications [52], leading to a non-radiative quenching process:

$$p^{\pm} + S_1^* = S_0 + phonons + p^{\pm}.$$ (13)

$S_1^*$ is an excited SE, $p^{\pm}$ is a positive or negative polaron and $S_0$ is the singlet ground state.

### SE-TE-quenching

The SE-TE-quenching is a quenching process from an excited SE to a TE. Abiding Agranovich's theory [53], the process of SE-TE-quenching can be described in a similar way as the SE-polaron-quenching shown before and can be labeled mathematically by the following formula:

$$T_1 + S_1^* = S_0 + T_n + phonons.$$ (14)

$S_1^*$ is an excited SE, $S_0$ is the singlet ground state and $T_n$ an excited state of the TE manifold.

## Energy transfer

As explained in the paragraph above about dynamic quenching, an energy transfer occurs between the excited molecule and the quencher, enabling a quenching process. Two important types of these energy transfers, the Förster resonant energy transfer and the Dexter energy transfer, will be explained in more detail in the following:

### Förster resonant energy transfer

The Förster resonant energy transfer (FRET) is described by the following processes: The excited molecule (donor) transfers its excitation energy to the quencher (acceptor) by a radiationless dipol-dipol interaction. Afterwards the donor is in its ground state, the acceptor in an excited state. If the quencher is a fluorophor too, the FRET leads to a decrease of the fluorescence of the donor and an enhancement of the fluorescence of the acceptor.

To enable a FRET, the distance $r$ between the donator and acceptor has to be in a range of 2 to 10 nm due to the short range of the dipol-dipol interaction. [54] The energy transfer rate $k_{FRET}$ can be calculated by the following equation:

$$k_{FRET} = \frac{1}{\tau_D} \cdot \left( \frac{R_0}{r} \right)^6 . \tag{15}$$

$\tau_D$ is the life time of the excited donor in absence of the acceptor (quencher). The Förster radius $R_0$ is defined as the distance between acceptor and donor, where the probability of a spontaneous emission of the excited donor is the same as the probability of a FRET. In other words, at this distance the FRET efficiency is 50%. As a formula, the Förster radius $R_0$ can be written as

$$R_0 = \left( 8{,}79 \cdot 10^{23} \cdot \frac{\kappa^2 \cdot \Phi_D \cdot J_{DA}}{n^4} \right)^{\frac{1}{6}} \tag{16}$$

$\kappa^2$ is the orientation factor, $\Phi_D$ the photo luminescence quantum yield in absence of the acceptor and $n$ the refraction index of the medium between the donor and acceptor. The overlap integral $J_{AD}$ considers the overlap of the emission spectrum of donor and the absorption spectrum of acceptor. $J_{AD}$ can be calculated with the equation

$$J_{AD} = \int f_D(\lambda) \cdot \varepsilon_A(\lambda) \cdot \lambda^4 \, d\lambda , \tag{17}$$

where $f_D(\lambda)$ is the normalized radiant intensity of the donor molecule at the wavelength $\lambda$ and $\varepsilon_A(\lambda)$ is the extinction coefficient of the acceptor molecule. [49] [55]

Due to the fact that the FRET is a spin conserving process, only singlet excitons can take part. In Figure 2.17, a schematic picture of the radiationless FRET is shown.
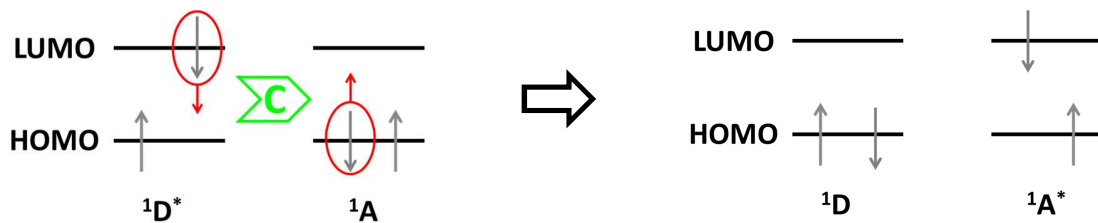


Figure 2.17: Sketch of the radiationless Förster resonant energy transfer between donor and acceptor. $^1D^*$ and $^1D$ indicate the donor in excited singlet state and ground state, $^1A^*$ and $^1A$ indicate the acceptor in excited singlet state and ground state. The green arrow represents the coulomb interaction between the donor and acceptor.

*Dexter energy transfer*

Instead of an energy transfer due to a dipol-dipol interaction as it is the case at the FRET, the Dexter energy transfer (DET) is based on an exchange of the excited electron from the donor

with a non-excited electron from the acceptor. Due to the exchange of two electrons, the spin has not to be conserved for the individual molecules (donor and acceptor), but for the whole interacting system. As a consequence, also a DET between triplet states are possible. [9] To enable the exchange of electrons, the orbitals of the donor and acceptor have to overlap, which requires a very short distance between the molecules of the interacting system. Typical values of the distance $r$ are in the range of 0,5 to 1 nm. [33] With the following equation (18), the DET rate $k_{DET}$ can be calculated:

$$k_{DET} = K \cdot J_{AD} \cdot \exp\left(-\frac{2 \cdot r}{L}\right). \tag{18}$$

$J_{AD}$ considers the spectral overlap of the emission spectrum of the donor and the absorption spectrum of the acceptor (see equation (17)), the factor $K$ is related to specific orbital interactions [9] and $L$ stand for the Van-der-Waals radius of the donor and acceptor. [33] In Figure **2.18**, a schematic picture of the radiationless DET is shown between two singlet and two triplet states.
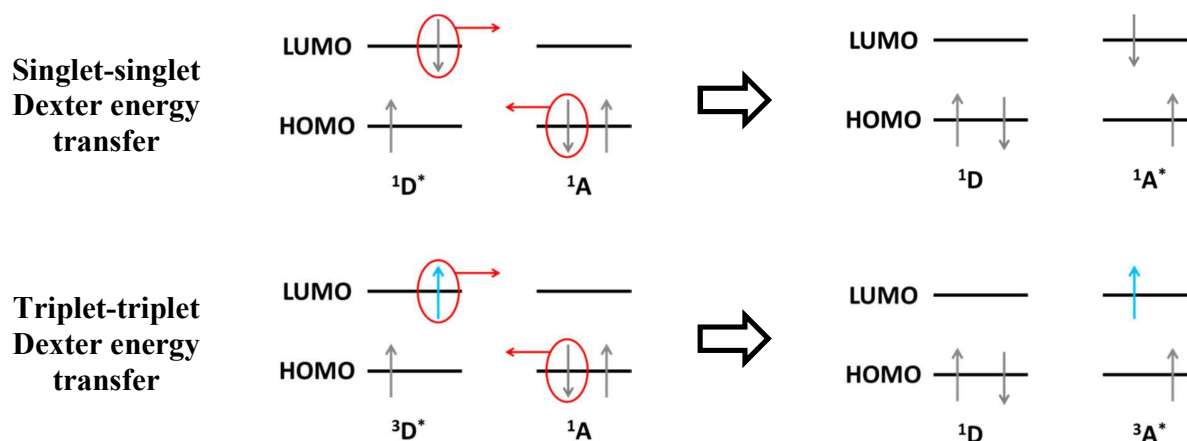


Figure 2.18: Sketch of the radiationless Dexter energy transfer between two singlet and two triplet states. $^1D$ and $^3D$ indicate the donor in ground singlet and ground triplet state, $^1A$ and $^3A$ indicate the acceptor in ground singlet and ground triplet state. The asterisk "*" earmarks the excited singlet and excited triplet states of the donor and acceptor.

# 3   Organic light emitting diodes

Photoexcitation is one way to generate excitons in the OSCs. Another way is the injection of electrons and holes from electrodes into the LUMO and HOMO of the OSC, leading to negative and positive polarons. If two polarons (positive and negative) get attracted by Coulomb forces, they can form an exciton which can undergo a radiative relaxation which is then called electro luminescence (EL). This is the basic process in organic light emitting diodes (OLEDs) for the generation of light. In contrast to ISCs, OSCs show lower charge carrier densities, wherein the charge carriers additionally have a lower mobility in comparison to charge carriers in ISCs. Due to these limitations, very thin OSC layers with thicknesses in the range of nm have to be assembled by using thin film technologies for the fabrication of OLEDs. However, the thinner the layer, the higher the probability for an injected charge carrier to reach the opposite electrode without forming an exciton. Due to this it is an important point in the development of OLEDs to find the appropriate thicknesses of the OSC layers.

## 3.1   Assembly of OLEDs

The schematic assembly of a single layer OLED is shown in Figure 3.1. In this thesis the labeling "single layer OLED" refers to the fact, that the OLED consisted of a single light emitting layer, whereas OLEDs which contain two or more light emitting layers are called multi layer OLEDs. The different layers and their functionalities will be explained in the following chapters.
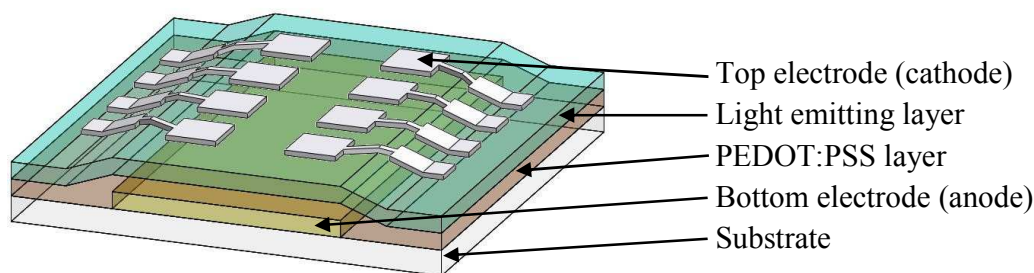


Figure 3.1: Schematic assembly of a single layer OLED: substrate, bottom electrode (anode), PEDOT:PSS layer, light emitting layer and top electrode (cathode).

### 3.1.1   Substrate

The requirements for the substrate can be combined to the following points: It has to be resistant against any mechanical, thermal and chemical stress during the OLED fabrication. Since most of the OSC show a high sensitivity with respect to air humidity and atmospheric oxygen, the substrate has to be impenetrable concerning those environmental influences. Additionally the

substrate has to be transparent in the wavelength range of interest to enable an out coupling of the emitted light. For most of the experiments, shown in the following, about 1 mm thick square glass plates were used as substrates. For the fabrication of flexible OLEDs, polyester films were used instead of glass substrates.

## 3.1.2 Electrodes – Anode and Cathode

**Anode**
The anode is placed between the substrate and the light emitting layer. The emitted light of the OLEDs has to pass through the anode, which therefore has to be transparent for light with the wavelength of interest. The material most commonly used for this application is indium tin oxide (ITO), a heavily-doped n-type semiconductor with a band gap between 3,5 and 4 eV. Due to this, ITO has a transparency of 80 to 90% in the range of visible light. [56] In chapter 6, experiments will be presented, where instead of ITO the combination of a gold layer and a high conductive Poly(3,4-ethylenedioxythiophene) poly(styrenesulfonate) (HC-PEDOT:PSS) layer will be used.

**Cathode**
The used electrode materials for the electron injection are typically aluminum (Al) and calcium (Ca). Due to the high reactivity of Ca with oxygen and water (air humidity), an aluminum layer is evaporated over the Ca layer for protection against environmental influences.

For the charge carrier injection from the electrodes into the light emitting layer, it is necessary to know the work function of the used material for both electrodes. The work function is the lowest energy that is needed to remove an electron out of the material. Later on in chapter 3.2, it will be shown that the levels of HOMO and LUMO are crucial for choosing the electrode materials.

## 3.1.3 PEDOT:PSS layer

Poly(3,4-ethylenedioxythiophene) poly(styrenesulfonate) (PEDOT:PSS) (see Figure 3.2) is a polymer mixture of two ionomers. For the simplest assembly of an OLED, a PEDOT:PSS layer is not necessary, but all OLEDs shown in this thesis are fabricated with this layer due to the following two reasons: Primarily, PEDOT:PSS is used as hole injection layer. Additionally it serves as a flattening layer of the ITO electrode, because the ITO layer exhibit sharp edges at the boundaries. When operating an OLED without a PEDOT:PSS layer, high electric field occur at the sharp edges (high compared to the electric field at flat areas of the ITO electrode) due to the electrical point effect and can cause a short circuit. Due to the additional electroconductive PEDOT:PSS layer, a homogeneous distribution of the electric field is achieved and an electrical point effect is avoided.
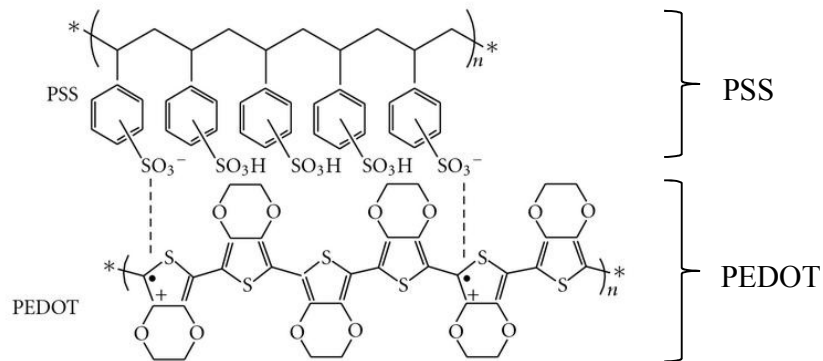
Figure 3.2: Chemical structure of PEDOT:PSS; upper molecule: PSS, lower molecule: PEDOT (taken from [57] and modified).

### 3.1.4 Light emitting layer

The centerpiece of an OLED is the light emitting layer. The charge carriers, which are injected into this layer from the electrodes, can lead to emission of light, when they recombine. A more detailed explanation is given in the following chapter.

## 3.2 Working principle of OLEDs

The operation of an OLED can be divided into three areas: the charge carrier injection from the electrodes into the light emitting layer, the charge carrier migration through the OSC under an applied electric field and the formation, migration and recombination of excitons. [9] Figure 3.3 shows the scheme of energy levels of an OLED with an applied bias $U_{ext}$ (in forward direction). $\phi_{ITO}$ and $\phi_{Al}$ describe the work functions of the anode and cathode (in this case made of ITO and Al). The energetic difference between the HOMO level of the OSC and the work function of the anode is labeled with $\Delta E_h$. $\Delta E_e$ labels the energetic difference between the LUMO level of the OSC and the work function of the cathode.
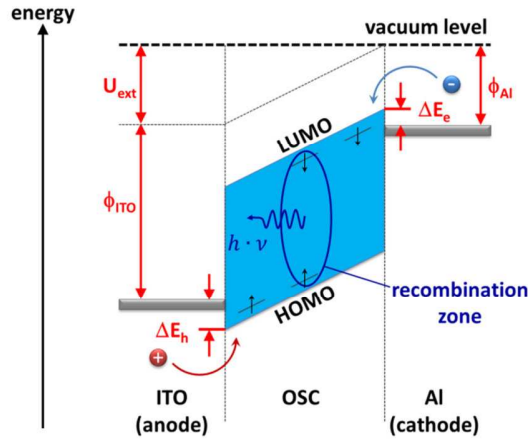
Figure 3.3: Scheme of the energy levels of a single layer OLED biased in forward direction (for detailed explanation see text).

To inject an electron and a hole into the light emitting layer, the potential barriers $\Delta E_h$ and $\Delta E_e$ have to be overcome respectively. In general there are two fundamental mechanisms: tunnel injection and thermal injection. The tunneling current is described with the Fowler-Nordheim-equation [58]

$$j(E) = K_1 \cdot \frac{E^2}{\phi} \cdot \exp\left( -\frac{K_2 \cdot \phi^{3/2}}{E} \right), \qquad (19)$$

with the electric field $E$, the injection barrier $\phi$, the elementary charge $e$ and the two material specific constants $K_1$ and $K_2$. Charge injection due to thermal excitation is explained by the Richardson-Dushman-equation [58]

$$j(T) = A \cdot T^2 \cdot \exp\left( \frac{e \cdot \phi}{k_B \cdot T} \right), \qquad (20)$$

with the material specific constant $A$, the temperature $T$, the elementary charge $e$, the injection barrier $\phi$ and the Boltzmann constant $k_B$. In comparison to the charge injection by tunneling, the injection by thermal excitation plays only a subordinate role. This is caused by the fact that due to the thermal energy of the molecules of about 25 meV at room temperature it is only possible to overcome injections barriers in this scale range.

**Location of recombination zone**

The location of the recombination zone within the light emitting layer depends on several specific factors of the OLED setup like the height of the injection barriers, the charge carrier mobility or

33

the presence of charge carrier blocking layers. For the following consideration the mobility of electrons and holes are assumed as equal. In Figure 3.4, three schemes of the energy levels of a single layer OLED are shown, where cathode materials with different work functions are used, leading to different locations of the recombination zone. The usage of a cathode material with a high work function like silver (Ag) leads to a low injection of electrons due to a high potential barrier (left side of Figure 3.4). As a consequence, the electrons are the minority carriers and the holes are the majority carriers in the OSC, leading to a recombination zone near the cathode. Using a cathode material with a low work function like cesium fluoride (CsF), an inverse behavior is achieved. Now the holes are the minority carriers and the electrons are the majority carriers (right side of Figure 3.4), leading to a recombination zone near the anode. Only when electrode materials are chosen where a balanced charge carrier injection is possible, a recombination zone in the middle of the light emitting layer can be achieved (center of Figure 3.4). [31]
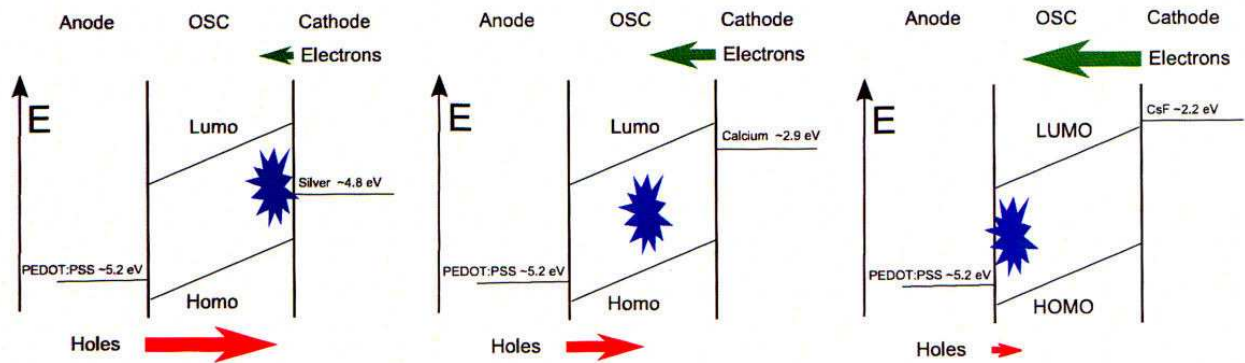


Figure 3.4: Sketch of an OLED energy level diagram, where cathode materials with different work functions are used, leading to different positions of the recombination zone within the light emitting layer (taken from **[31]**).

**Device efficiency**

In chapter 2.5, the photoluminescence quantum yield $\Phi_{PL}$ is defined as the ratio of the number of emitted photons by the number of absorbed photons. In comparison to this, the electro luminescence quantum yield (ELQY) is defined as the ratio of photons created per injected electron. [58] Besides $\Phi_{PL}$, further parameters affect the electro luminescence quantum yield $\eta_{EL}$,

$$\eta_{EL} = \Phi_{PL} \cdot r_{ST} \cdot \gamma \cdot k \ . \tag{21}$$

The parameter $r_{ST}$ considers the ratio between the formation of singlet and triplet excitons in the OSC. $\gamma$ denotes the number of formed excitons per injected electron. If an electron and a hole are injected into the OSC, a formation of an exciton is not guaranteed. As a first approximation, the

thickness of the light emitting layer can be considered as the factor with the main influence to the parameter $\gamma$. The thinner the thickness of the light emitting layer, the higher the probability that the charge carriers can reach the opposite electrode without forming an exciton. Losses due to quenching effects are taken to account by the parameter $k$.

Considering geometrical issues of OLEDs and regarding only photons leaving the device, one can define the external quantum efficiency $\eta_{Ext}$

$$\eta_{Ext} = \eta_{EL} \cdot g \; , \tag{22}$$

where the factor $g$ mainly accounts substrate, waveguided and plasmonic losses. [58] [59]

In Figure 3.5, a sketch of the external quantum efficiency and all light loss channels of an OLED device are shown. Additionally it is stated which loss channel is taking into account by which parameter.
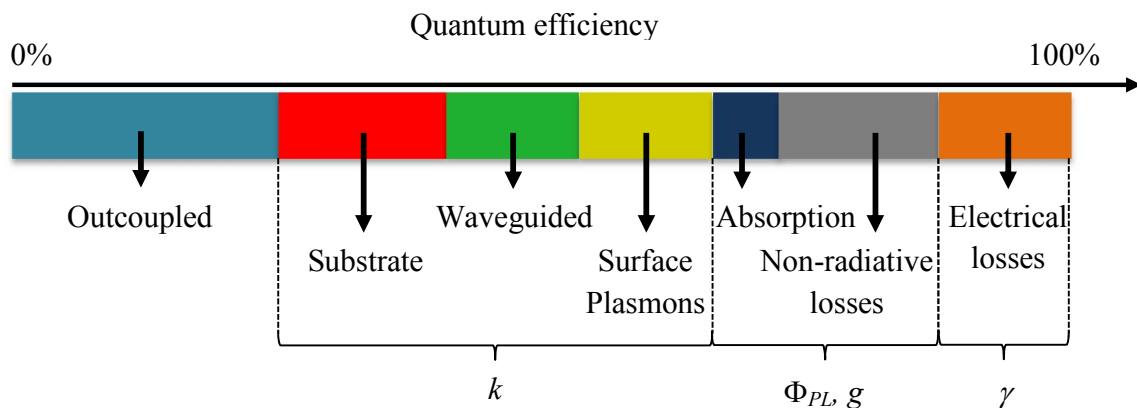


Figure 3.5: Unscaled sketch of the external quantum efficiency (outcoupled) and all loss channels in an OLED device (taken from **[59]** and modified).

## 3.3 Multi layer OLEDs - Enhancement of efficiency

In order to yield an as high as possible device efficiency of organic light emitting diodes, the layer structure of most OLEDs not only consists of one active material layer, but of more layers. Methods to increase the device efficiency are the improvement of the charge carrier injection and the charge carrier accumulation at the heterostructure interface of two OSC layers to facilitate the formation of excitons.

An extended possibility for multi layer devices is the usage of two OSC layers with different emission colors. The target in this case is not to increase the device efficiency, but to achieve the possibility of a color switch.

### 3.3.1 Improving charge carrier injection

An improvement of the charge carrier injection can be achieved by adding a charge transport layer. If the LUMO level of the emitting layer is higher than the work function of the cathode, electrons have to overcome a potential step to be injected into the LUMO (see Figure 3.6, *a* and *c*). By adding a charge transport layer with an LUMO level between the LUMO level of the emitting layer and the work function of the cathode, the step is apportioned into two smaller steps. The same concerns are also valid for holes if the HOMO level of the light emitting layer is lower than the work function of the anode. In this case, a charge transport layer with a HOMO level between the HOMO level of the light emitting layer and the work function of the anode is used for improving the hole injection. The charge transport layer itself can also be a light emitting layer as it will be shown in chapter 5. From quantum mechanics it is known that the probability of a particle to tunnel through a barrier can be described by equation (23) [60],

$$P(E) = \frac{1 - \dfrac{E}{E_0}}{\left(1 - \dfrac{E}{E_0}\right) + \left(\dfrac{E_0}{4E}\right)\sinh^2\left(a\dfrac{\sqrt{2m(E_0 - E)}}{\hbar}\right)} \; . \tag{23}$$

$E_0$ is the height of the barrier, $E$ the energy of the particle, $m$ the mass of the particle and $a$ the tunneling distance. The important fact is that the tunneling probability of the particle is not a linear function of the inverse of the tunneling distance. This leads to the outcome that when a potential barrier is divided into two potential barriers, the probability of tunneling through the whole distance increases and the charge carrier injection is improved.

Figure 3.6 shows a sketch of the energy levels of the individual layers (light emitting layer, charge transport layer, electrode). Parts *a* and *b* represent the case with and without an additional electron transport (ETL) layer with no bias applied. Parts *c* and *d* show the energy level diagrams with applied bias. In case *c*, the electrons have to overcome one high potential barrier, in case *d* two smaller ones. Tunneling trough two smaller barriers in case *d*, is more probable than tunneling through the barrier in case *c*, because the probability of tunneling through the barrier is not linearly proportional with the inverse of the tunnel length, as explained prior to this (see equation (23)).
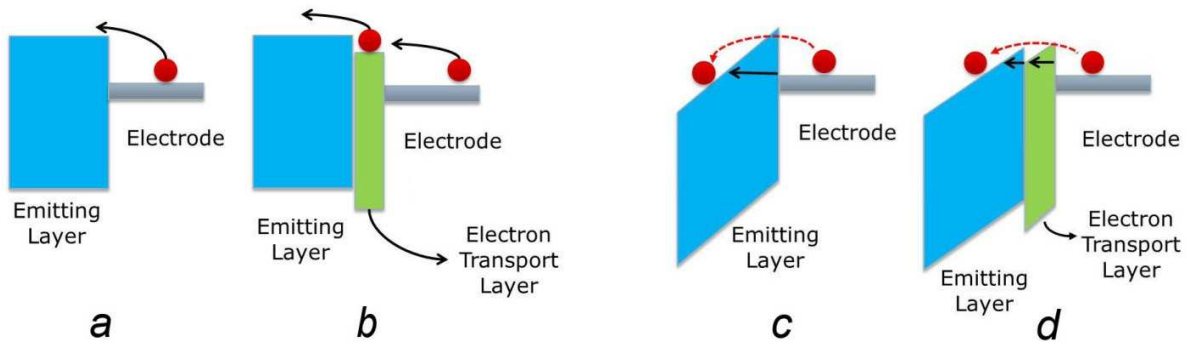
Figure 3.6: Sketch of energy levels: *a*: energy levels of emitting layer and electrode; *b*: energy levels of emitting layer, electron transport layer and electrode; *c*: same as *a*, but with applied bias; *d*: same as *b*, but with applied bias.

## 3.3.2  Charge carrier accumulation at heterostructure interface

Another possibility to improve the device efficiency by using multiple layers is to use two different OSCs with small differences between their HOMO and/or LUMO levels for the fabrication of two light emitting layers on top of each other. An example of such a situation is shown in Figure 3.7. The used OSCs polyfluorene (PF) and poly(indenofluorene) (PIF) have almost the same LUMO levels, the HOMO levels show a minor, but important difference. For holes, this step forms a small barrier that leads to an accumulation of holes in the PIF layer at the interface to the PF layer. Due to this accumulation, the probability that an electron in the LUMO of PIF forms an exciton with a hole in the HOMO of PIF is enhanced. This finally leads to an enhanced device efficiency. [61]
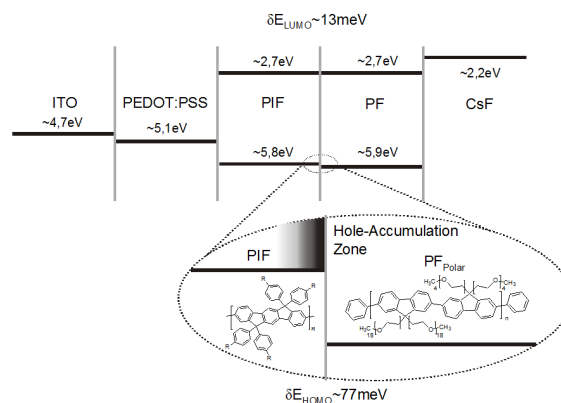


Figure 3.7: Schematic diagram of the energy levels of the hetero structure and the chemical structure of the utilized conjugated polymers (for detailed explanation see text; taken from **[61]**).

### 3.3.3  Shift of emission color

To enable a shift of the emission color of a multi layer device, two light emitting layers are required, where the emitting materials have different emission colors. A shift of the recombination zone between the two light emitting layers leads to a change of the emission color. For example one considers two OSCs (OSC1 and OSC2), which have the same LUMO, but different HOMO levels, where the HOMO level of OSC1 is higher than the HOMO level of OSC2. Applying an electric field leads to an accumulation of holes in the OSC1 layer at the interface to the OSC2 layer and most of the recombination processes occur in the OSC1 layer. Increasing the applied electric field, a decrement of the tunnel barrier between the OSC1 and OSC2 layer ($l_2 < l_1$) is achieved and the number of tunneled holes into the HOMO of the OSC2 increases. Due to this, more recombination processes in the OSC2 layer occur, which finally causes a change of the emission color of the multi layer device. In summary, the emission color is controllable by changing the applied electric field. In Figure 3.8, a schematic energy level diagram of the hetero structure (OSC1 and OSC2) is shown at different applied electric fields.
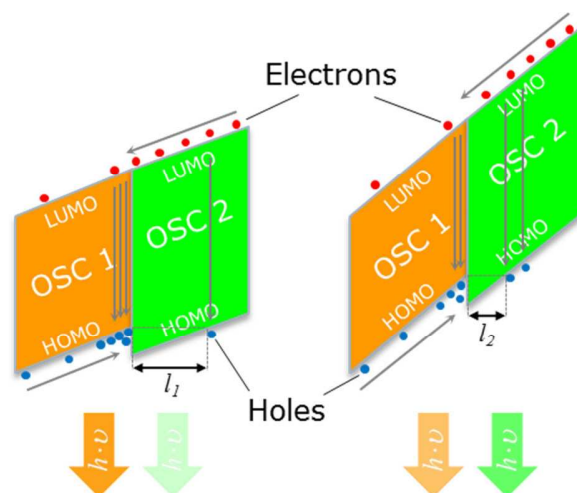


Figure 3.8: Schematic diagram of the energy levels of the hetero structure (OSC1 and OSC2) at different applied electric fields; left: accumulation of holes in OSC1 at the interface of OSC1 and OSC2, most recombination processes take place in the OSC1 layer; right: increasing the applied electric field causes a decrement of the tunnel barrier length ($l_2 < l_1$), leading to an enhancement of recombination processes in the OSC2 layer and finally to a change of the emission color.

### 3.3.4  Different approaches of multi layer assembling

As already explained, two important classes of OSC materials are used for the fabrication of OLEDs: small molecules and conjugated polymers.
Small molecules provide the opportunity of vacuum deposition. With this method, a multi layer OLED is fabricated by simply evaporating the different OSC layers on top of each other.

However, the method has the disadvantage that it is a high vacuum process which is time consuming and has a limited flow-rate. Therefore it is less suitable for large scale production of OLED devices.

In contrast to the procedure using small molecules, the usage of conjugated polymers has the potential for cheap large scale production. Instead of evaporating the OSC, polymers are dissolved with solvents. Afterwards the solutions are deposited by spin coating or similar techniques onto the sample. The big advantage of this technique is that no high vacuum processes for the coating of the OSC layer are needed. For large scale production, methods like ink jet printing or roll-to-roll processing would be adequate. However, there are also disadvantages when using polymers and solution based manufacturing for the fabrication of OSC layers. The synthesis of conjugated polymers is in the fledgling stages and to reach the ELQYs of small molecules, further research is needed. When using solution based manufacturing for the fabrication of multi layer devices, the used solvents have to be selected purposefully. Concerning the wettability properties of the solvent, it has to wet the underlying polymer layer (which has to be coated) evenly to ensure a homogeneous layer formation. Moreover the underlying polymer layer should not be dissolved or becomes damaged during the coating process. To prevent such effects, different approaches have been demonstrated, ranging from liquid buffer layers between the individual polymer layers, to in situ converted or cross-linked electro-optical active polymer layers. [62] Another possibility is to use orthogonal solvents. Orthogonal in this case means, for example, the first solvent is able to dissolve polymer A, but not polymer B and the second solvent can dissolve polymer B, but not polymer A. So it is possible to fabricate multi layer devices with the polymers A and B without damaging the underlying layer.

All multi layer devices that are discussed in this thesis were built by solution based manufacturing and by the usage of orthogonal solvents. A detailed explanation will be shown in the corresponding chapters.

# 4  Experimental methodology

In the following, the individual process steps for preparation and fabrication of OLEDs are explained in detail. Afterwards, all measurement routines used for the determination of the experimental data are presented.

## 4.1  Preparation

### 4.1.1  Substrate

For most experiments, ITO coated quartz glass plates were used as substrates. The plates have a squared shape with an edge length of 25 mm and a thickness of about 1 mm. The ITO layer was structured via wet-chemical etching. Therefore the ITO surface was covered with tape at the area where the ITO should not be removed. For wet-chemical etching, hydrochloric acid (HCL; 37%) was used. For a faster etching process, the catalyst zinc powder was strewn onto the ITO surface. The etching process took about 25 s, followed by rinsing the substrate in deionized water. After the etching process, the tape was peeled off. To remove the adhesive leftovers and other contaminations, a combination of chemical and mechanical cleaning steps, containing polar and nonpolar solvents, were performed. In detail, the substrates were cleaned with acetone (polar) followed by isopropanol (nonpolar). Afterward the substrates were cleaned in an ultrasonic bath in isopropanol for 15 min. The last cleaning step was a 10 min oxygen plasma etching process. During the discharge in an oxygen atmosphere, OH-groups were added to the surface of the substrate enhancing the wettability for water. This was important for spin coating of PEDOT:PSS from a water based solution. [18]

For flexible OLEDs, 175 µm thick Melinex$^®$ polyester films instead of glass plates were used as substrates. Due to the soft surface of the film, mechanical cleaning would lead to scratches in the substrate and so had to be avoided. The film substrate was rinsed with isopropanol, followed by rinsing with deionized water. The foil substrate was dried with a nitrogen jet followed by spinning the substrate with 5000 rpm for 100 s by using the spin coater. Before spin coating the HC-PEDOT:PSS layer, a gold layer was evaporated onto the film. The last step was also a 10 min oxygen plasma etching process.

As reference, also an ITO coated polyester film (OFD-10-St504-5mil) manufactured by Solutia$^®$ was used for the fabrication of flexible OLEDs. The etching procedure was the same as for etching of ITO coated glass substrates with the difference that the etching time was only 15 s. For cleaning, the same procedure as for the Melinex$^®$ polyester films was used.

## 4.1.2  Layer preparation

For the fabrication of the individual polymer layers of the OLED, a spin coater was used. Spin coating is a procedure to apply uniform thin layers on flat substrates from solution, where a certain amount of solution is placed on the substrate which is then spun at a defined rotation speed. Due to the centrifugal force, the biggest part of the solution is catapulted away, but a thin layer is left over. By changing the rotation speed or the concentration of the solution, the thickness of the layer can be adjusted.

The first spin coated layer (after plasma etching) contested of PEDOT:PSS and HC-PEDOT:PSS respectively. Before spin coating (at ambient conditions), the substrate was blown with a nitrogen jet to remove possible impurities, followed by dropping the solution onto the substrate. After a waiting period of 10 s (to increase the wetting and the adhesion of the film), the spin coater was started. The next step was a heating process at 120°C to dry the coated layer. During this process, the heating chamber was evacuated ($p < 5 \cdot 10^{-3}$ mbar). At the end of the process, the substrate was left in the chamber to cool down to about 50°C. Afterwards it was removed and cooled down to ambient temperature in argon atmosphere in a petri dish. When spin coating HC-PEDOT:PSS, the substrate was immediately removed from the heating chamber at 120°C and cooled down in a petri dish in argon.

The emitting layer (or layers) was applied by a spin coating process in argon. The process steps were almost the same as shown for the fabrication of the PEDOT:PSS layer, but with the difference, that the substrate was blown with an argon jet to remove possible impurities before spin coating and the spin coating process was started immediately after dropping the polymer solution onto the substrate. Depending on the used polymer, individual parameters for the spin coating and heating process were chosen. The individual layers were prepared by using the parameters shown in Table 4.1 (if not stated otherwise).

**Thickness measurements**

For the determination of the layer thicknesses, two measuring units were used. The first was a VEECO Nanoman VS atomic forces microscope, the second a VEECO Dektak 150 profilometer.

Table 4.1: List of spin coating, drying and cooling parameters of the individually fabricated polymer layers (explanations of the acronyms are shown at the beginning of this thesis in the table of abbreviations). The spinning process consisted of one or two process sections (1, 2). Ramp indicates the acceleration ramp, the time corresponds to the operation time of the process section.

| Layer | Spin parameter | Drying parameter | Cooling after drying |
|---|---|---|---|
| PEDOT:PSS | 1: 2500 rpm, ramp 4, 40 s | 120°C, 45 min, in a vacuum ($p < 5 \cdot 10^{-3}$ mbar) | Cooling to ~50°C in heat chamber, further cooling in petri dish to ambient temperature. |
| HC-PEDOT:PSS | 1: 1500 rpm, ramp 4, 120 s | 120°C, 20 min, in a vacuum ($p < 5 \cdot 10^{-3}$ mbar) | Immediate removal from heating chamber and cooling in petri dish to ambient temperature. |
| fPF (parameter 1) | 1: 1500 rpm, ramp 2, 12 s<br>2: 3000 rpm, ramp 0, 40 s | 60°C, 45 min, in a vacuum ($p < 5 \cdot 10^{-5}$ mbar) | Cooling to ~50°C in heat chamber, further cooling in petri dish to ambient temperature. |
| fPF (parameter 2) | 1: 1000 rpm, ramp 9, 240 s<br>2: 1000 rpm, ramp 9, 240 s | 60°C, 45 min, in a vacuum ($p < 5 \cdot 10^{-5}$ mbar) | Cooling to ~50°C in heat chamber, further cooling in petri dish to ambient temperature. |
| MEHPPV | 1: 1500 rpm, ramp 2, 12 s<br>2: 3000 rpm, ramp 0, 40 s | 60°C, 45 min, in a vacuum ($p < 5 \cdot 10^{-5}$ mbar) | Cooling to ~50°C in heat chamber, further cooling in petri dish to ambient temperature. |
| HTP | 1: 1000 rpm, ramp 2, 12 s<br>2: 3000 rpm, ramp 0, 40 s | 200°C, 60 min, in argon | Cooling down to ~100°C, further cooling on argon box bottom to ambient temperature. |
| HTP:fPF (blend) | 1: 1000 rpm, ramp 9, 240 s<br>2: 1000 rpm, ramp 9, 240 s | 60°C, 45 min, in a vacuum ($p < 5 \cdot 10^{-5}$ mbar) | Cooling to ~50°C in heat chamber, further cooling in petri dish to ambient temperature. |
| PEGPF | 1: 1500 rpm, ramp 2, 12 s<br>2: 3000 rpm, ramp 0, 40 s | 60°C, 45 min, in a vacuum ($p < 5 \cdot 10^{-5}$ mbar) | Cooling to ~50°C in heat chamber, further cooling in petri dish to ambient temperature. |
| PIF | 1: 1500 rpm, ramp 2, 12 s<br>2: 3000 rpm, ramp 0, 40 s | 60°C, 45 min, in a vacuum ($p < 5 \cdot 10^{-5}$ mbar) | Cooling to ~50°C in heat chamber, further cooling in petri dish to ambient temperature. |

### 4.1.3 Top electrode

The final preparation step was the evaporation of the top electrode in a vapor deposition unit (VDU) in an argon box. After closing the chamber of the VDU, it was evacuated. When reaching a pressure value of $p \leq 10^{-6}$ mbar, the evaporation process was started. As top electrode the combination of a 10 nm thick calcium layer protected by a 100 nm thick aluminum layer or only a 100 nm aluminum layer was used. For some experiments an additional ETL was evaporated which was located between the emitting layer and the top electrode.

## 4.2 Determination of surface energies and dissolving

### 4.2.1 Surface energies of polymer layers and solvents

An important physical property, coupled with the topic of solution based manufacturing, is the surface energy of the produced conjugated polymer layers and the surface energies of the subsequently used solvents. For fluids also the term surface tension is used. The surface energy quantifies the disruption of intermolecular bonds (that occur when a surface of a solid or a fluid is created) and defines the amount of energy that is needed for the generation of a surface per unit area (SI unit: $J/m^2$). In general, surfaces with a high surface energy can easily be covered by materials with a low surface energy, but not the other way round. [63] In this context, often the term "good or bad wettability" is used.

For the manufacturing of multi layer OLEDs one is interested in producing smooth layers with a uniform layer thickness and a low layer roughness. To gain an understanding into the behavior of the combination of the different used polymer surfaces with different used solvents, contact angle and surface energy measurements were accomplished. For measurements, the contact angle measuring system DSA100 from Krüss was used. To calculate the surface energy of an unknown surface (polymer layer), the contact angle of a solvent with a known surface tension is dropped onto the investigated surface, followed by the measurement of the contact angle and with the aid of the empirical equation

$$\cos(\alpha) = -1 + 2\sqrt{\frac{\sigma_s}{\sigma_l}} \cdot e^{-\beta(\sigma_l - \sigma_s)^2}, \tag{24}$$

the surface energy of the investigated surface can be calculated. $\alpha$ is the contact angle, $\sigma_l$ the known surface tension of the solvent, $\sigma_s$ the unknown surface energy of the investigated surface and $\beta$ an empirically determined constant ($\beta = 0,0001247$). [64] In Figure 4.1 on the left side, the measurement unit for gauging the contact angle of a solvent on the surface of the sample can be seen. The right side shows a picture of a conjugated polymer layer, where a solvent drop is applied.
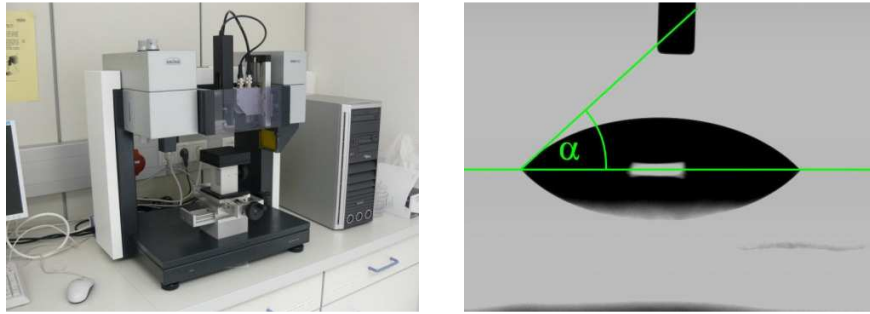
Figure 4.1: Left: measurement unit DSA100 for contact angle measurement; right: drop of solvent on polymer layer, α delineates the contact angle.

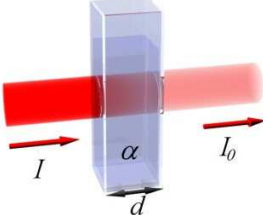## 4.2.2 Dissolving of polymer layer during coating process

As explained in the chapter before, the first condition for a successful assembly of multi layer OLEDs by solution based manufacturing is that the layer which should be coated shows a sufficient large wettability concerning the applied solvent. The second important point in the fabrication is that the underlying layer is not dissolved or becomes damaged during the coating process due to the applied solvent.

To verify the damage of the underlying layer during the spin coating process, two investigation methods were accomplished. The first was to examine the samples which were used for the contact angle measurement with a profilometer. The layer thickness was measured in the region where the solvent was dropped onto the polymer surface and in an unstressed area. By comparing these two values, one was able to estimate the etching destruction due to the solvent. To verify the results of the first investigation method, a second method was performed. In this case, two substrates were fabricated in the same way, as for the contact angle measurement. One of these substrates was spin coated with the corresponding solvent. The second substrate was left untreated. The difference of this method was that the dissolved polymer was ejected during spin coating so that no re-deposition was possible. Subsequently, the layer thicknesses of both samples were measured by using the profilometer. Both investigation methods showed similar results (difference < 5%) and were complementary used for the determination of the etching destruction due to the solvent. The individual values of the surface energies and the damage due to applying the solvent onto the layer are specified at the corresponding chapters about the assembled multi layer OLEDs.

## 4.3 Absorption measurements

If light is passing through matter, the intensity of the light beam got weakened due to absorption, reflection and scattering effects inside the material. The effect of the absorption depends on the

absorption coefficient of the material and the length of the optical path through the matter. This behavior can be explained in a first approximation by the Beer-Lambert law:



$$I = I_0 \cdot e^{-\alpha \cdot d} \,. \tag{25}$$

Figure 4.2: Sketch of light beam traveling through a material for illustration of the Beer-Lambert law (taken form [65] and modified).

$I$ is the intensity of the light beam after travelling through matter, $I_0$ is the light beam intensity before the pass through, $\alpha$ is the absorption coefficient of the sample and $d$ the length of the optical path in the material. For the measurements, a PERKIM ELMER LAMBDA 900 UV/VIS spectrometer was used. To be able to calculate the absorbance of a thin polymer film or polymer solution, the intensities $I$ and $I_0$ have to be measured. $I$ is represented by the beam intensity after the cross through the glass substrate with a thin polymer film on top or the cross through a quartz cuvette filled with a polymer solution (see Figure 4.2). For determination of $I_0$, the beam intensity after the pass through of an uncoated glass substrate or a quartz cuvette filled with the pure solvent has to be measured.

When reading documents about absorption experiments, one will discover that the definition of absorption and absorbance is often not determined clearly. For example Hollas [66] defines that the absorption spectrum is typically measured in absorbance, which is calculated by the common logarithm of the ratio $I_0 / I$. On the other side Atkins et al. [12] used this formula as the definition of the absorption. Cantle [67] defines the absorption by the formula $I - I_0$, the absorbance is defined in the same as formulated by Hollas. For clarification, in this thesis all absorption spectra are measured in absorbance, which is defined by the formula:

$$Absorbance = \log\!\left(\frac{I_0}{I}\right) \tag{26}$$

For measuring the absorbance of a thin polymer layer, a polymer film was spin coated from a 4 g/l solution onto a glass substrate. The absorption spectrum of a polymer in solution was determined by measuring solutions in a concentration range of $10^{-3}$ to $10^{-1}$ g/l.

## 4.4 Photoluminescence measurements

For the measurement of the photoluminescence (PL) spectrum, a SHIMADZU RF-5301PL spectrofluoro-photometer was used. Thin polymer films were investigated by spin coating a 1 g/l solution onto a glass substrate, followed by a PL measurement. For the analysis of polymers in solution, solutions in a concentration range of $10^{-7}$ to $10^{-2}$ g/l were measured on the one hand to investigate any self absorption effects and on the other hand to ensure that the measured signal reaches a sufficiently high value. Due to the fact, that the sensitivity of the sensor is not constant over the wavelength range, the recorded data were corrected by the detector's sensitivity curve.

## 4.5 Photoluminescence quantum yield measurement

As shown in chapter 2.5, the PLQY is defined as the ratio of photons absorbed to photons emitted through fluorescence. For the determination of the PLQY, an indirect measurement method was applied, where a material with a known PLQY was used as reference. [68] The idea behind this method is to compare the absorbance and the integrated fluorescence intensity of different fluorophors.

The measurement procedure can be summarized as follows: First a recording of the absorption spectrum of the polymer in solution in a quartz cuvette has to be done. The next step is to record the fluorescence spectrum of the same solution at an appropriate excitation wavelength (near the maximum of the absorption spectrum). After the fluorescence spectrum is corrected concerning the wavelength dependent sensitivity of the detector, one has to calculate the integrated fluorescence spectrum (this corresponds to the area of the fluorescence spectrum). These measurements have to be repeated with different concentrations of the solution. Plotting a graph of the integrated fluorescence intensity vs. the absorbance value (at the excitation wavelength) at different concentrations resulted in a straight line with a gradient $grad_x$. To be able to make a statement about the PLQY of the investigated polymer X in solution, one has to do the same measurement with a fluorophor that has a known PLQY. In the case of this thesis, quinine sulfate dihydrate with a PLQY of 54,5% in solution was used as reference. Finally it is possible to calculate the PLQY of the investigated polymer X by the following formula:

$$\Phi_X = \Phi_{QS} \cdot \left( \frac{grad_X}{grad_{QS}} \right) \cdot \left( \frac{n_X}{n_{QS}} \right)^2 . \tag{27}$$

$\Phi_X$ and $\Phi_{QS}$ are the PLQYs of the investigated polymer X and quinine sulfate dihydrate in solution, $grad_X$ and $grad_{QS}$ are the gradients from the plot of integrated fluorescence intensity vs. absorbance, $n_X$ and $n_{QS}$ are the refraction indices of the used solvents for dissolving the polymer X and quinine sulfate dihydrate. [31] [68]

When measuring solutions with different concentrations, one has to take care that there are no self absorption effects due to too high concentrations of the solution. An indication for a too high concentration is an advanced deviation of measured data points from the straight line in the graph of the integrated fluorescence intensity vs. the absorbance with increasing the concentration. One

has to be aware that an error in the range of 10% should be assumed for this measurement method. [31]

## 4.6  Device characterization

### 4.6.1  Current-voltage-luminescence characteristic

Luminance is a concept used to quantify the density of luminous flux emitted from a particular area in a specific direction toward a light receiver such as a human eye. The definition of luminance $L$ is:

$$L = \frac{I}{A_S \cdot \cos(\Theta)} \; .$$

(28)

The SI unit of luminance is cd/m$^2$. Referring to Figure 4.3, $I$ is the luminous intensity produced on area $A_S$ of the light source in the direction of the receiver $P$ and $A_p$ is the projected area of the source when viewed from the receiver. The luminance concept is important in illumination design because it is a physically measurable quantity that correlates with the subjective evaluation of "brightness" when viewing a surface or object. [69]
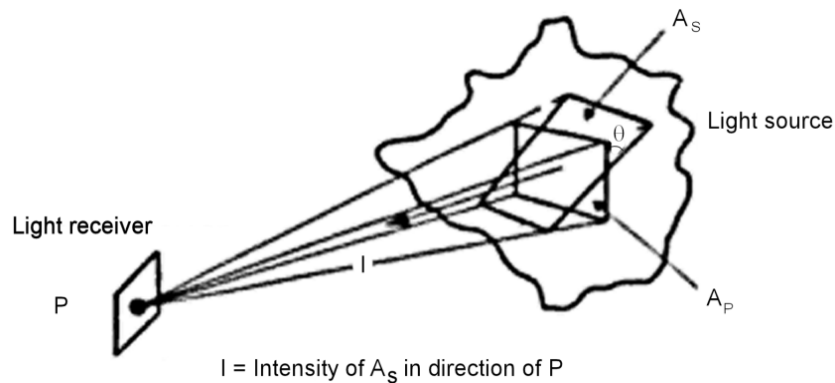


Figure 4.3: Concept of luminance (for detailed explanation see text; taken from **[69]** and modified).

For the measurement of the luminance value, the OLED was mounted and sealed in an airproof measuring cell (see Figure 4.4). Afterwards the measuring cell was connected to a computer controlled KEITHLEY 2612 sourcemeter. To be able to measure the luminance during the recording of the IV-characteristic, a silicon photo diode which is connected to a KEITHLEY 6417A electrometer was placed on the window of the measuring cell. The measured signal (photocurrent) from the silicon photo diode is proportional to the luminance value of the OLED.

In order to calibrate the signal of the silicon photo diode, a calibrated luminance analyzer (MINOLTA LS-100 luminancemeter) was used for a reference measurement to determine the right proportionality factor between the photocurrent and the luminance value. Some of the depicted current-voltage-luminance characteristics (IV characteristics) in this thesis show occasional luminance peaks in a voltage range below the onset voltage. This can be explained by the noise of the detector and the bad signal-to-noise ratio in this operating range.
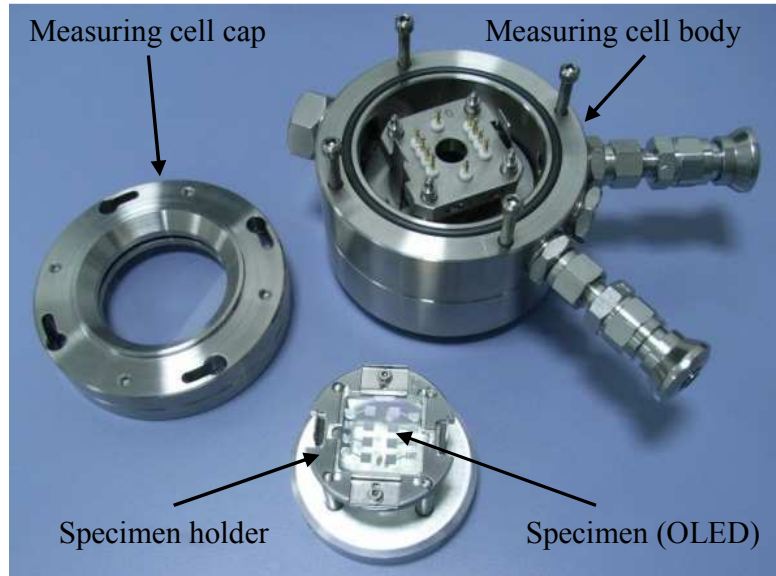


Figure 4.4: Disassembled measuring cell, cell body, cell cap and specimen holder for the investigation of the manufactured OLEDs.

## 4.6.2  Analysis of electroluminescence spectra

The spectral distribution of the light emitted by the investigated OLED was measured by a LOT-ORIEL CCD-spectrometer. Inside the spectrometer, the incoming light gets separated by a grid. The spectral components are then analyzed by a charge coupled device sensor (CCD). To reduce the noise of the sensor chip, it is cooled (-30°C and -50°C respectively for the measurements shown in this thesis). Due to the fact, that the sensitivity of the sensor is not constant over the wavelength range, the recorded data set has to be corrected by the detector sensitivity curve.
First, the emission spectra at different applied voltage values were recorded. The measurement of the spectra started at the lowest possible voltage value where an emission signal was detectable. The measurement was continued by stepwise increasing the applied voltage and after every step the spectrum was recorded again. Due to this series of measurements it was possible to determine the spectral change caused by the increment of the applied voltage. The second measurement was similar to the first one, but instead of changing the applied voltage, the device current was varied.

If one is interested in the device current density (in A/m$^2$) instead of the device current (in mA), one has to use to the following equation:

$$Device\ current\ density\left(\frac{A}{m^2}\right) = \frac{Device\ current\ (mA)}{9\cdot10^{-3}\ m^2}. \tag{29}$$

# 5 Assembling of multi layer OLEDs

In this chapter, the fabrication and characterization of all assembled multi layer systems is presented. For solution based manufacturing, two novel polymers, one soluble in fluorinated solvents, the other soluble in alcohol (like methanol), were combined with already determined polymers soluble in toluene and chloroform respectively. Before the results of the particular multi layer systems are given, a discussion about the detailed investigations of the novel polymers is shown.

## 5.1 Multi layer OLEDs with fluorinated polyfluorene

This chapter deals with the application of a novel conjugated polymer – fluorinated polyfluorene (fPF) – which is soluble in fluorinated solvents. By the combination of this polymer with other already known polymers (soluble in orthogonal solvents), multi layer OLEDs were assembled, wherein two different approaches concerning the configuration of the light emitting layers were made. In the following chapter, these approaches are explained in more detail. In the course of this discussion, the substantial question is answered, to what extent it is even possible to create multi layer OLEDs with the used polymers and solvents, taking into account the problems concerning wettability and dissolving as discussed in chapter 4.2. Afterwards, the experiments for the determination of the fPF properties are explained and finally the measurements results of the fabricated multi layer systems are shown.

### 5.1.1 Multi layer systems - determination of wettability and dissolving

For a first approach, the blue emitting fPF was combined with a red emitting polymer poly[2-methoxy-5-(2'-ethyl-hexyloxy)-1,4-phenylenevinylene] (MEHPPV). For the experiment, devices with different sequences of the fPF and MEHPPV layers were assembled, wherein also different types of top electrode configurations (Al and ETL/Ca/Al) were tested. The ETL was made of 1,3,5-tri(phenyl-2-benzimidazole)-benzene (TPBi). In Figure 5.1, sketches of the assembled multi layer OLEDs with the device configurations ITO/PEDOT:PSS/fPF/MEHPPV/ (TPBi/Ca)/Al and ITO/PEDOT:PSS/MEHPPV/fPF/(TPBi/Ca)/Al are shown.

The second approach was to combine fPF with a blue emitting polymer with an enhanced hole transport characteristic. The used hole transport material was a copolymer with equal amounts of poly(indenofluorene) and triphenylamine based units in its backbone. [31] In the following, the acronym HTP is used for this copolymer. Beside the layer system, also a blend system of fPF and HTP was investigated. The OLED assemblies of the layer system (ITO/PEDOT:PSS/HTP/ fPF/TPBi/Ca/Al) and the blend system (ITO/PEDOT:PSS/HTP:fPF/TPBi/Ca/Al) are shown in Figure 5.2.
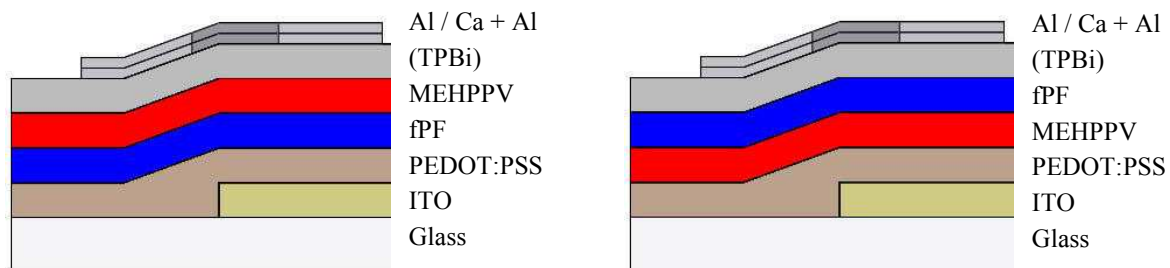
Figure 5.1: Sketch of the layer sequences of the investigated multi layer OLEDs using MEHPPV (red emitter) and fPF (blue emitter) as light emitting layers.
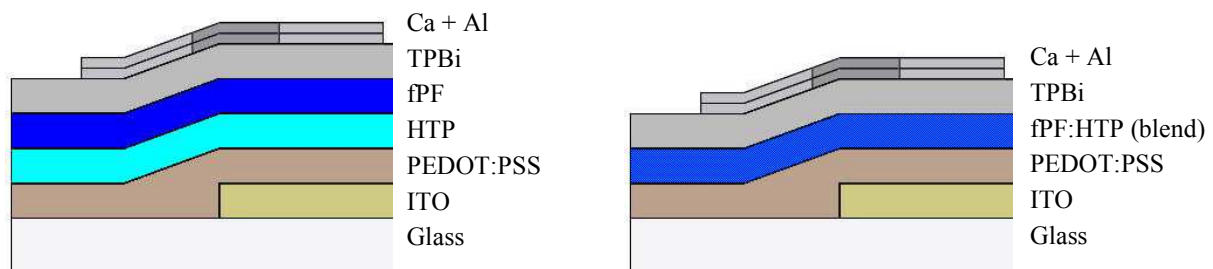


Figure 5.2: Sketch of the layer structures of the investigated multi layer OLEDs using HTP and fPF as light emitting layers in a layer system (left) and a blend system (right).

In the following, results of experiments are shown to point out, if it is even possible to coat the light emitting layers on top of each other by solution based manufacturing, and if so, to answer the question if there is a damage of the polymer films when applying the individual polymer solutions during the spin coating processes.

**Contact angles and surface energies**

For the fabrication of the multi layer OLEDs, the fPF was dissolved in $\alpha,\alpha,\alpha$-trifluorotoluene (TFT) and MEHPPV in chloroform. In Table 5.1, the surface energies of the polymer layers and the used solvents for coating are listed.

Table 5.1: Surface energies (SE) of fPF, MEHPPV and HTP layer and the used solvents for the coating process.

|  | fPF layer | MEHPPV layer | HTP layer | $\alpha,\alpha,\alpha$ - trifluorotoluene [70] | chloroform [71] |
|---|---|---|---|---|---|
| SE (in mN/m) | 12,69 | 34,70 | 31,50 | 23,39 | 27,50 |

Due to the theory that surfaces with high surface energies can easily be covered by materials with low surface energies, it is expected that covering the MEHPPV layer with a solution consisting of TFT is possible. In contrast, covering the fPF layer with chloroform, wetting problems are supposed. Spin coating the fPF solution onto a MEHPPV layer showed satisfying results, spin coating the MEHPPV solution onto a fPF surface led to a blotchy layer, as expected. The contact angle of TFT on the MEHPPV layer is 9,6°, the contact angle of chloroform on the fPF layer is 35,9°. Figure 5.3 shows the devices with fPF coated on MEHPPV and MEHPPV coated on fPF.
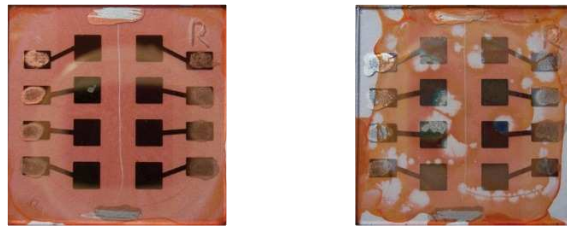


Figure 5.3: Left: formation of a smooth fPF layer (fPF dissolved in TFT) when spin coating onto a MEHPPV layer; right: formation of a blotched MEHPPV layer (MEHPPV dissolved in chloroform) when spin coating onto a fPF layer.

The contact angle of TFT on the HTP layer is 8,1°, which implies a good wettability as it is already expected due to the measured surface energies shown in Table 5.1

**Dissolving**

The investigations concerning the influence of dissolving the polymer layer during the spin coating process showed that after treating the MEHPPV layer with the solvent TFT, about 90% of the layer thickness is left and about 80% of the HTP layer remains. In Figure 5.4, pictures of the investigated MEHPPV and HTP films are shown. The areas, which were stressed with TFT are labeled with yellow markings.
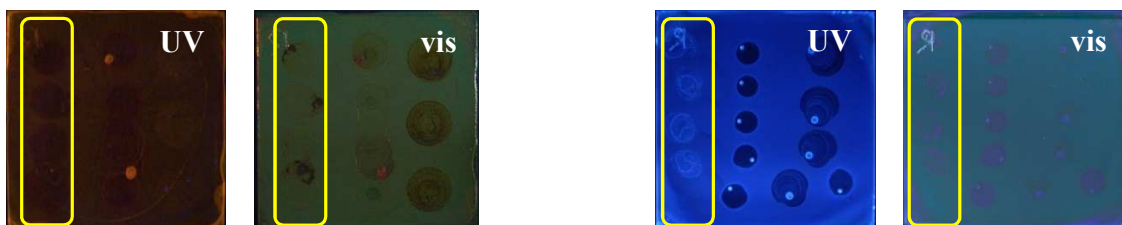


Figure 5.4: Pictures of MEHPPV film (left) and HTP film (right) taken during illumination with UV light and visible light after stressing with solvents. The yellow markings label the regions, where the polymer layers were stressed by applying TFT.

## 5.1.2 Chemical structures of fluorinated polyfluorene and fluorinated solvents

Polyfluorene consists of two bridged benzene rings. At the bridgehead (C9-position), side chains are added by alkylation [72]. These side chains are responsible for the solubility of the polymer. In the case of the fluorinated polyfluorene, the side chains contain fluorine ($C_7F_{15}$; see Figure 5.5) which facilitated the dissolving of the polymer in fluorinated solvents. For the fabrication of OLEDs with a fPF layer, the solvents $\alpha,\alpha,\alpha$ -trifluorotoluene (TFT) and hexafluorobenzene were used (see Figure 5.6).
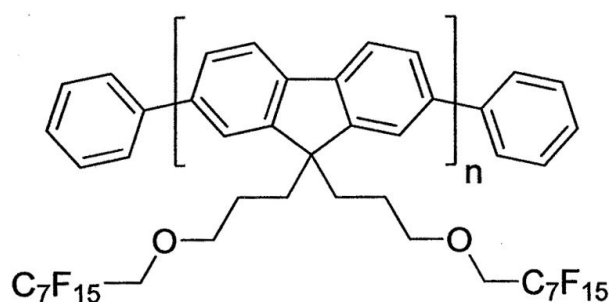


Figure 5.5: Chemical structure of fPF with fluorinated side chains.
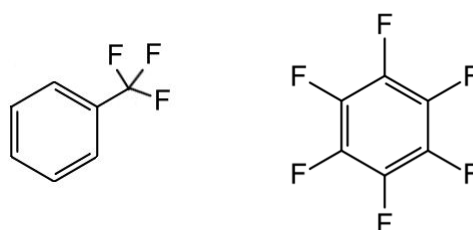


Figure 5.6: Left: $\alpha,\alpha,\alpha$-trifluorotoluene (taken from [73] and modified); right: hexafluorobenzene (taken from [74]).

## 5.1.3 Photo physical characterization of fluorinated polyfluorene

In the following, the photophysical properties (absorption and photoluminescence spectra in film and in solution, photoluminescence quantum yield in solution) of the fPF are shown. After discussing the stability of the absorption and photoluminescence spectra of the fPF in film under environmental influence, the results of the fabricated OLEDs are presented.

**Absorption, emission and quantum yield of fluorinated polyfluorene**

TFT was used as the solvent for fPF for all experiments shown in this subchapter. Prior to processing and measuring, the solution was stirred for 24 hours to facilitate a completely dissolving of the polymer.

The emission spectrum of fPF in film shows a significant intensity in the range of 400 to 500 nm with a peak maximum at 420 nm and a vibronic fine structure at 446 nm. The absorption spectrum has a maximum at 388 nm and no vibronic fine structure (Stokes shift: 32 nm). In contrast to the film emission of fPF, the emission maximum of fPF in solution shows a blue-shift due to solvatochromism and appears at 412 nm with a vibronic fine structure at 435 nm. The absorption spectrum shows a maximum at 386 nm (Stokes shift: 26 nm). In Figure 5.7, the absorption and PL spectra of fPF in film and in solution are depicted.
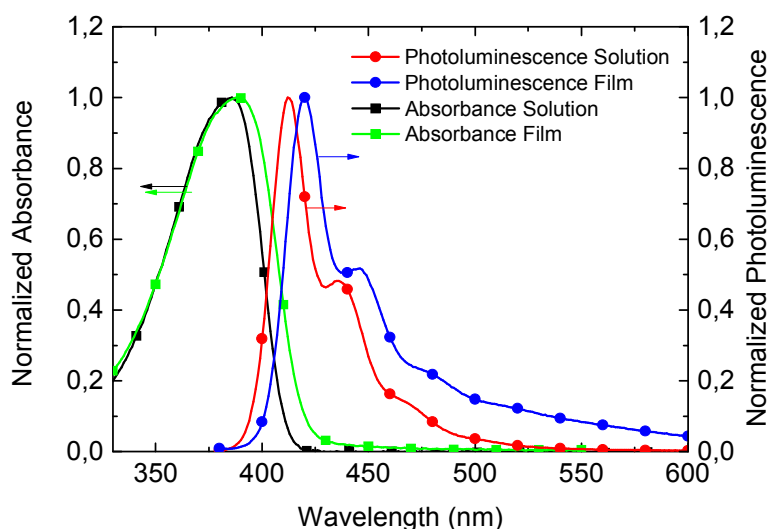


Figure 5.7: Absorption and PL spectra of fPF in solution and in film.

To calculate the photoluminescence quantum yield, solutions of fPF with the concentrations $10^{-4}, 5 \cdot 10^{-3}, 10^{-3}, 0{,}125 \cdot 10^{-2}, 0{,}25 \cdot 10^{-2}$ and $0{,}5 \cdot 10^{-2}$ g/l were investigated (as explained in chapter 4.5). In Figure 5.8 the integrated corrected photoluminescence and its corresponding absorbance values are shown as red squared data points. The linear fit of the data points is indicated by the red line. The used quantum yield standard was quinine sulfate dihydrate with a defined quantum yield of 54,5 %. The data for quinine sulfate dihydrate (black line in Figure 5.8) were taken from Nau [31]. The calculated photoluminescence quantum yield of fPF in solution is 99 %.
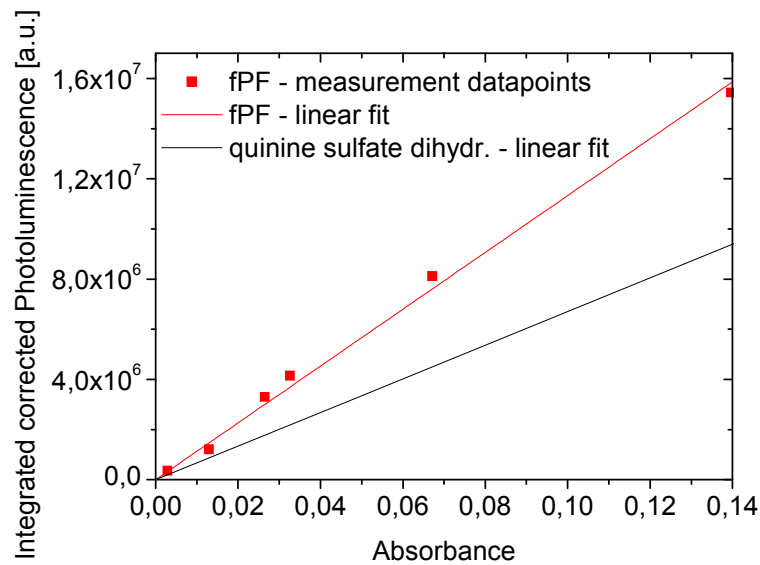
Figure 5.8: Measured points (red squares) and linear fit (red line) of fPF, linear fit of quinine sulfate dihydrate (black line) **[31]**.

**Photoluminescence related stability of fluorinated polyfluorene**

For applications of conjugated polymers in the display and lighting industry, the materials have to show – besides a high efficiency – a high stability against environmental influences. To get an idea of the stability of fPF, three different measurements were performed. The first two experiments investigated the stability with respect to thermal stress and the third, the stability with respect to UV irradiation.

*Stability with respect to thermal stress*

To investigate the stability of fPF with respect to thermal stress, two glass substrates with a spin coated fPF layer were heated at 100°C for the total of five hours, in which the absorption and the photoluminescence spectra were measured immediately after spin coating and at regular time intervals. To avoid any effects or reactions due to ambient light, the probes were covered during heating. To determine the influence of oxygen and atmospheric humidity, one sample was heated under ambient conditions, the other one in argon.

After heating the sample under ambient conditions for five hours, no big change in the absorption spectrum is determinable. In contrast to this, an additional peak appears at about 540 nm in the emission spectrum. The origin of this spectral feature can be described by the so called Keto defect. This effect explains a photo- (or electro-) oxidative degradation process and leads to an undesired low-energy emission at about 2,2 to 2,3 eV in polyfluorene. [75] [76] Converted to wavelengths, this encases the range 540 to 560 nm. The absorption and photoluminescence

spectra of the thermally stressed samples at different heating times under ambient conditions are shown in Figure 5.9.
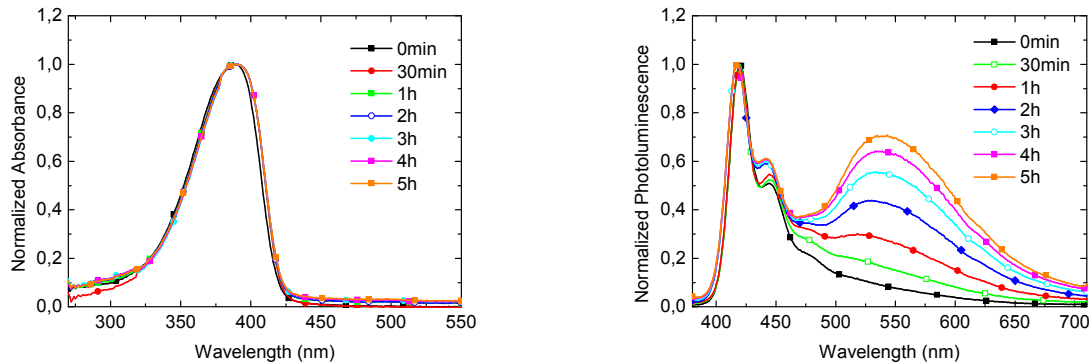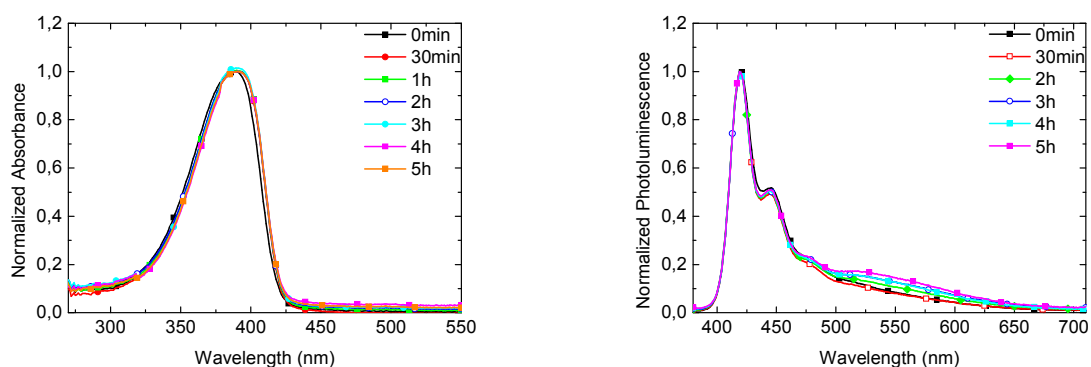


Figure 5.9: Absorption (left) and PL spectra (right) of fPF film measured at different exposure times during heating at 100°C under ambient conditions.

In comparison to the sample stressed under ambient conditions, the fPF film, heated in an argon box, shows nearly no change to the PL spectrum (see Figure 5.10). This is a further indication that the Keto defect is accountable for the additional peak at 540 nm. The small change in the region of 540 nm can be explained by the fact that there was also a small amount of oxygen in the argon box (< 20 ppm) and the measurement of the absorbance and the PL took place under ambient conditions. So a reaction with oxygen was possible, but this effect was much smaller in comparison to the spectral change due to thermal stress under ambient conditions.



Figure 5.10: Absorption (left) and PL spectra (right) of fPF film measured in air at different exposure times during heating at 100°C in argon.

## *Stability with respect to UV irradiation*

The third task was to measure the influence of UV radiation on the PL spectrum. Due to the UV radiation, an appearance of so called singlet oxygen can occur. This high reactive molecule is able to react with the polymer, leading to a spectral change. [31] Beside the task of measuring the PL spectrum, the SHIMAZU RF-5301PC spectrofluoro-photometer was also used as UV

illumination source. For this reason, one was able to make sure that the stressed area is always equal to the area where the PL measurement is performed. It was not possible to measure the absorption spectra, because the sample had to stay in the specimen holder. For illumination, a wavelength of 280 nm was used via the excitation monochromator. Even after six minutes of exposure to UV irradiation, no big differences in the spectra are detected (see Figure 5.11), which is an indication that UV irradiation plays only a minor roll to the life time of fPF.
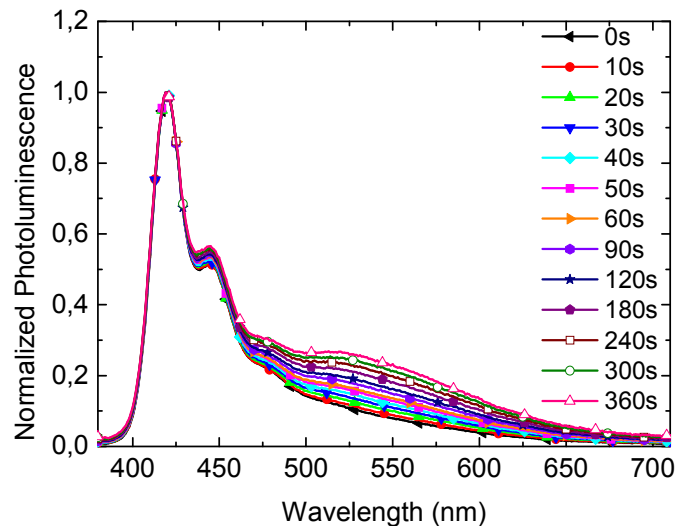


Figure 5.11: PL spectra of fPF film measured at different exposure times during illumination with UV irradiation (280 nm) under ambient conditions.

## 5.1.4  Single layer OLED with fluorinated polyfluorene

For the first investigation of fPF as light emitting layer in an OLED, fPF was dissolved in TFT with a concentration of 5 g/l, leading to a layer thickness of  about 15 nm. Indium tin oxid coated glass was used as substrate. On top of it, a PEDOT:PSS layer followed, ensued by the fPF layer. As top electrode, a calcium pad structure was deposited in a vacuum. Finally, the calcium electrodes were covered by aluminum. The whole layer structure, including the thicknesses of the individual layers, is depicded in Figure 5.12.
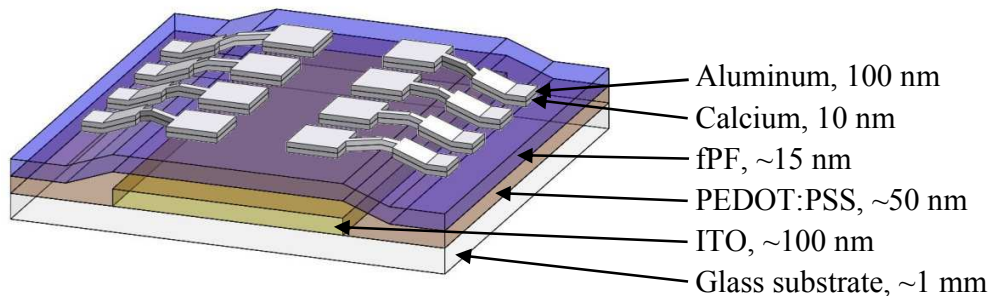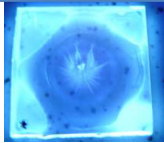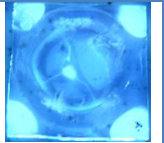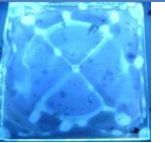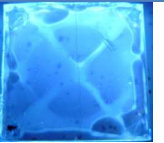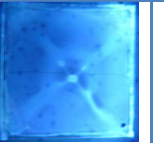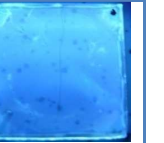
Figure 5.12: Assembly and thicknesses of the individual layers of the single layer OLED.

The high quantum yield of the fPF gave the opportunity for a good performance as light emitting layer in an OLED. Unfortunately, the single layer device with the device configuration ITO/PEDOT:PSS/fPF/Ca/Al, exhibits a poor luminance and efficiency value (7,68 cd/m$^2$; $8 \cdot 10^{-4}$ cd/A). However, the device shows blue emission (CIE 1931 x = 0,181 and y = 0,142) with an emission peak at 419 nm. A detailed overview about the measurement results are shown in the appendix in chapter 8. The first attempt to improve the performance of the OLED was to add an ETL (TPBi). The device with the layer configuration ITO/PEDOT:PSS/fPF/TPBi/Ca/Al shows an enhancement compared to the device without an TPBi layer, but the performance is still poor (0,012 cd/A; 27,72 cd/m$^2$; all measurement results shown in chapter 8). The low thickness of the fPF layer can be the reason for the poor device performance. The lower the layer thickness, the shorter is the propagation time of injected electrons and holes through the fPF layer and the more unlikely is the formation of excitons before the charge carriers reach the opposite electrode. Due to this, the thickness of the fPF layer was increased.

**Increasing device efficiency by variation of layer thickness**

The technique of spin coating achieves two possibilities to change the thickness of the coated layer. The first, is to change the spin parameters (acceleration ramp, rotational speed and duration) and the second, is to use a higher concentration of the solution. An economical use of the polymer was necessary, because the amount of fPF was limited. So the first attempt was to change the spin parameters, therefore a series of substrates with the layer configuration ITO/PEDOT:PSS/fPF was fabricated. The acceleration ramp and the spin duration stayed the same, but the rotational speed was changed (100, 200, 400, 600, 800, 1000 rpm). In Table 5.2, pictures of the ready-made samples illuminated with UV light are shown. At low rotating speed, the surface is inhomogeneous, only after the rotational speed reaches the value of 1000 rpm or higher, the surface shows a maintainable uniformity.

Table 5.2: Pictures of fPF films on ITO/PEDOT:PSS spin cast at different rotational speed.

| Samples irradiated with UV light | | | | | | |
|---|---|---|---|---|---|---|
| **rpm** | 100 | 200 | 400 | 600 | 800 | 1000 |

By using the new determined spin parameter (1000 rpm for 480 s, ramp 9), the thickness of the layer increases to 29 nm. The efficiency of the assembled OLED (all measurement results shown in chapter 8) almost stays at the same value, only the maximum luminance value rise by about 10% (31,58 cd/m$^2$; 0,011 cd/A). To increase the layer thickness further, the concentration of the solution was changed from 5 to 10 g/l, all the other parameters stayed the same, leading to a fPF layer thickness of 57 nm. Assembling an OLED with these new parameters shows a strong performance enhancement. The maximal luminance value increases from 31,58 to 257,0 cd/m$^2$ and the efficiency heightens from 0,011 to 0,177 cd/A. The device shows blue emission (CIE 1931 x = 0,230 and y = 0,247) with a peak maximum at 426 nm and a vibronic replica at 447 nm. In Figure 5.13, the IV-characteristic and emission spectra at different device currents are shown. Table 5.3 displays the summarized results.

In comparison to the calculated CIE 1931 coordinates of the OLEDs with a thin (15 nm) fPF layer discussed in the paragraph above, a red-shift of the emission color into the light blue region is evident. In the CIE 1931 diagram in Table 5.3, the yellow triangle indicates the coordinates of the emission from the OLED with a thick fPF layer (57 nm). For comparison, the emission color of the OLED with a thin fPF layer is marked by a red triangle. The white arrow displays the shift of the emission into the light blue region due to the increased fPF layer thickness.
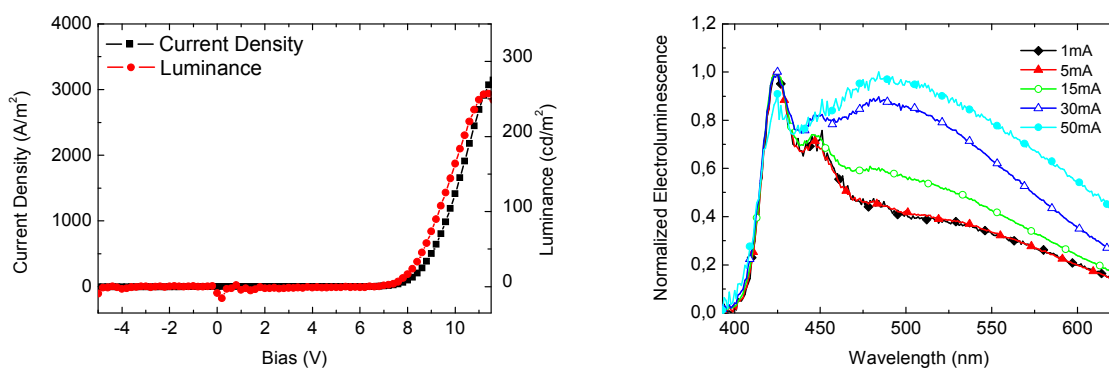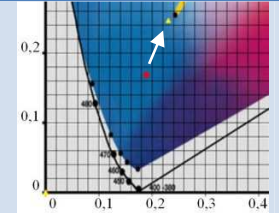


Figure 5.13: Current-voltage-luminance characteristic (left) and EL spectra (I-sweep; right) of an ITO/PEDOT:PSS/fPF(57 nm)/TPBi/Ca/Al device.

Table 5.3: Key results of ITO/PEDOT:PSS/fPF(57 nm)/Ca/Al device.

| Onset voltage | Maximum efficiency | Maximum luminance | Peak maximum | CIE 1931 coordinates | CIE 1931 diagram |
|---|---|---|---|---|---|
| ~6,9V | 0,177 cd/A | 257,0 cd/m$^2$ | 426 nm | x = 0,230 <br> y = 0,247 <br> (@ 9 V) |  |

**Origin of increased luminescence intensity in the region 500 nm to 600 nm**

Due to the unexpected change of the emission color when increasing the fPF layer thickness, measurements for the determination of the origin of the spectral change were performed. A microscope image of a fPF film, fabricated form a 5 g/l TFT solution, shows small particles with a diameter of about 3 μm in the film. The reason can be that the polymer does not dissolve properly. To enhance the dissolving process, the 10 g/l fPF solution was heated at 70°C for 24 h. To investigate if this heating leads to a thermal degradation of the polymer (which can be the reason for the change of the emission color of the OLED), a heated solution was prepared and spin coated onto a glass substrate. With this sample, PL and absorbance measurements were accomplished and compared to the data of a sample where an unheated solution was used. In Figure 5.14, the results of the PL and absorbance measurements are depicted. It is obvious that no mentionable differences can be seen. This is an indication that there is no thermal degradation process during heating the solution.
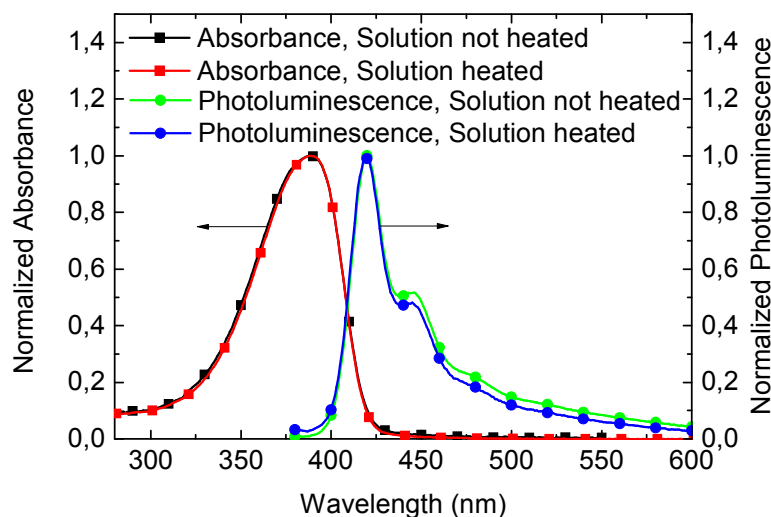


Figure 5.14: Comparison of PL and absorption spectra of a fPF film assembled with a heated (70°C) and unheated solution.

**Increasing layer thickness by using more viscous solvent**

In order to make further investigations of OLEDs with thick fPF layers, the solvent hexafluorobenzene was used instead of TFT. An advantage of hexafluorobenzene is its higher viscosity of 1,2 mPa s. For comparison, the viscosity of TFT is 0,55 mPa s. Due to this it is possible to achieve a higher level of thicknesses of the fPF layer, with lower solution concentration using hexafluorobenzene in comparison to TFT.

To investigate the effect of the new solvent, a series of OLEDs with the same layer assembly as shown before (ITO/PEDOT:PSS/fPF/TPBi/Ca/Al), but different fPF layer thicknesses were built and investigated. In total, fPF solution concentrations of 5, 7, 10 and 20 g/l were used, that lead to layers of 48, 69, 90, and 210 nm thickness. Again, IV-characteristic and spectrum measurements were performed.

The devices with an fPF layer thickness of 48 and 69 nm have similar luminance and efficiency values compared to the measurement results of the OLEDs, where a 10 g/l fPF solution - dissolved in TFT - was used for the fabrication of the fPF layer. Also the similarity of the emission spectra is obvious. This is plausible, because the thicknesses of the layers are in the same region.

The devices with a 90 and 210 nm thick fPF layer show a huge enhancement of the device efficiency and luminance values. However, the emission spectra give entirely different pictures. In the emission spectrum of the OLED with a 90 nm fPF film, the main peak at about 426 nm almost vanishes. The spectrum of the OLED with a 210 nm fPF film shows a strong increase of the intensity at about 530 nm and the intensity of the vibronic replica almost reaches the value of the main peak. In Figure 5.15 the EL spectra of the devices with different fPF layer thicknesses are depicted. Table 5.4 shows a summary of the measurement results.

One approach to explain the spectral change is to make a self-absorption effect responsible for this behavior. Another possible explanation is the appearance of a micro cavity effect.
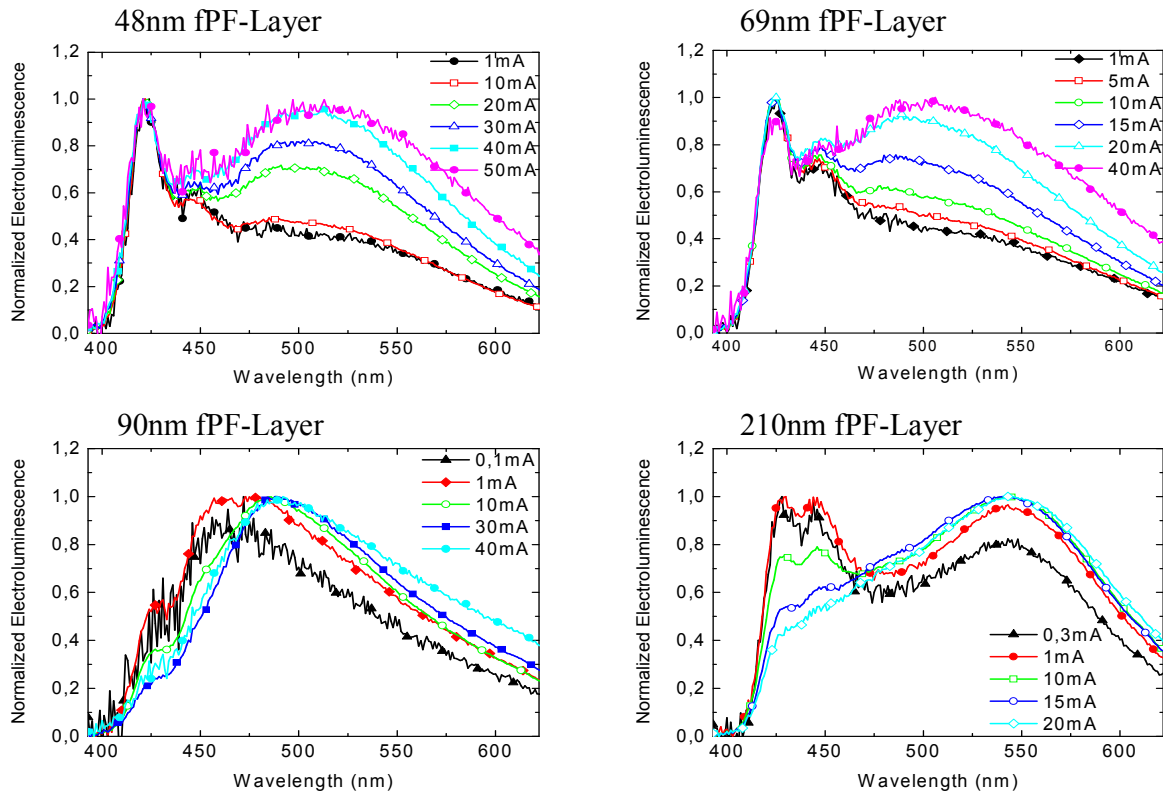
Figure 5.15: EL spectra (I-sweep) of ITO/PEDOT:PSS/fPF/TPBi/Ca/Al devices with different fPF layer thickness.

Table 5.4: Key results of ITO/PEDOT:PSS/fPF/TPBi/Ca/Al devices with different fPF layer thickness.

| fPF layer thickness | Onset voltage | Maximum efficiency | Maximum luminance | Peak maximum | CIE 1931 coordinates (@ 10 mA) |
|---|---|---|---|---|---|
| 48 nm (5 g/l) | ~5,4 V | 0,052 cd/A | 111,4 cd/m$^2$ | 422 nm | x = 0,223 y = 0,249 |
| 69 nm (7 g/l) | ~6,1 V | 0,157 cd/A | 169,8 cd/m$^2$ | 425 nm | x = 0,221 y = 0,233 |
| 90 nm (10 g/l) | ~9,0 V | 0,281 cd/A | 310,3 cd/m$^2$ | 482 nm | x = 0,229 y = 0,316 |
| 210 nm (20 g/l) | ~18,0 V | 0,714 cd/A | 363,8 cd/m$^2$ | 428 nm | x = 0,272 y = 0,336 |

**Investigation of self-absorption effect**

To investigate a possible self-absorption effect, a sample with a fPF layer was illuminated from one side with UV radiation (366 nm). On the other side of the sample, the detector head of a spectrometer was positioned (see Figure 5.16). Due to this position of the detector, only light

which traveled through the fPF layer is measured by the spectrometer. If self-absorption is responsible for the spectral change of the devices with thick fPF layers, one would expect a spectral change of the detected spectrum when increasing the fPF layer thickness. In Figure 5.17, the measured spectra of samples with 48, 90 and 210 nm thick fPF layers are shown. All three spectra look similar and show no distinct dependence from the layer thickness. Due to this, the results do not provide any evidence for a self-absorption effect.
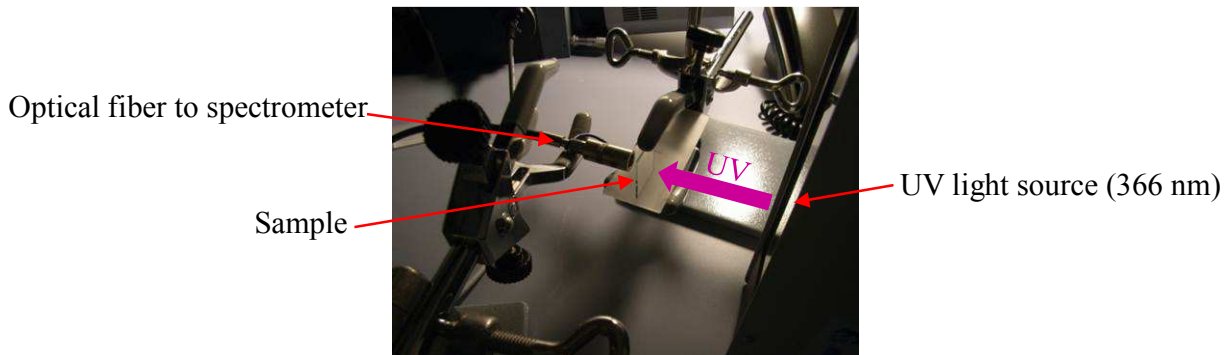


Figure 5.16: Measurement setup for the investigation of a self-absorption effect.
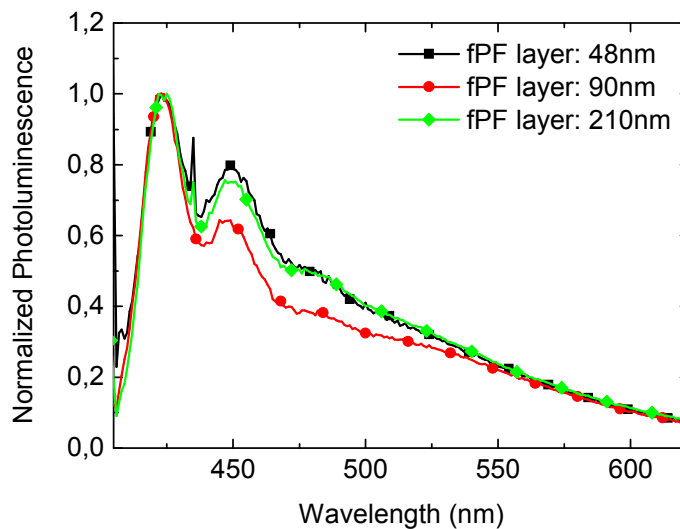


Figure 5.17: PL measurement results (by using the measurement setup shown in Figure 5.16) of samples with different thicknesses of the fPF layer.

**Investigation of micro cavity effect**

Due to the hetero layer structure of an OLED and reflections of light at the interfaces of adjacent layers, the possibility exists that multiple reflections can lead to constructive interference of light

beams (like in a Fabry-Perot-interferometer; see Figure 5.18) leading to a micro cavity effect. A prerequisite for this effect is the satisfaction of the equation

$$d = n \cdot \frac{\lambda}{2} \qquad n \in \aleph.$$

$d$ is the distance between the reflecting interfaces, $\lambda$ is the wavelength of the emitted light and $n$ is an integer. Among others, Bulovic et al. [77] and Dodabalapur et al. [78] reported about micro cavity effects in OLEDs. The effect, presented by Bulovic et al. shows only a small shift of the emission maximum by changing the thickness of the light emitting layer. In contrast, Dodabalapur et al. introduced an OLED, where the device was specifically engineered to lead to an as large as possible micro cavity effect. The emission spectrum of this device shows a very sharp peak at the decided wavelength. Due to these experimental results it can be speculated that an unwanted micro cavity effect is the origin of the spectral change.
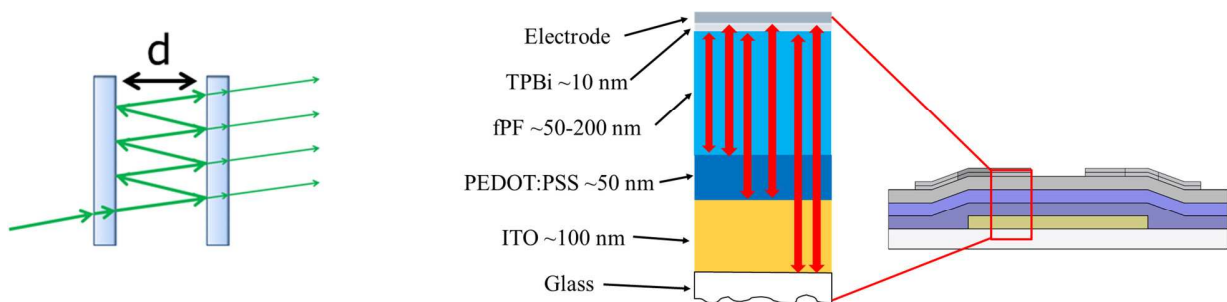


Figure 5.18: Left: sketch of a Fabry-Perot-interferometer leading to a standing wave inside the resonator if the distance $d = n \cdot \frac{\lambda}{2}$, where $n$ is an integer and $\lambda$ is the wavelength of light (taken from [79] and modified); right: different distances of interfaces inside an OLED having a potential as possible resonators leading to a micro cavity effect.

For verification, devices with the configuration ITO/PEDOT:PSS/fPF/TPBi/Ca/Al were assembled from fPF solutions with the concentrations 5, 7, 10 and 20 g/l using hexafluorobenzene as solvent. If a micro cavity effect is responsible for the spectral change, a modification should not only be visible in the EL spectrum, but also in the PL spectrum when exciting the fPF layer with UV light.
For the measurement, the OLED was fixed in the SHIMAZU RF-5301PC spectrofluorophotometer. The illumination of the OLEDs was done through the glass side. To ensure that the excitation light only hit the region of the polymer film that was covered by the electrode, an aperture was used. When the excitation of the fPF layer with UV light (365 nm) leads to a resonance effect inside the OLED (symbolized by the red double arrow on the left side of Figure 5.19), an enhancement of the intensity at a particular wavelength in the emission spectrum is expected. As an example, the EL and PL spectra of the device with a 200 nm thick

fPF layer are depicted on the right side of Figure 5.19. The EL spectrum shows a strong enhancement of the intensity at 530 nm. In contrast to this, no change in the PL spectrum at this wavelength is determinable. Also the PL spectra of the other investigated devices do not show any additional emission peaks. Due to these results there are no indications for a micro cavity effect to be the origin of the spectral change.
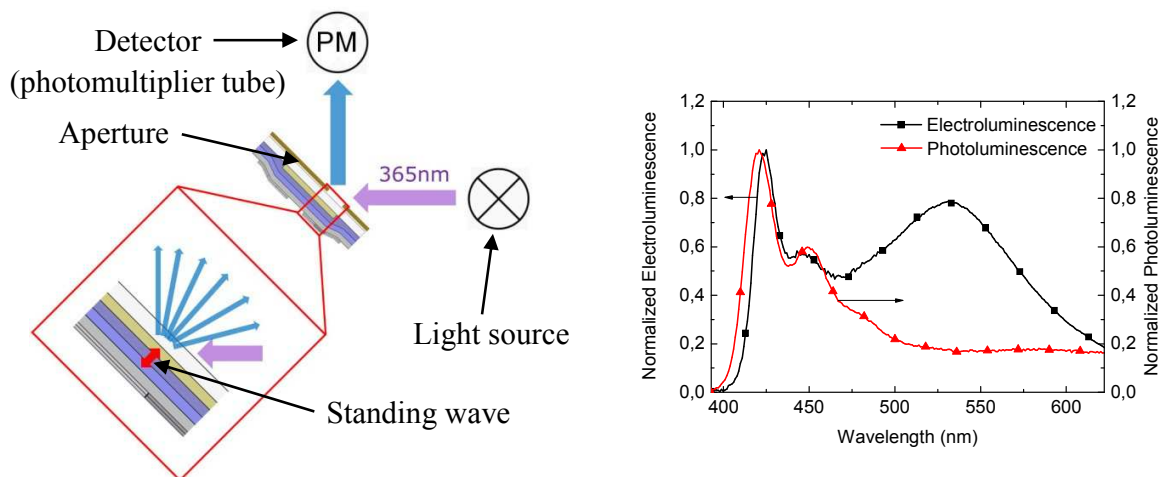


Figure 5.19: Left: measurement setup for verification of micro cavity effect by PL measurement; right: EL and PL emission spectra of device with the layer configuration glass/ITO/ PEDOT:PSS/fPF(200 nm)/TPBi/Ca/Al.

None of the experiments, shown in the last paragraphs, can explain the origin of the spectral modification. Another reason for the change of the emission spectrum can be an electrochemical degradation process, but it is up to further investigations and experiments to prove this possibility.

## 5.1.5 Multi layer OLED with fluorinated polyfluorene and MEHPPV

In this chapter, a detailed analysis of a multi layer OLED with two light emitting layers - one made of the blue emitter fPF and the other one made of the red emitter MEHPPV - is shown. The target was to cause a color switch through shifting the recombination zone between the two light emitting layers, using different electrode materials and applied voltages.

In general, when manufacturing multi layer OLEDs, the following points must be observed:

- Optical path: Light that is emitted from the electro active layer has to travel through all subsequent layers until it reaches the glass substrate and is coupled out to environment. It must be ensured that during this process the light is not absorbed by one of the layers.

- **Performance of single layer devices:** To be able to comment on the performance of the multi layer systems, the performances of the used polymers applied with a single layer device have to be determined.
- **Assembly of multilayer devices:** Finally, the assembly and investigation of multi layer devices can be started, where different electrode materials and different layer thicknesses of the electro active emitters are investigated.

**Optical path**

To be sure that emitted light from the fPF layer is not absorbed while propagating through the device (see Figure 5.20, left side), the absorption properties of the individual layers were investigated. Glass, ITO and PEDOT:PSS have low absorption values in the range of visible light, so the main concern was with the MEHPPV layer. In Figure 5.20 on the right side, the PL spectra of fPF and MEHPPV and the absorption spectrum of MEHPPV are depicted. Due to the broad absorption spectrum of the MEHPPV layer, with a maximum at about 500 nm, most of the intensity of the emitted light from the fPF layer with a wavelength higher than about 450 nm is absorbed, but the main peak around 420 nm should be detectable. Summarized, one can say that if a color switch can be induced, the detection is not inhibited by the absorption properties of the individual layers of the multi layer device.
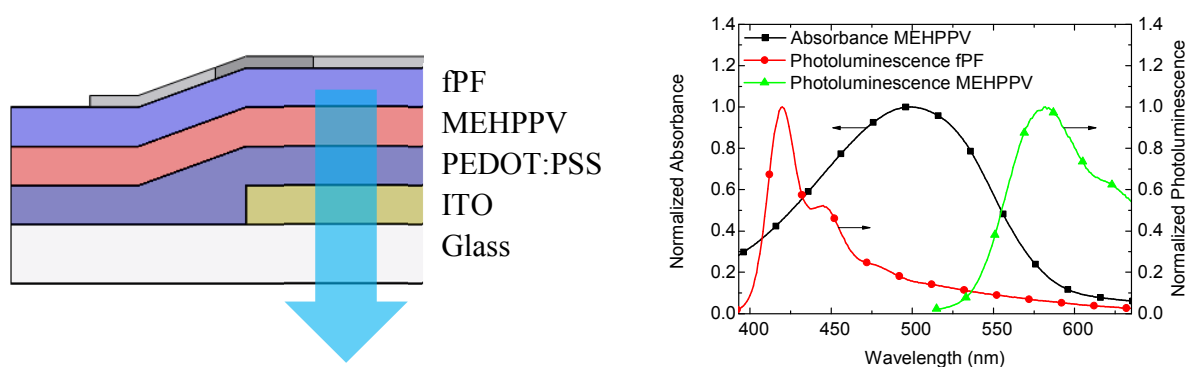


Figure 5.20: Left: sketch of optical path of light emitted from the fPF layer; right: PL spectra of fPF and MEHPPV film and absorption spectrum of MEHPPV film.

**Performance of single layer devices**

In chapter 5.1.4, the performances of fPF single layer devices have already been discussed. In the following, the results of single layer devices with MEHPPV as light emitting layer are presented. Two different layer assemblies were fabricated and investigated, ITO/PEDOT:PSS/MEHPPV/Al

and ITO/PEDOT:PSS/MEHPPV/TPBi/Ca/Al. The MEHPPV layer was deposited from a chloroform solution with a concentration of 5 g/l, leading to a layer thickness of about 55 nm.

The device with the layer configuration ITO/PEDOT:PSS/MEHPPV/Al shows a luminance value of 482,1 cd/m$^2$ and a device efficiency of 0,028 cd/A. Due to the additional TPBi layer, an enhancement of the efficiency to 0,778 cd/A and the luminance to 9.044 cd/m$^2$ is detected. A further consequence of the TPBi layer is the decrease of the onset voltage from 3 to 2 V. The emission spectra of both devices look almost the same with peak maxima at 594 nm in each case. Having a closer look at the spectrum, one can assess a spectral shift to a lower wavelength by increasing the current. Due to the given fact that previous measurements in another laboratory (with the same MEHPPV polymer charge) led to the same shift while increasing the current, this behavior can be traced back to a basic property of MEHPPV. [80] Figure 5.21 and Figure 5.22 depict the IV characteristics and the emission spectra at different operation currents. Table 5.5 shows a summary of the measurement results.
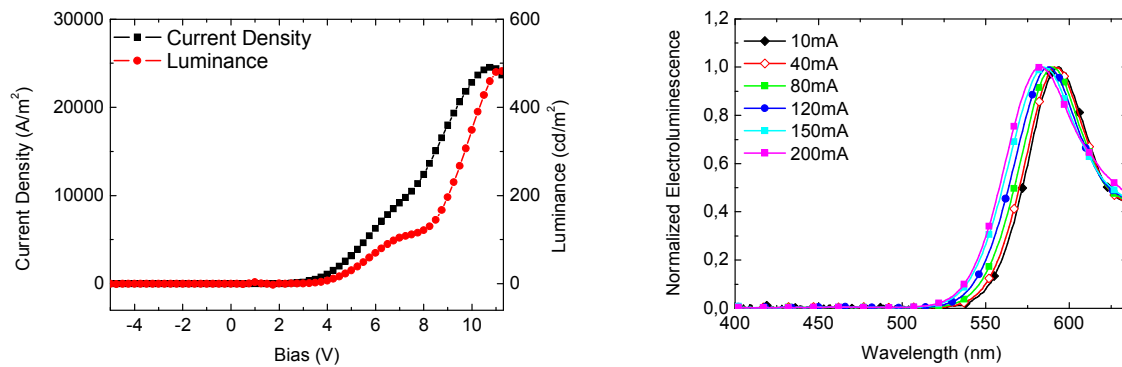


Figure 5.21: Current-voltage-luminance characteristic (left) and EL spectra (I-sweep; right) of ITO/PEDOT:PSS/MEHPPV/Al device.
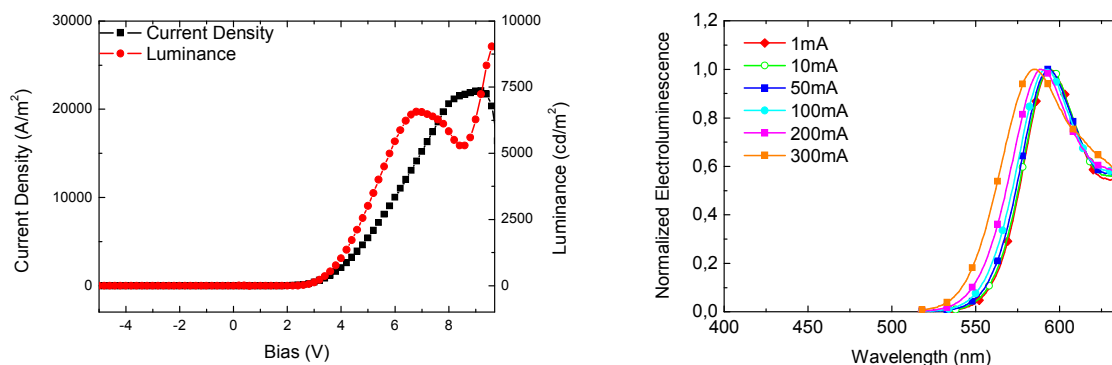


Figure 5.22: Current-voltage-luminance characteristic (left) and EL spectra (I-sweep; right) of ITO/PEDOT:PSS/MEHPPV/TPBi/Ca/Al device.

Table 5.5: Key results of ITO/PEDOT:PSS/MEHPP/Al and ITO/PEDOT:PSS/MEHPPV/TPBi/ Ca/Al devices.

| Layer configuration | Onset voltage | Maximum efficiency | Maximum luminance | Peak maximum |
|---|---|---|---|---|
| ITO/PEDOT:PSS/MEHPP/Al | ~3,0 V | 0,028 cd/A | 482,1 cd/m$^2$ | 594 nm |
| ITO/PEDOT:PSS/MEHPPV/TPBi/Ca/Al | ~2,0 V | 0,778 cd/A | 9.044 cd/m$^2$ | 594 nm |

**Assembly of multi layer devices**

Due to wettability problems (as shown in chapter 5.1.1) it is not possible to coat MEHPPV (dissolved in chloroform) onto a fPF layer. As a consequence, only multi layer devices were investigated, where the fPF layer was spin coated onto the MEHPPV layer. The fabricated devices had the layer configuration ITO/PEDOT:PSS/MEHPPV/fPF/TPBi/Ca/Al and ITO/PEDOT:PSS/MEHPPV/fPF/Al (see Figure 5.23). The fPF layer (~15 nm) was deposited from a 5 g/l TFT solution, for the fabrication of the MEHPPV layer (~55 nm), a 5 g/l chloroform solution was used.

Figure 5.24 shows the (not scaled) energy level diagrams of the two assembled multi layer devices. The HOMO and LUMO levels of fPF are unknown, but Sax et al. [61] used a polyfluorene (with known HOMO and LUMO levels of ~5,9 eV and ~2,7 eV), which has a similar chemical structure and photophysical behavior compared to the fPF. Lee at el. [81] showed that semifluorination of the alkyl side chains of their investigated polyfluorene influences the energy band gap by lowering the both the HOMO and LUMO levels in the order of magnitude of 0,1 eV. Due to these facts it is possible to get a rough idea about the positions of the HOMO and LUMO levels of fPF.

In both multi layer systems, an accumulation of holes at the MEHPPV-fPF-interface is expected due to an assumed energy barrier between the two HOMO energy levels. Using TPBi, calcium and aluminum instead of an aluminum electrode only, electrons can easily reach the MEHPPV layer without having to overcome high barriers. A main emission from the MEHPPV layer is expected due to the smaller band gap of this polymer. Using just aluminum as the top electrode, electrons have to overcome an energetically high barrier to be injected into the fPF layer. The intention of this configuration is that due to the accumulation of electrons at the interface of the Al-electrode and the fPF layer, an increased emission of the fPF layer can be achieved. Moreover, an attempt is being made to change the emission color of the device by shifting the recombination zone between the MEHPPV layer and the fPF layer when changing the applied electric field.
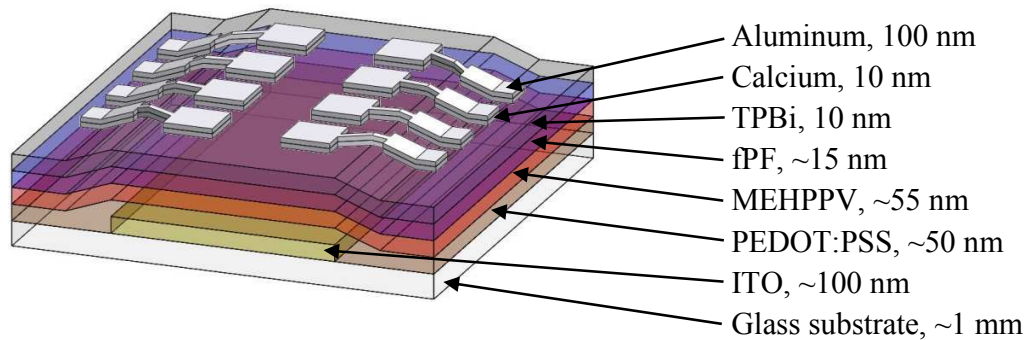
Figure 5.23: Assembly and thicknesses of the individual layers of the multi layer device with the layer configuration ITO/PEDOT:PSS/MEHPPV/fPF/TPBi/Ca/Al.
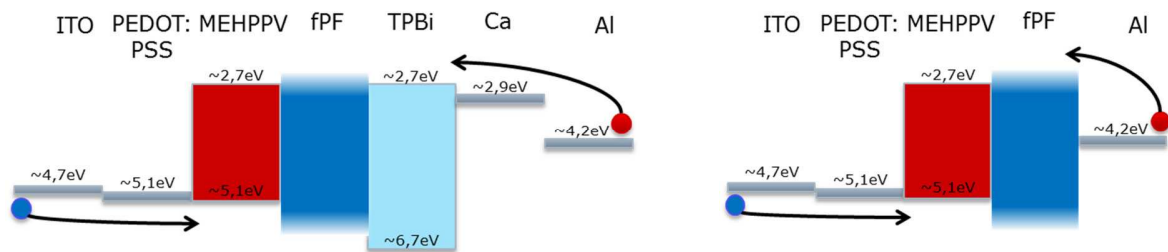


Figure 5.24: Energy level diagrams (not scaled) of assembled multi layer devices with the configurations ITO/PEDOT:PSS/MEHPPV/fPF/TPBi/Ca/Al and ITO/PEDOT:PSS/MEHPPV/fPF/Al, respectively.

The device with the layer configuration ITO/PEDOT:PSS/MEHPPV/fPF/Al shows an efficiency of 0,047 cd/A and a luminance value of 68,0 cd/m$^2$. Using a TPBi/Ca/Al top electrode, a device efficiency of 0,221 cd/A and a luminance value of 215,6 cd/m$^2$ is determined. Both devices show red emission with an emission peak at 594 nm (Al-electrode) and 597 nm (TPBi/Ca/Al-electrode). Increasing the applied electric field leads to a shift of the emission peaks to lower wavelengths. Due to the results of the investigated MEHPPV single layer devices, this attitude can be attributed to the basic property of MEHPPV. Taking a closer look at the inset in Figure 5.25 (right), a small increase in the intensity at 420 nm can be seen. Due to the fact that this wavelength corresponded with the emission maximum of fPF, the spectral feature can be attributed to the emission of the fPF layer. The device with the Al-electrode, shows a strong spectral change with increasing bias (Figure 5.25; left). The MEHPPV single layer device do not show any spectral changes in this wavelength region, so the origin of this emission is most likely caused by the fPF layer or an effect induced by the combination of the MEHPPV and the fPF layer.
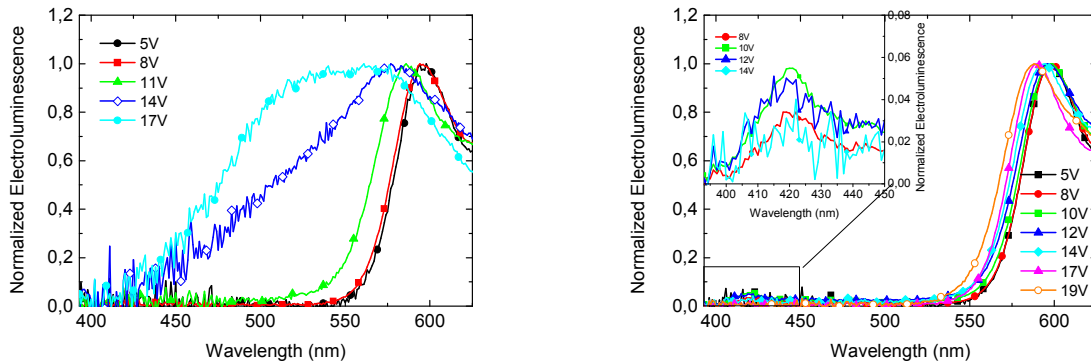
Figure 5.25: EL spectra at different applied voltages of ITO/PEDOT:PSS/MEHPPV (55 nm)/ fPF(15 nm)/Al (left) and ITO/PEDOT:PSS/MEHPPV(55 nm)/fPF(15 nm)/TPBi/Ca/Al devices (right). The inset in the right diagram shows an image enlargement of the emission spectrum, where the emission peak of fPF at 420 nm is visible.

Table 5.6: Key results of ITO/PEDOT:PSS/MEHPPV(55 nm)/fPF(15 nm)/Al and ITO/ PEDOT:PSS/MEHPPV(55 nm)/fPF(15 nm)/TPBi/Ca/Al devices.

| Layer configuration | Onset voltage | Maximum efficiency | Maximum luminance | Peak maximum |
|---|---|---|---|---|
| ITO/PEDOT:PSS/MEHPPV/fPF/Al | ~4,2 V | 0,047 cd/A | 68,0 cd/m$^2$ | 594 nm |
| ITO/PEDOT:PSS/MEHPP/fPF/TPBi/Ca/Al | ~3,6 V | 0,221 cd/A | 215,6 cd/m$^2$ | 597 nm |

Due to the strong spectral change of the device with the layer configuration ITO/PEDOT:PSS/MEHPPV/fPF/Al with increasing bias, a multi layer OLED with the same layer configuration was assembled again, but instead of using a 5 g/l TFT solution, a 10 g/l TFT solution was used to achieve a higher layer thickness of the fPF layer (55 nm), and thereby to increase the influence of the fPF layer to the emission spectrum of the device.

The achieved efficiency and luminance values (0,01 cd/A, 37,2 cd/m$^2$) decrease compared to the multi layer device with the same layer configuration, but with a thin (15 nm) fPF layer. This behavior can be explained by the enhanced influence of the fPF layer to the overall performance of the OLED. The device shows red emission with a peak maximum at 594 nm. At a wavelength of about 420 nm, a significant enhancement of the intensity is determined (see Figure 5.26) compared to the multi layer device with the thin fPF layer. By increasing the voltage, a shift to the lower wavelength of the emission peak (because of a basic property of MEHPPV) is determinable again. When a voltage higher than 14 V is applied, a strong shift of the emission maximum to lower wavelengths is measured.
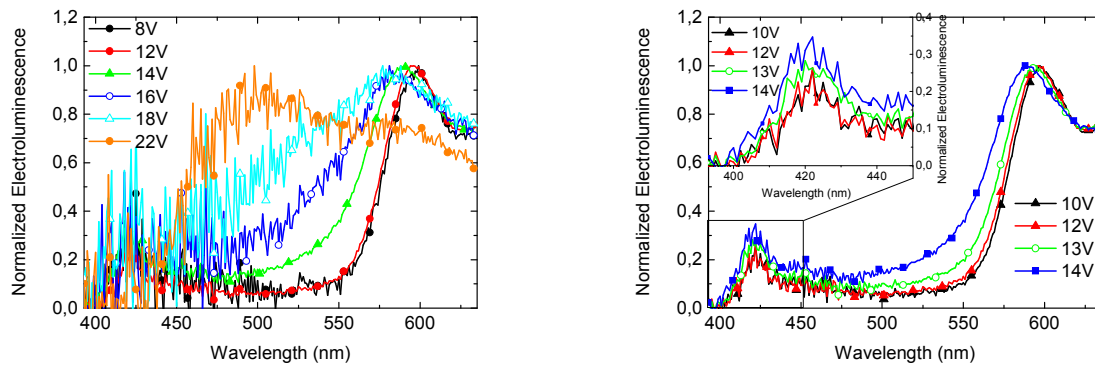
Figure 5.26: EL spectra at different applied voltages of ITO/PEDOT:PSS/MEHPPV(55 nm)/ fPF(55 nm)/Al device; left: EL spectra at voltages between 8 and 22 V. When the voltage value reaches or exceeds 14 V, a strong shift of the emission peak to lower wavelengths is visible; right: EL spectra at voltages between 10 and 14 V.

Table 5.7: Key results of ITO/PEDOT:PSS/MEHPPV(55 nm)/fPF(55 nm)/Al device.

| Layer configuration | Onset voltage | Maximum efficiency | Maximum luminance | Peak maximum |
|---|---|---|---|---|
| ITO/PEDOT:PSS/MEHPPV/fPF/Al | ~8,7 V | 0,01 cd/A | 37,2 cd/m$^2$ | 594 nm |

To investigate if the measured color switch is reversible, the EL spectrum of the OLED was measured while the voltage values 9 V and 16 V were applied alternately. Increasing the applied voltage from 9 V to 16 V, leads to a blue-shift of 15 nm of the emission peak. In the case of a reversible color switch, one expects to measure a red-shift of 15 nm, when decreasing the applied voltage to 9 V again. In contrast to this expectation, a further blue-shift is determined and the device shows a green emission. It seems reasonable to assume that the spectral change is not the result of a shift of the recombination zone, but of a degradation process during device operation.

As described earlier, the fPF single layer device shows an appearance of green emission during device operation because of a degradation process. Due to this, it is obvious to make the degradation process of the fPF layer responsible for the change of the emission color. However, there is still the question, why the emission of the MEHPPV layer decreases and why the green emission of the fPF layer is not absorbed during the propagation though the MEHPPV layer (which has an absorption maximum at 500 nm; see right side of Figure 5.27). A possible explanation is that not only the fPF layer shows degradation, but also the MEHPPV layer is damaged during device operation.

To determine a possible damage of the MEHPPV layer, two multi layer OLEDs (pad 1 and pad 2) with the layer configuration ITO/PEDOT:PSS/MEHPPV (55 nm)/fPF (55 nm)/Al were analyzed with the SHIMAZU RF-5301PC spectrofluorophotometer. Pad 2 was stressed via EL measurements by increasing the applied bias, until green emission was detectable. Pad 1 was also stressed by increasing the applied voltage, but the stressing procedure was stopped before green emission was determinable. The idea behind this investigation was to compare the PL spectra and

PL emission intensities of the emitted light of pad 1 and pad 2 when exciting the devices with light (365 nm: excitation of fPF layer; 500 nm: excitation of MEHPPV layer). If the MEHPPV layer of pad 2 is damaged, it is expected to measure a lower emission intensity compared to the emission intensity of pad 1. When exciting pad 1 with a wavelength of 365 nm, the PL spectrum should show peaks at about 420 nm (fPF layer) and also at 582 nm (MEHPPV layer). The emission of the MEHPPV layer is expected because on the one side, the MEHPPV layer shows small absorption at 365 nm which leads to an excitation. On the other side, one has to consider that light emitted from the fPF layer also excites the MEHPPV layer during the pass through. Exciting pad 2 at 365 nm should lead to a greenish emission.

For the PL measurements, the devices (pad 1 and pad 2) were fixed in the spectrofluorophotometer one after the other and illuminated through the glass side. To ensure that the excitation light only hits the region of the polymer films that are covered by the electrode, an aperture was fixed (see Figure 5.27; left). When exciting pad1 with a wavelength of 500 nm, the PL spectrum of the MEHPPV film can be measured. Using an excitation wavelength of 365 nm, peaks at 420 nm and 594 nm are visible. The excitation of pad 2 at 500 nm shows a braking-down of the emission intensity compared to pad 1. Comparing the PL spectra of pad1 and pad 2 at an excitation wavelength of 365 nm, pad 2 shows increased emission intensity in the range of 500 to 550 nm. All the results of the PL measurements (see Figure 5.28) are in line with the theoretical consideration about the spectral changes shown above and can be considered as evidences for the assumption, that during device operation, the MEHPPV layer is damaged and consequently green light – emitted from the degraded fPF layer – can be detected.
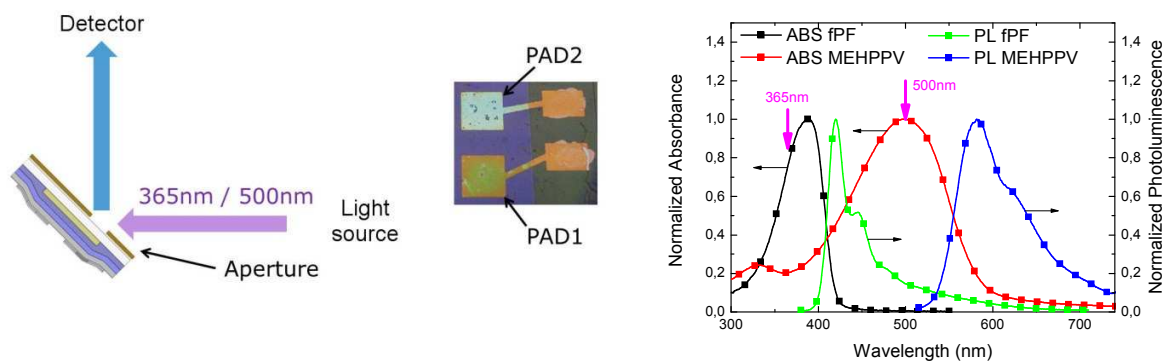


Figure 5.27: Left: a sketch of the measurement setup and a picture of both investigated devices (pad 1 and pad 2); right: absorption and PL spectra of fPF and MEHPPV in film. The pink arrows indicate the wavelengths used for the excitation of fPF (365 nm) and MEHPPV (500 nm).
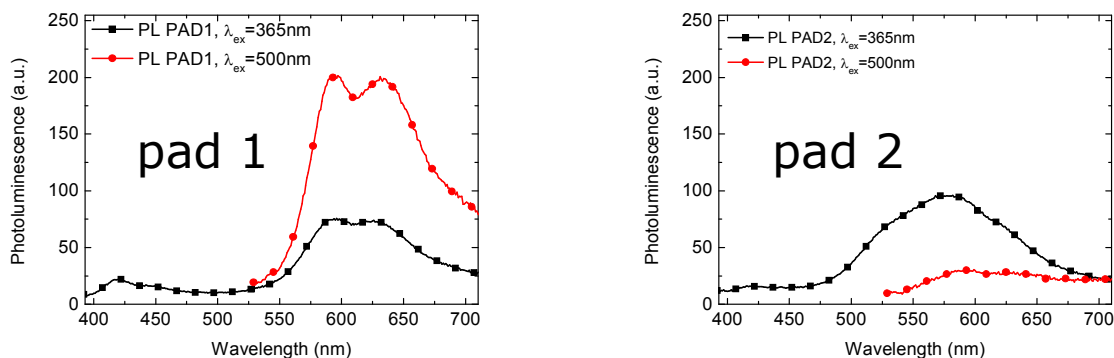
Figure 5.28: Left: PL spectra of pad 1, excited at 365 nm (black line) and 500 nm (red line); right: PL spectra of pad 2, excited at 365 nm (black line) and 500 nm (red line).

To summarize: Using different cathode materials (Al and TPBi/Ca/Al) leads only to a hardly measurable change of the emission color. When using only Al, a weak emission peak of fPF at 420 nm is detectable, using TPBi/Ca/Al as top electrode, the fPF emission peak is not measurable. When increasing the applied bias of the device with the layer configuration ITO/PEDOT:PSS/MEHPPV/fPF/Al, a substantial change of the emission spectrum is determinable. Detailed studies about the origin of the spectral change shows that a degradation of the fPF layer and a damage of the MEHPPV layer during device operation are responsible for the spectral change and therefore the color switch is not reversible.

## 5.1.6 Multi layer OLED with fluorinated polyfluorene and HTP

This chapter deals with the analysis of multi layer OLEDs with two blue emitting layers – one made of fPF and the other one made of HTP (which shows an enhanced hole transport characteristic). The target was to achieve an enhancement of the device efficiency due to an improved injection of holes and the accumulation of charge carriers at the interface between the HTP and fPF layer (to facilitate the formation of excitons). In addition, a blend system with fPF and HTP was fabricated and investigated.
As shown in the chapter before, the optical path and the performance of fPF and HTP single layer OLEDs had to be investigated, before starting the assembly of the multi layer system.

**Optical path**

The HTP film shows high absorption between 360 and 430 nm, with a maximum at 405 nm, the PL spectrum reveals a peak maximum at 435 nm and a vibrational maximum at 461 nm. The PL spectrum of the fPF film (with an emission peak at 426 nm) and the absorption spectrum of the HTP film show a strong overlap in the area of 405 to 430 nm. Therefore it is expected, that the emission of the fPF film in this wavelength range is mostly absorbed by the HTP film. Due to this

73

one anticipates that the emission of the multi layer device shows an emission peak in the region of the emission maximum of HTP. In Figure 5.29 on the right side, the PL spectra of fPF and HTP in film and the absorption spectrum of HTP in film [31] are depicted. The left side of Figure 5.29 shows a sketch of the optical path of light emitted from the fPF layer.
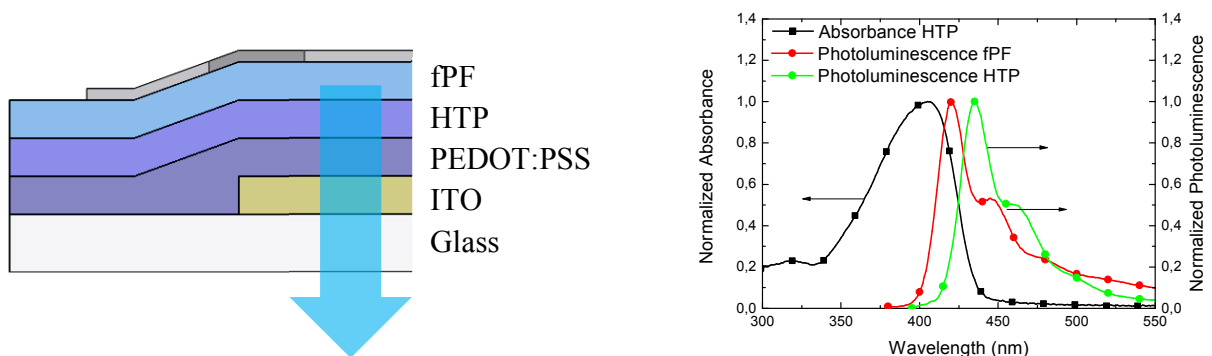


Figure 5.29: Left: sketch of the optical path of light emitted from the fPF layer; right: PL spectra of fPF and HTP in film and absorption spectrum of HTP in film [31].

**Performance of single layer devices**

In chapter 5.1.4, the performance of fPF single layer device was already discussed. In the following, the results of a single layer device with HTP as light emitting layer and the layer configuration ITO/PEDOT:PSS/HTP/TPBi/Ca/Al are presented. The HTP layer was deposited from a toluene solution with a concentration of 3 g/l, leading to a layer thickness of about 20 nm. The device shows a moderate maximal luminance value of 123,3 cd/m$^2$ and a rather poor efficiency of 0,005 cd/A. However, the EL emission exhibits deep blue emission (CIE 1931 x = 0,157 and y = 0,043) with a maximum at 433 nm and a shoulder at around 462 nm. Figure 5.30 depicts the IV characteristic and the emission spectra at different operation currents of the device. Table 5.8 shows a summary of the measurement results.
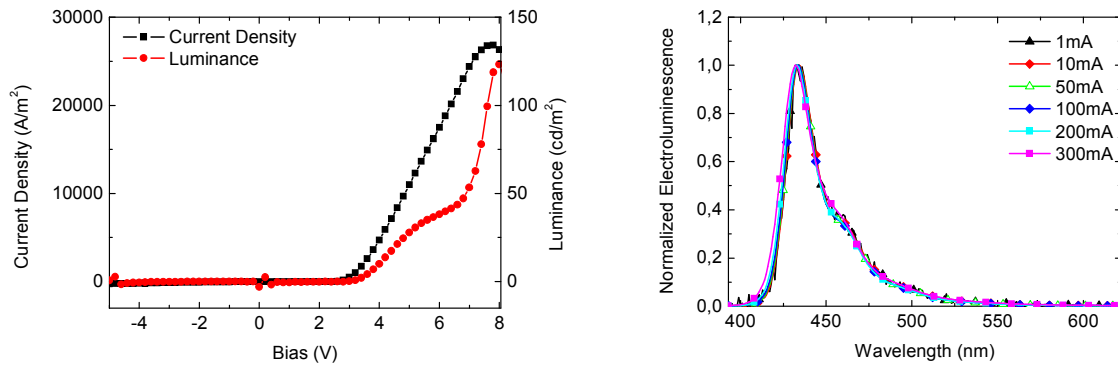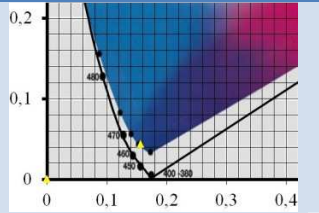
Figure 5.30: Current-voltage-luminance characteristic (left) and EL spectra (I-sweep; right) of ITO/PEDOT:PSS/HTP/TPBi/Ca/Al device.

Table 5.8: Key results of ITO/PEDOT:PSS/HTP/TPBi/Ca/Al device.

| Onset voltage | Maximum efficiency | Maximum luminance | Peak maximum | CIE 1931 coordinates | CIE 1931 diagram |
|---|---|---|---|---|---|
| ~2,8V | 0,005 cd/A | 123,3 cd/m$^2$ | 433 nm | x = 0,156 y = 0,043 (@ 10 mA) |  |

**Assembly of multi layer devices**

*Layer system*

As it was presented in chapter 5.1.4, the fPF single layer devices show poor device efficiencies. One possible reason for the poor efficiencies can be the propagation of charge carriers through the fPF layer to the opposite electrode without forming excitons.

Sax et al. [61] showed that an enhancement of the device efficiency can be achieved by using a bilayer structure consisting of two OSCs with the same LUMO levels and similar, but not exactly the same HOMO levels. The difference between the HOMO levels leads to a small barrier for holes, which in turn leads to an accumulation of holes in the layer with the higher HOMO level at the interface of the two polymer layers. Due to this accumulation, the probability for the formation of excitons is increased and an enhancement of the device efficiency is achieved.

To investigate if it is also possible to enhance the device efficiency of the fPF single layer OLED by using a bilayer structure, HTP was used as additional layer to fabricate a multi layer device with the layer configuration ITO/PEDOT:PSS/HTP/fPF/TPBi/Ca/Al. The idea was to enhance

the device efficiency by using the effect of charge carrier accumulation at the interface between the HTP and the fPF layer. In addition, the HTP layer should enhance the hole injection.

The fPF layer (~75 nm) was deposited from a 10 g/l TFT solution, for the fabrication of the HTP layer (~20 nm), a 3 g/l toluene solution was used. The whole device structure, including the thicknesses of the individual layers, is depicted in Figure 5.31.
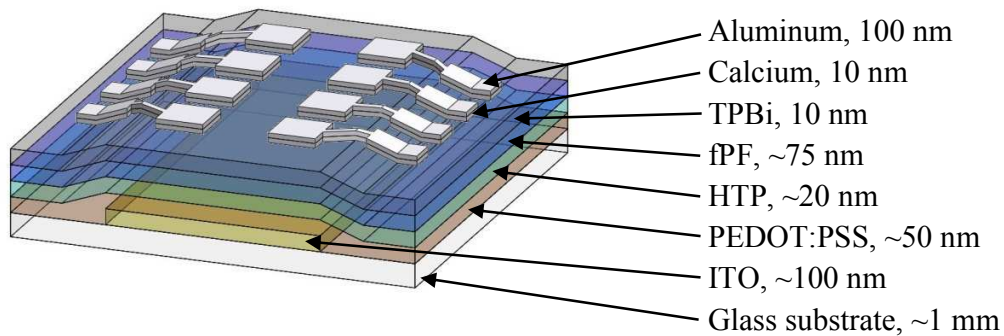


Figure 5.31: Assembly and thicknesses of the individual layers of the multi layer device.

In comparison to the fPF and HTP single layer devices, which show device efficiencies of 0,177 cd/A and 0,005 cd/A, an enhancement of the efficiency to 0,239 cd/A can be achieved when using a bilayer structure of fPF and HTP. The multi layer device reaches a luminance value of 376,1 cd/m$^2$, which is also an enhancement compared to the luminance values of the single layer devices (fPF: 257,0 cd/m$^2$; HTP: 123,3 cd/m$^2$). Blue EL emission is found (CIE 1931 x = 0,174 and y = 0,146) with emission peaks at 438 nm and 461 nm. The positions of the peaks correspond quite well to the peak positions of the emission spectrum of the HTP single layer device (433 nm and 462 nm). The intensity ratio between the peak at 433 nm and 462 nm of the HTP single layer device is 3,5:1. In contrast to this, the peaks of the emission spectrum of the multi layer device exhibit an intensity ratio of almost 1:1. A possible reason for the change of the intensity ratio can be a molecular interaction at the interface of the HTP and the fPF layer. As expected, the emission peak of fPF at about 426 nm is not determinable most likely due to the absorption of the HTP layer. Figure 5.32 shows the corresponding current-voltage-luminance characteristics and the emission spectra at different operation currents. Table 5.9 presents the key results of the ITO/PEDOT:PSS/HTP/fPF/TPBi/Ca/Al device.
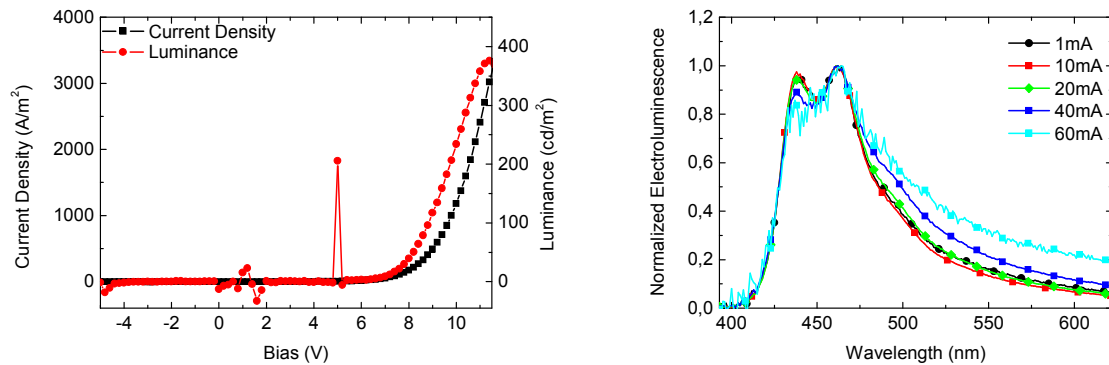
Figure 5.32: Current-voltage-luminance characteristics (left) and EL spectra (I-sweep; right) of ITO/PEDOT:PSS/HTP/fPF/TPBi/Ca/Al device.

Table 5.9: Key results of ITO/PEDOT:PSS/HTP/fPF/TPBi/Ca/Al device.

| Onset voltage | Maximum efficiency | Maximum luminance | Peak maximum | CIE 1931 coordinates | CIE 1931 diagram |
|---|---|---|---|---|---|
| ~6,2 V | 0,239 cd/A | 376,1 cd/m$^2$ | 461 nm | x = 0,174 y = 0,146 (@ 10 mA) |  |

*Blend system*

Another possibility to enhance the device efficiency of OLEDs using polyfluorene with fluorinated side chains was shown by Lee et al. [81]. They investigated semiperfluoroalkyl polyfluorenes as emitter materials for OLEDs. Due to the poor efficiency of the devices, they assumed that the introduction of semiperfluoroalkyl groups in the polymer film leads to charge traps adversely affecting the charge transport. Experiments with adding a small portion of electron-accepting comonomers led to an enhancement of the EL performances.

It was not possible to change the molecular structure of fPF (adding of electron-accepting comonomers), but due to the results shown by Lee et al., the idea was to combine fPF and the hole transport material HTP in a blend system in order to improve the charge transport in the light emitting layer and therefore, to increase the device performance.

In addition, the blend system opens up the opportunity for a FRET between the fPF and HTP molecules due to the strong overlap of the PL spectrum of fPF and the absorption spectrum of HTP and can have a positive effect to the device efficiency. For the sake of completeness, it has to be mentioned that in the case of the layer system shown above, the possibility for a FRET at the interface of the fPF and HTP layer exists too. If the FRET is primarily responsible for the

efficiency enhancement of the layer system, one expects that an increase of the efficiency by using a blend system can be achieved too.

The solvents TFT and toluene are miscible, which is important for the preparation of an HTP:fPF solution for the fabrication of the blend system. Two 10 g/l HTP:fPF solutions with a mixing ratio of 1:1 and 10:1 (10 parts of fPF, one part of HTP) were prepared. The solution with the mixing ratio of 10:1 showed the precipitation of one polymer, but the mixture with a ratio of 1:1 yielded a clear solution. The precipitated polymer was soluble in toluene, which was a first indication that HTP was precipitated. A PL measurement of the solution confirmed this assumption. Fabricating a light emitting layer from a 10 g/l HTP:fPF solution with a mixing ratio of 1:1, leads to a layer thickness of about 60 nm.

In comparison to the fPF (257,0 cd/m$^2$) and HTP (123,3 cd/m$^2$) single layer device, the blend system shows a luminance value of 120,5 cd/m$^2$. The device efficiency of 0,052 cd/A is better compared to the HTP single layer device (0,005 cd/A), but worse than the efficiency of the fPF single layer device (0,177 cd/A). Blue emission is determinable (CIE 1931 x = 0,152 and y = 0,084) with peaks at 437 nm and 463 nm. The emission spectrum looks similar to the emission spectrum of the layer system ITO/PEDOT:PSS/HTP/fPF/TPBi/Ca/Al, but with considerably lower emission intensity in the wavelength range 470 to 600 nm compared to layer system. The absence of the fPF emission peak at 426 nm is an indication for a possible FRET between the fPF and HTP molecules, because - differently to the layer system - the blend system does not exhibit an individual HTP layer which can be responsible for the absorption of the fPF emission peak. Figure 5.33 shows the current-voltage-luminance characteristic and EL spectra. In Table 5.10, the most important results are depicted.
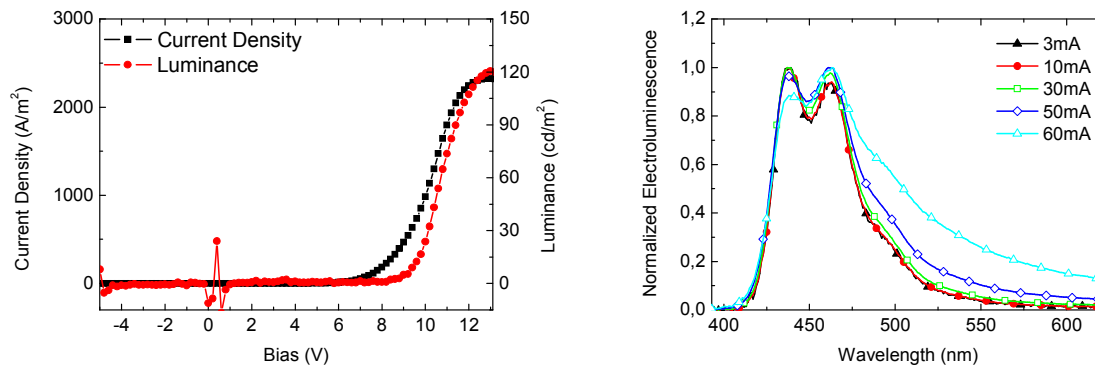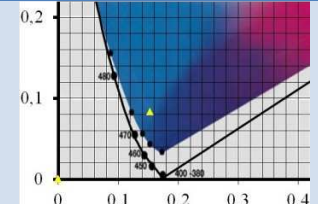


Figure 5.33: Current-voltage-luminance characteristic (left) and EL spectra (I-sweep; right) of ITO/PEDOT:PSS/HTP:fPF (1:1)/TPBi/Ca/Al device.

Table 5.10: Key results of ITO/PEDOT:PSS/HTP:fPF (1:1)/TPBi/Ca/Al device.

| Onset voltage | Maximum efficiency | Maximum luminance | Peak maximum | CIE 1931 coordinates | CIE 1931 diagram |
|---|---|---|---|---|---|
| ~8,3 V | 0,052 cd/A | 120,5 cd/m$^2$ | 437 nm | x = 0,152 y = 0,084 (@ 10 mA) |  |

**Overview of measurements results**

In summary it can be said that the layer system (ITO/PEDOT:PSS/HTP/fPF/TPBi/Ca/) shows the most promising results concerning the enhancement of the device efficiency and device luminance. Due to the fact, that the device efficiency of the blend system is only about one quarter of the efficiency shown by the layer system, it can be assumed, that not a FRET between the fPF and HTP molecules, but the accumulation of charge carriers at the interface of the HTP and fPF layer is primarily responsible for the efficiency enhancement. To obtain a better overview of the performances of the HTP and fPF single layer devices and the layer and blend systems of HTP and fPF, a summary of the maximum efficiency and luminance values and the corresponding emission colors (depicted by marks in a CIE 1931 diagram; measured at a device current of 10 mA) are shown in Figure 5.34.

*fPF single layer system*
Max. eff.: 0,177 cd/A (@ 7,8 V)
Max. lum.: 257,0 cd/m$^2$ (@ 11,4V)
Lum. @ 8/9/10 V: 16,6/73,5/163,7 cd/m$^2$

*HTP + fPF coating system*
Max. eff.: 0,239 cd/A (@ 9 V)
Max. lum.: 376,1 cd/m$^2$ (@ 11,4V)
Lum. @ 8/9/10 V: 39,4/117,3/234,1 cd/m$^2$

*HTP + fPF blend system*
Max. eff.: 0,052 cd/A (@ 13 V)
Max. Lum.: 120,5cd/m$^2$ (@ 13 V)
Lum. @ 8/9/10 V: 0,8/4,8/23,7 cd/m$^2$

*HTP single layer system*
Max. Eff.: 0,005 cd/A (@ 8 V)
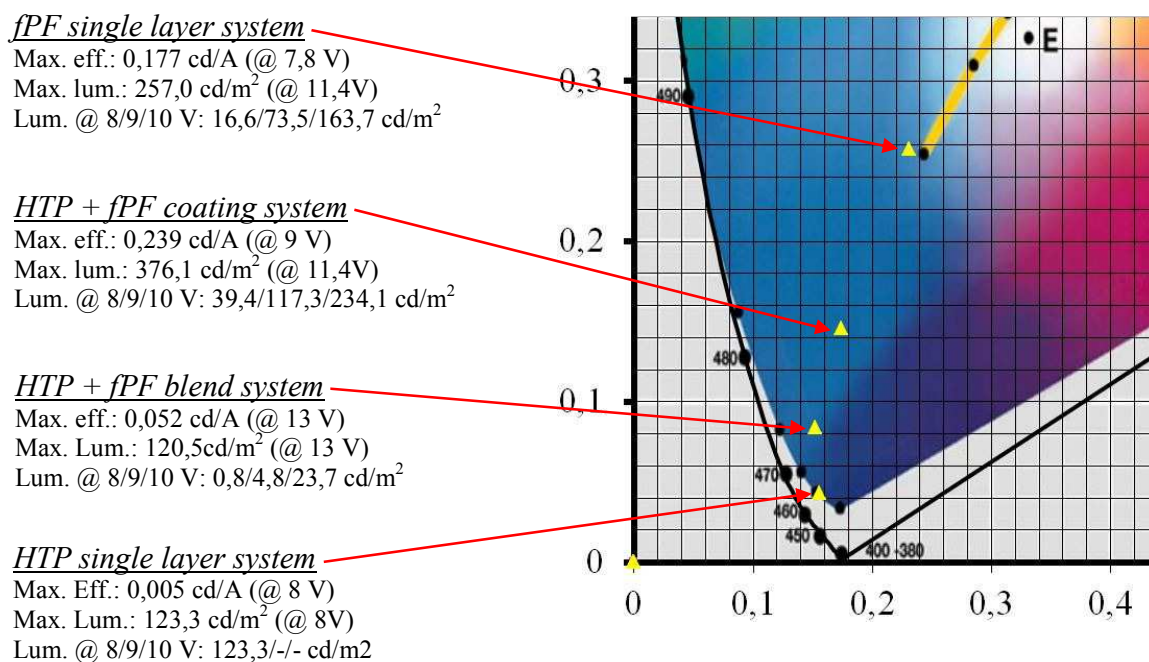Max. Lum.: 123,3 cd/m$^2$ (@ 8V)
Lum. @ 8/9/10 V: 123,3/-/- cd/m2

Figure 5.34: Maximum efficiency, luminance values and the corresponding applied voltage values and emission colors (CIE 1931 diagram; measured at a device current of 10 mA) of single and multi layer systems using HTP and fPF are shown. Additionally the luminance values at 8, 9 and 10 V are listed.

## 5.1.7 Summary and discussion

The novel polymer fluorinated polyfluorene (fPF) was investigated concerning its PL and absorption spectrum in solution and in film, the quantum yield in solution and experiments concerning thermal stress and stress due to exposure to UV light were determined. The PL spectrum shows peaks at 412 nm (solution) and 420 nm (film), respectively. The peak maximum of the absorption spectrum is found at a wavelength of 386 nm (solution) and 388 nm (film), respectively. The quantum yield shows a high value of 99%. Only thermal stress under ambient conditions leads to a distinct change of the PL spectrum (appearance of an emission peak at about 540 nm) which can be explained by the Keto defect.

The usage of fPF as light emitting layer in an OLED leads to a poor device efficiency and luminance value ($8 \cdot 10^{-4}$ cd/A; 7,68 cd/m$^2$). By increasing the thickness of the fPF layer (15 nm $\rightarrow$ 57 nm), an enhancement of the efficiency and luminance is achieved (0,177 cd/A; 257 cd/m$^2$). Before staring the fabrication of multi layer devices, investigations concerning the wettability and the dissolving of the polymer films, the optical path and the performance of the polymers used as light emitting layers in single layer OLEDs were investigated.

To obtain a color switch, the blue emitting fPF was combined with the red emitting polymer MEHPPV. An investigation concerning dissolving revealed that 90% of the MEHPPV layer

thickness is left after spin coating the fPF layer. A color switch is obtainable, but further investigations showed that this change of the emission color can be traced back to the degradation of the fPF layer and a damage of the MEHPPV layer. So it is not reversible. Changing the top electrode material has only a small, hardly provable, influence on the emission color.

A further attempt was to combine fPF with a blue emitting polymer with an enhanced hole transport characteristic (HTP). The target was to achieve an enhancement of the device efficiency due to an improved injection of holes and the accumulation of charge carriers at the interface between the HTP and fPF layer (to facilitate the formation of excitons). The multi layer device shows a device efficiency enhancement of about 35%, compared to the fPF single layer device. Also a blend system (mixture ration of fPF and HTP: 1:1) was investigated to determine if HTP can be used to improve the charge transport in the light emitting layer and therefore to increase the efficiency or if a possible FRET between the fPF and HTP molecules can have a positive effect to the device efficiency, but an enhancement of the efficiency and luminance is not achieved compared to the fPF single layer device.

## 5.2  Multi layer OLEDs with PEGylated polyfluorene

While in chapter 5.1, fluorinated solvents (TFT and hexafluorobenzen) in combination with toluene and chloroform formed pairs of orthogonal solvents, in this chapter, the pair of orthogonal solvents is formed by polar alcohol (methanol; polarity index 6,6 [82]) and non-polar toluene (polarity index 2,3 [82]). One polymer used for the assembly of multi layer OLEDs, was a novel PEGylated polyfluorene (PEGPF), which shows solubility in methanol (MeOH). The other electro active material was an already determined blue emitting poly(indenofluoren)-based polymer (PIF; soluble in toluene). In the following subchapter, the investigations concerning the wettability and the dissolving of the PIF film, when applying MeOH, is presented. Afterwards, the experiments for the determination of the PEGPF properties are explained and finally the measurements results of the fabricated multi layer systems are shown.

### 5.2.1  Multi layer systems - determination of wettability and dissolving

As explained above, the polymers PIF and PEGPF were used for the fabrication of two light emitting layers for the assembly of multi layer OLEDs with the device configurations ITO/PEDOT:PSS/PIF/PEGPF/Ca/Al         and         ITO/PEDOT:PSS/PIF/PEGPF/TPBi/Ca/Al (see Figure 5.35).
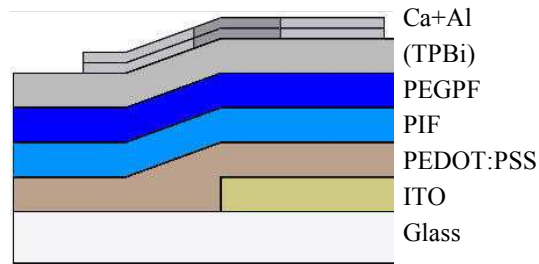
Figure 5.35: Sketch of the layer sequences of the investigated multi layer OLEDs using PEGPF and PIF as light emitting layers.

In the following, results of experiments are shown to point out, if it is even possible to coat the light emitting layers on top of each other (PEGPF film onto PIF film) by solution based manufacturing, and if so, to answer the question if there is a damage of the PIF film when applying the PEGPF solution during the spin coating process.

**Contact angles and surface energies**

The surface energies of the PIF layer and the used solvent for coating (MeOH) are listed in Table 5.11.

Table 5.11: Surface energies (SE) of PIF layer and MeOH.

|  | **PIF layer** | **Methanol [83]** |
|---|---|---|
| **SE (in mN/m)** | 24,94 | 22,70 |

The measured contact angle of MeOH on the PIF film was 24,9°. This value is quite high. However, due to the fact that the surface energy of the PIF layer is higher than the surface energy of MeOH, a successful assembly of the PEGPF layer by spin coating onto the PIF layer was expected.

**Dissolving**

The investigations concerning the influence of dissolving the polymer layer during the spin coating process showed that after treating the PIF layer with the solvent MeOH, about 70% of the layer thickness is left. In Figure 5.36, pictures of the investigated PIF film are shown. The areas, which were stressed with MeOH, are labeled with yellow markings.
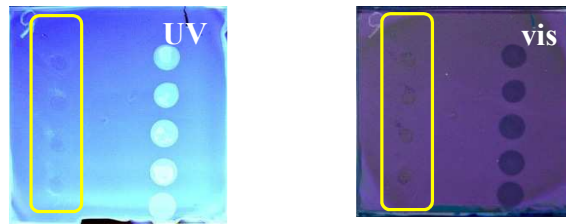
Figure 5.36: Pictures of PIF film taken during illumination with UV light and visible light after stressing with the solvent MeOH. The yellow markings label the regions, where the PIF layer was stressed by applying MeOH.

## 5.2.2 Chemical structures of PEGylated polyfluorene and polyethylene glycol

In Figure 5.37 on the left side, the chemical structure of PEGlyted polyfluorene (PEGPF) is shown. Via PEGylation, polyethylene glycol polymer chains (PEG) are covalently bonded to the target molecule. [84] On the right side of Figure 5.37, the chemical structure of PEG is depicted. As already explained before, PEGPF is soluble in alcohol.
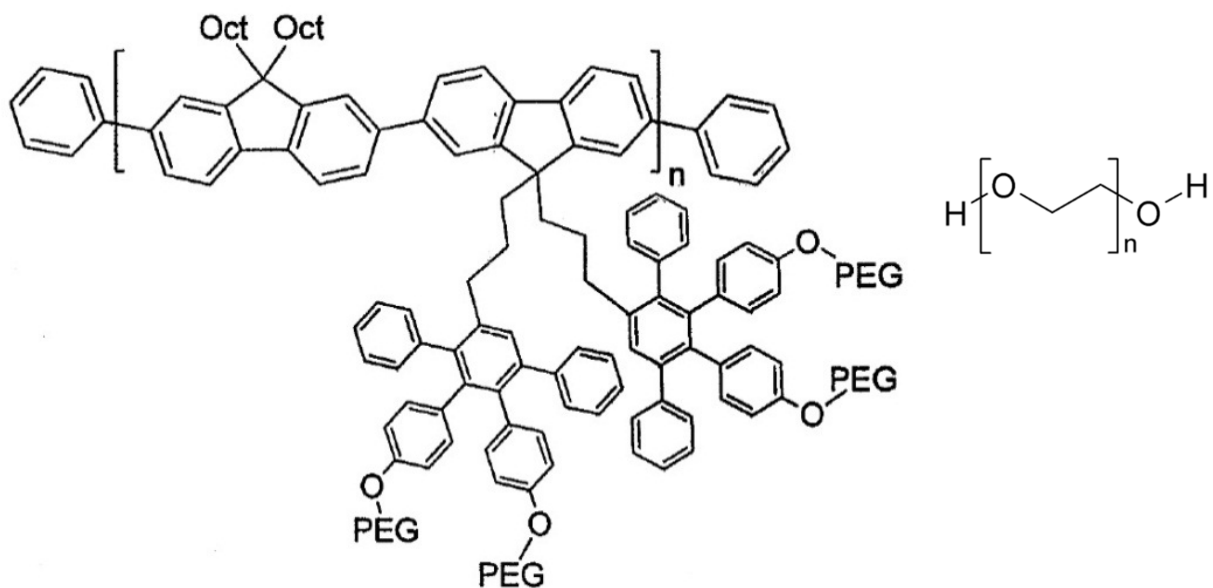


Figure 5.37: Left: chemical structure of PEGlyted polyfluorene; right: chemical structure of polyethylene glycol (taken from [85]).

## 5.2.3 Photo physical characterization of PEGylated polyfluorene

In this chapter, the photo physical properties of PEGPF will be shown. This includes absorption and emission spectra of the polymer in film and in solution. Additionally, the measured and calculated photoluminescence quantum yield is given.

**Absorption, emission and quantum yield of PEGylated polyfluorene**

Prior to processing and measuring, the PEGPF solutions were stirred for 24 hours to facilitate a completely dissolving of the polymer.

The PL spectrum of PEGPF in film shows a peak maximum at 425 nm and vibronic fine structures at 450 nm and 483 nm. The absorption spectrum has a maximum at 400 nm and does not exhibit a vibronic fine structure (Stokes shift: 25 nm). In contrast to the film emission, the emission maximum of PEGPF in solution shows a blue-shift due to solvatochromism and appears at 423 nm with vibronic fine structures at 448 nm and 480 nm. The absorption spectrum shows a maximum at 402 nm (Stokes shift: 21 nm). In Figure 5.38, the absorption and PL spectra of PEGPF in film and in solution are depicted.
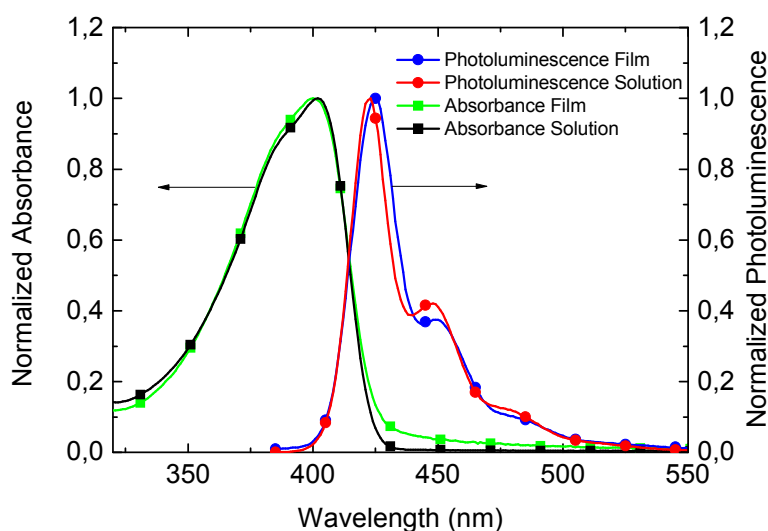


Figure 5.38: Absorption and PL spectra of PEGPF in solution and in film.

In Figure 5.39, the integrated corrected photoluminescence and the corresponding absorbance values of PEGPF solutions with different concentrations ($10^{-3}$, $5 \cdot 10^{-3}$ and $10^{-2}$ g/l) are shown as red squared data points. The linear fit of the data points is indicated by the red line. Quinine sulfate dehydrate was used again as quantum yield standard and the calculated

photoluminescence quantum yield of PEGPF in solution is 106%. Of course, a quantum yield above 100% is not allowed by the law of physics, but an error up to 10% must be considered.
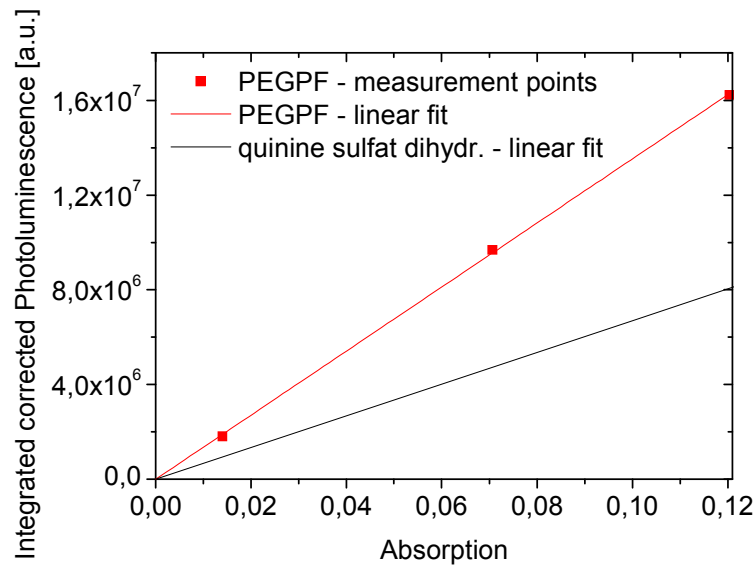


Figure 5.39: Measured points (red squares) and linear fit (red line) of PEGPF, linear fit of quinine sulfate dihydrate (black line) **[31]**.

## 5.2.4 Single layer OLED with PEGylated polyfluorene

For the investigation of PEGPF single layer OLEDs, two different configurations were fabricated The layer structure of the first device was ITO/PEDOT:PSS/PEGPF/Ca/Al. For the second device, an additional 10 nm thick TPBi layer was used (ITO/PEDOT:PSS/PEGPF/TPBi/Ca/Al; see Figure 5.40). The PEGPF layer was deposited from a MeOH solution with a concentration of 5 g/l, leading to a layer thickness of about 65 nm.
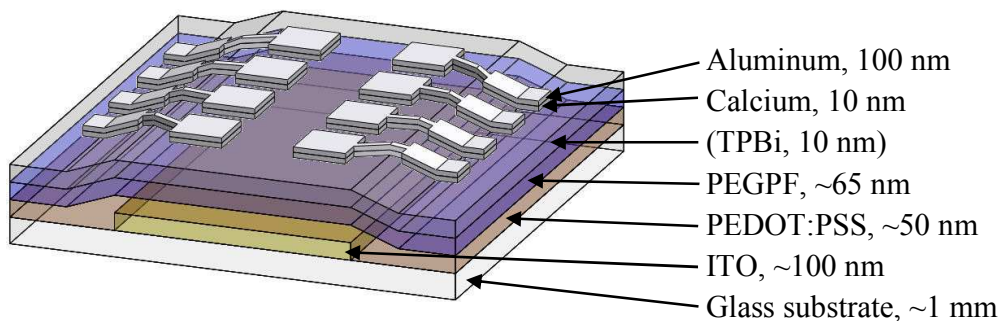


Figure 5.40: Assembly and thicknesses of the individual layers of the single layer OLED.

*PEGPF single layer device (ITO/PEDOT:PSS/PEGPF/Ca/Al)*

In the voltage range of 3 V to 6,5 V, the device with the layer configuration ITO/PEDOT:PSS/ PEGPF/Ca/Al shows a poor device efficiency of 0,006 cd/A and a maximal luminance of about 80 cd/m$^2$. Applying a voltage higher than 6,5 V leads to a strong increase of the luminance up to 238,7 cd/m$^2$ (flash) and is followed by a totally breakdown of the intensity and destruction of the device. In this short period, the efficiency increases to about 0,3 cd/A, but this is of no significance, due to a not stable operation of the OLED. The device shows blue emission (CIE 1931 x = 0,164 and y = 0,079) with a maximum at 425 nm. Performing a current sweep, the emission spectrum stays almost the same for current values from 15 to 100 mA. Only after applying a device current of 200 mA, a distinct change of the emission spectrum is examined. In Figure 5.41, the IV-characteristic and emission spectra are shown. In Table 5.12, the summarized results are listed.
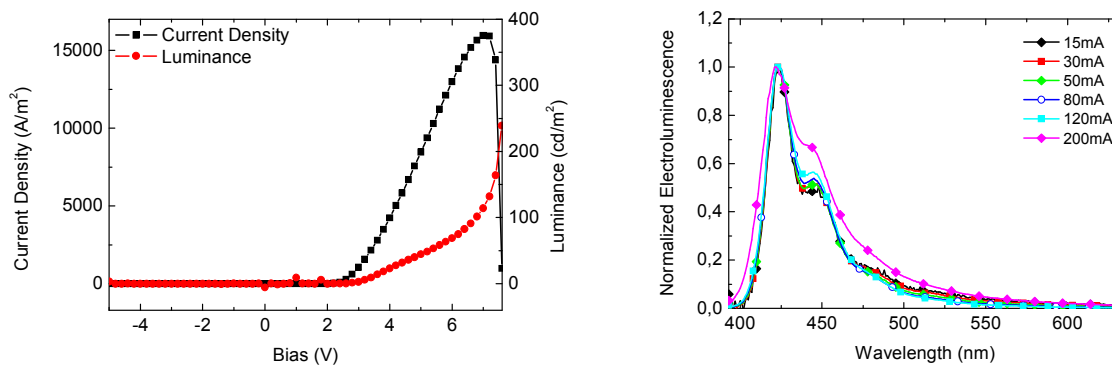


Figure 5.41: Current-voltage-luminance characteristic (left) and EL spectra (I-sweep; right) of the ITO/PEDOT:PSS/PEGPF/Ca/Al device.

Table 5.12: Key results of the ITO/PEDOT:PSS/PEGPF/Ca/Al device.

| Onset voltage | Maximum efficiency | Maximum luminance | Peak maximum | CIE 1931 coordinates | CIE 1931 diagram |
|---|---|---|---|---|---|
| ~2,6 V | 0,006 cd/A (≤ 6,5 V)  ~0,3 cd/A (> 6,5 V flash) | ~80 cd/m$^2$ (≤ 6,5 V)  238,7 cd/m$^2$ (> 6,5 V flash) | 425 nm | x = 0,167 y = 0,075 (@ 30 mA) |  |

*PEGPF single layer device with TPBi layer (ITO/PEDOT:PSS/PEGPF/TPBi/Ca/Al)*

Due to the additional TPBi layer, the PEGPF single layer device shows an enhancement of the efficiency from 0,006 to 0,040 cd/A and a maximal luminance value of 374,4 cd/m$^2$. The obtained EL emission is blue (CIE 1931 x = 0,179 and y = 0,085) with a maximum at 423 nm. The OLED shows a measurable emission already at a device current of 1 mA, but an increase of the current (1 $\rightarrow$ 10 mA) leads to an immediately recognizable change of the emission spectrum. In Figure 5.42, the IV characteristic and the EL spectra at different device currents of the PEGPF single layer device with an additional TPBi layer are depicted. The key results are listed in Table 5.13.
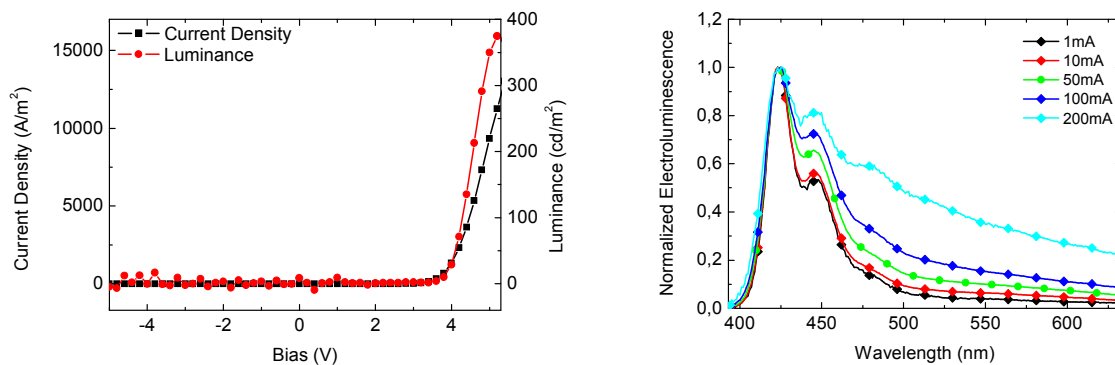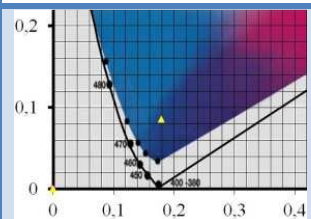


Figure 5.42: Current-voltage-luminance characteristic (left) and EL spectra (I-sweep; right) of the ITO/PEDOT:PSS/PEGPF/TPBi/Ca/Al device.

Table 5.13: Key results of the ITO/PEDOT:PSS/PEGPF/TPBi/Ca/Al device.

| Onset voltage | Maximum efficiency | Maximum luminance | Peak maximum | CIE 1931 coordinates | CIE 1931 diagram |
|---|---|---|---|---|---|
| ~3,4 V | 0,040 cd/A | 374,4 cd/m$^2$ | 423 nm | x = 0,179 y = 0,085 (@ 10 mA) |  |

## 5.2.5 Multi layer OLED with PEGylated polyfluorene and PIF

This chapter deals with the analysis of multi layer OLEDs with two blue emitting layers – one made of the PEGPF and the other one made of PIF. The target was to achieve an accumulation of charge carriers at the interface between the PIF and PEGPF layer and therefore to enhanced the device efficiency due to a facilitated formation of excitons.

As shown in the chapter 5.1 before, the optical path and the performance of PEGPF and PIF single layer OLEDs had to be determined, before starting the assembly of the multi layer systems.

**Optical path**

The absorption spectrum of PIF in film [31] shows a maximum at 405 nm, the PL spectrum reveals a peak maximum at 424 nm and vibronic fine structures at 450 nm and 479 nm. Due to the small overlap of the PL spectrum of PEGPF (PEGPF film emission peak at 425 nm) and the absorption spectrum of PIF, only a small absorption of emitted light from the PEGPF film with a wavelength between 400 to 415 nm is expected, but for the majority of the emitted light (wavelength > 415 nm), an absorption can excluded. In Figure 5.43 on the right side, the PL spectra of PEGPF and PIF [31] and the absorption spectrum of PIF [31] are depicted. The left side of Figure 5.43 shows a sketch of the optical path of light emitted from the PEGPF layer.
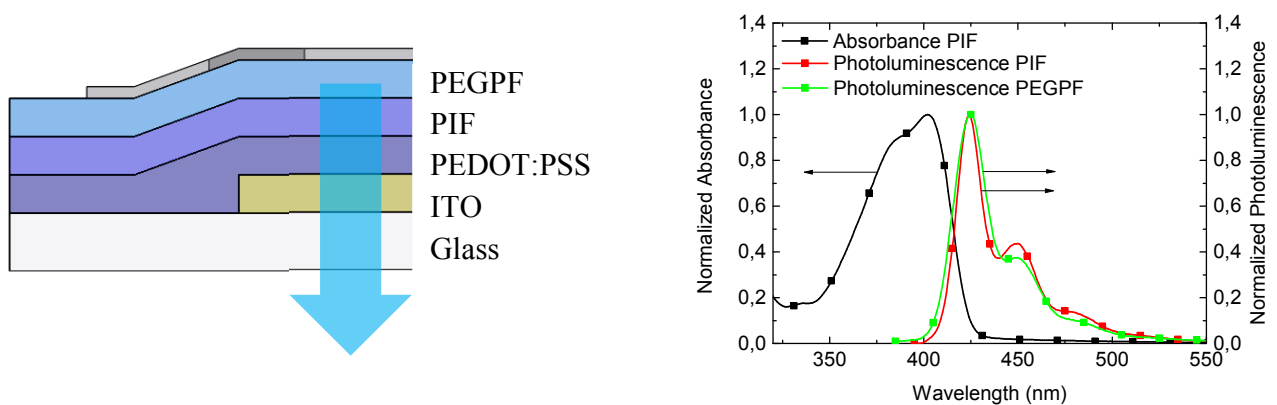


Figure 5.43: Left: sketch of the optical path of light emitted from the PEGPF layer; right: PL spectra of PEGPF and PIF in film [31] and absorption spectrum of PIF in film [31].

**Performance of single layer devices**

In chapter 5.2.4, the performances of PEGPF single layer devices were already discussed. In the following, the results of single layer devices with PIF as light emitting layer and the device configurations ITO/PEDOT:PSS/PIF/Ca/Al and ITO/PEDOT:PSS/PIF/TPBi/Ca/Al are presented. The PIF layer was deposited from a toluene solution with a concentration of 5 g/l, leading to a layer thickness of about 75 nm.

*PIF single layer device (ITO/PEDOT:PSS/PIF/Ca/Al)*

The device shows an efficiency of 0,628 cd/A and a luminance of 4.489 cd/m$^2$. Blue emission is found (CIE 1931 x = 0,153 and y = 0,055) with peaks at 427 nm and 449 nm and a shoulder at around 477 nm. Performing a current sweep, the emission spectrum stays almost the same for current values from 1 to 50 mA. Only after applying a device current $\geq$ 100 mA, a distinct change of the emission spectrum is examined, leading to a greenish-blue emission.

When comparing the PL and EL spectrum of PIF, a significant difference of the ratio between the intensities of the three emission peaks is observed. Due to previous investigations [86] [87] of OLEDs using PIF as light emitting layer, it is known, that the thickness of the PIF film and the used cathode material has a strong influence to the ratio between the intensities of the emission peaks and can explain the difference between the PL and EL spectrum. Figure 5.44 on the left side depicts the IV characteristic and on the right side, the emission spectra at different operation currents are shown. The key results are listed in Table 5.14 .
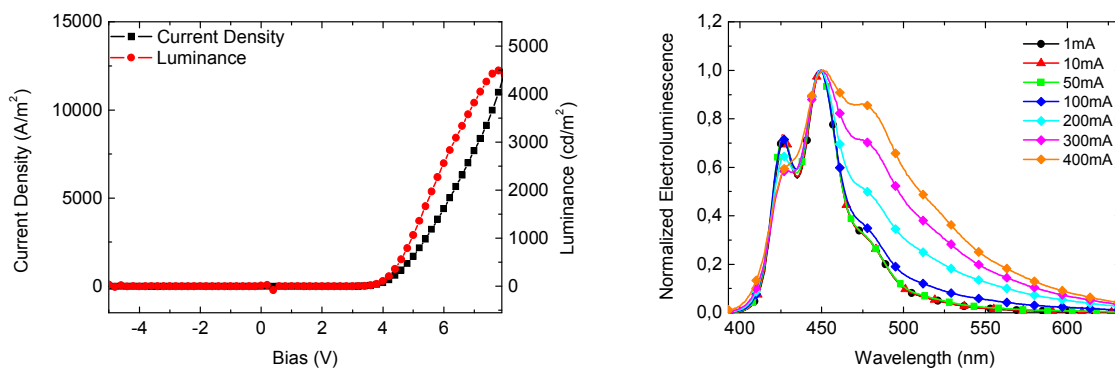


Figure 5.44: Current-voltage-luminance characteristic (left) and EL spectra (I-sweep; right) of ITO/PEDOT:PSS/PIF/Ca/Al device.

Table 5.14: Key results of ITO/PEDOT:PSS/PIF/Ca/Al device.

| Onset voltage | Maximum efficiency | Maximum luminance | Peak maximum | CIE 1931 coordinates | CIE 1931 diagram |
|---|---|---|---|---|---|
| ~3,2 V | 0,628 cd/A | 4.489 cd/m$^2$ | 449 nm | x = 0,153 y = 0,055 (@ 10 mA) |  |

*PIF single layer device with TPBi layer (ITO/PEDOT:PSS/PIF/TPBi/Ca/Al)*

The second investigated single layer device – using PIF as light emitting layer – has the device configuration ITO/PEDOT:PSS/PIF/TPBi/Ca/Al. The achieved device efficiency is 0,569 cd/A and a luminance value of 2.986 cd/m$^2$ is determined. The device shows blue emission (CIE 1931 x = 0,152 and y = 0,067) with emission peaks at 426 nm and 450 nm and a shoulder at around 479 nm. Already at a device current of 0,1 mA, an emission spectrum is measurable. Similar to the PIF single layer device without a TPBi layer, the emission spectrum of the device with the TPBi layer stays almost the same for a wide value range of the device current (0,1 to 50 mA). Only after applying a device current ≥ 100 mA, a distinct change of the emission spectrum is examined, leading to a greenish-blue emission. Figure 5.45 on the left side, depicts the IV characteristic and on the right side, the emission spectra at different operation currents. Table 5.15 shows a summary of the measurement results.
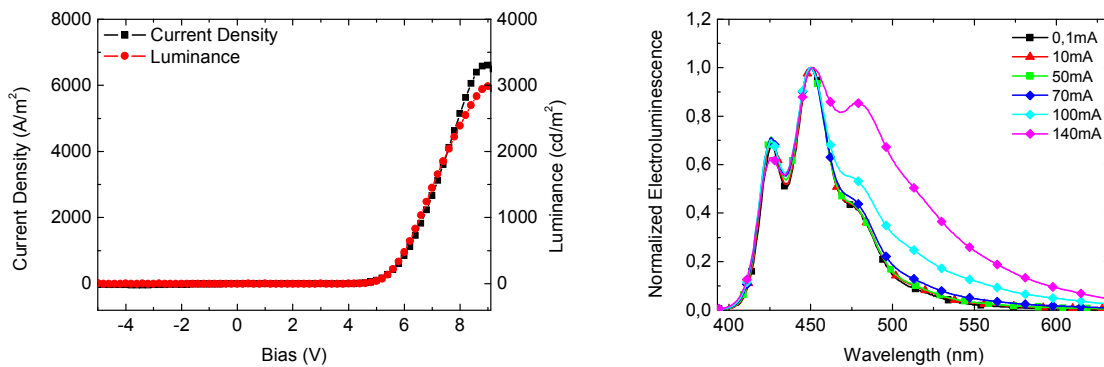


Figure 5.45: Current-voltage-luminance characteristic (left) and EL spectra (I-sweep; right) of ITO/PEDOT:PSS/PIF/TPBi/Ca/Al device.

Table 5.15: Key results of ITO/PEDOT:PSS/PIF/TPBi/Ca/Al device.

| Onset voltage | Maximum efficiency | Maximum luminance | Peak maximum | CIE 1931 coordinates | CIE 1931 diagram |
|---|---|---|---|---|---|
| ~3,8 V | 0,569 cd/A | 2.986 cd/m$^2$ | 450 nm | x = 0,152 y = 0,067 (@ 10 mA) |  |

**Assembly of multi layer devices**

Two different layer assemblies were fabricated: ITO/PEDOT:PSS/PIF/PEGPF/Ca/Al and ITO/PEDOT:PSS/PIF/PEGPF/TPBi/Ca/Al. The PIF layer (~75 nm) was deposited from a 5 g/l toluene solution, for the fabrication of the PEGPF layer (~65 nm), a 5 g/l MeOH solution was used. The whole device structure, including the thicknesses of the individual layers, is depicted in Figure 5.45.



Aluminum, 100 nm
Calcium, 10 nm
(TPBi, 10 nm)
PEGPF, ~65 nm
PIF, ~75 nm
PEDOT:PSS, ~50 nm
ITO, ~100 nm
Glass substrate, ~1 mm

Figure 5.46: Assembly and thicknesses of the individual layers of the multi layer device.

*Multi layer device (ITO/PEDOT:PSS/PIF/PEGPF/Ca/Al)*

In comparison to the PIF and PEGPF single layer devices (without a TPBi layer), which show device efficiencies of 0,628 cd/A and 0,006 cd/A, an enhancement of the efficiency to 0,824 cd/A can be achieved when using a bilayer structure of PIF and PEGPF. The multi layer device reaches a luminance value of 4.912 cd/m$^2$, which is also an enhancement compared to the luminance values of the single layer devices (PIF: 374,4 cd/m$^2$; PEGPF: 4.489 cd/m$^2$). Blue EL emission is found (CIE 1931 x = 0,158 and y = 0,067) already at a device current of 0,1 mA with emission peaks at 427 nm and 449 nm and a shoulder at 480 nm. When performing a current sweep, the emission spectrum stays almost the same for current values up to 30 mA. A further increase of the device current leads to a distinct change of the EL spectrum and a greenish-blue emission is determined. Figure 5.47 shows the corresponding current-voltage-luminance characteristics and the emission spectra at different operation currents. In Table 5.16, a summary of the measurement results is listed.
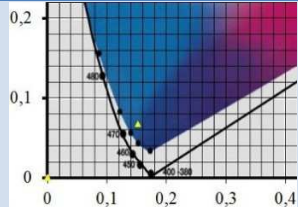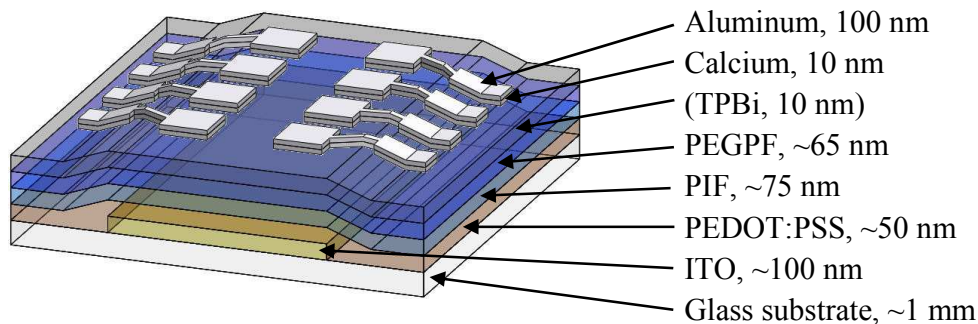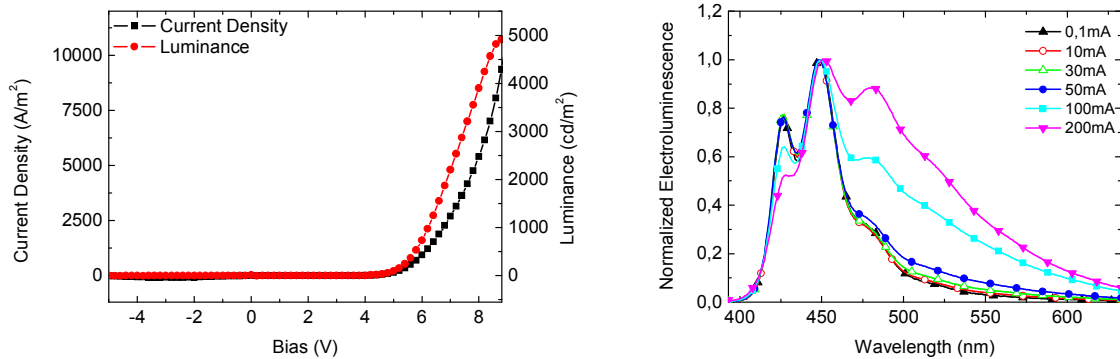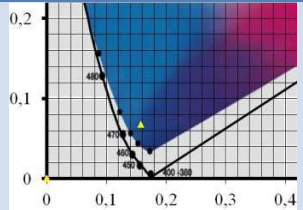
Figure 5.47: Current-voltage-luminance characteristic (left) and EL spectra (I-sweep; right) of ITO/PEDOT:PSS/PIF/PEGPF/Ca/Al device.

Table 5.16: Key results of ITO/PEDOT:PSS/PIF/PEGPF/Ca/Al device.

| Onset voltage | Maximum efficiency | Maximum luminance | Peak maximum | CIE 1931 coordinates | CIE 1931 diagram |
|---|---|---|---|---|---|
| ~3,5 V | 0,824 cd/A | 4.912 cd/ m$^2$ | 449 nm | x = 0,158 y = 0,067 (@ 10 mA) |  |

*Overview of measurements results*

Figure 5.48 shows a summary of the maximum efficiency and luminance values and the corresponding emission colors depicted by marks in a CIE 1931 diagram (operation current: 30 mA). In Figure 5.49, the emission spectra of the PIF and PEGPF single layer device and the multi layer device are depicted. The EL spectra of the PIF single layer device and the multi layer device possesses a high degree of similarity which is an indication, that the PIF layer is mainly responsible for the emission of the multi layer device. In comparison to the PIF single layer device, the multi layer device shows a small shift of the emission color into the light blue region, but an enhancement of the efficiency of about 30 % (0,628 cd/A → 0,824 cd/A) is determined.

*PIF PEGPF multi layer device*
Max. eff.: 0,824 cd/A (@ 6,6 V)
Max. lum.: 4.912 cd/m² (@ 8,8 V)
Lum. @ 6/7/8 V: 733,5/2.201,4/3.900,2 cd/m²

*PEGPF single layer device*
Max. eff.: 0,006 cd/A (@ 4,2 V)
Max. lum.: 239 cd/m² (@ 7,6 V)
Lum. @ 6/7/8 V: 68,8/114,2/- cd/m²

*PIF single layer device*
Max. eff.: 0,628 cd/A (@ 5 V)
Max. lum.: 4.489 cd/m² (@ 7,8 V)
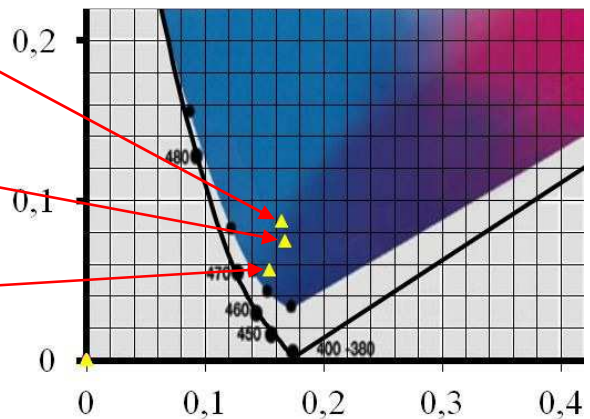Lum. @ 6/7/8 V: 2.560/3.818,8/4.410,6 cd/m²

Figure 5.48: Maximum efficiency and luminance and the corresponding applied voltage values and emission colors (CIE 1931 diagram) of the single layer systems ITO/PEDOT:PSS/ PEGPF/Ca/Al and ITO/PEDOT:PSS/PIF/Ca/Al and the multi layer system ITO/PEDOT:PSS/ PIF/PEGPF/Ca/Al at an operation current of 30 mA. Additionally the luminance values at 6, 7 and 8 V are listed.
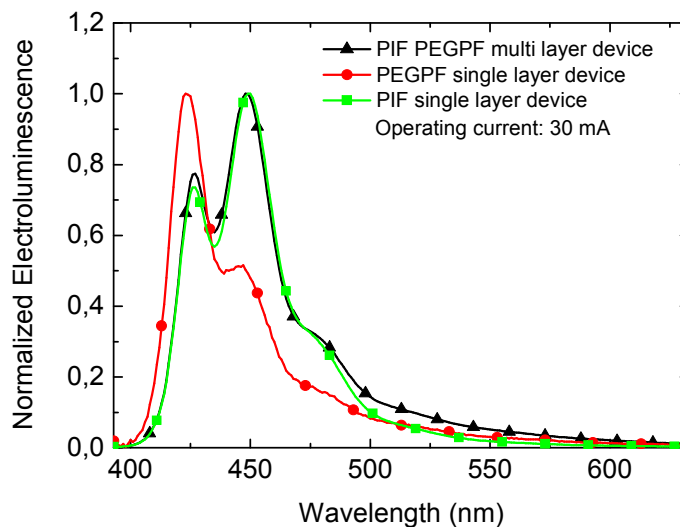
Figure 5.49: EL spectra of the single layer devices ITO/PEDOT:PSS/PEGPF/Ca/Al and ITO/PEDOT:PSS/PIF/Ca/Al and the multi layer device ITO/PEDOT:PSS/PIF/PEGPF/Ca/Al, measured at an operation current of 30 mA.

*Multi layer device with TPBi layer (ITO/PEDOT:PSS/PIF/PEGPF/TPBi/Ca/Al)*

The multi layer device shows an efficiency of 0,794 cd/A and a luminance of 3.576 cd/m², which is an enhancement compared to the PIF and PEGPF single layer devices with a TPBi layer (PIF: 0,569 cd/A, 2.986 cd/m²; PEGPF: 0,040 cd/A, 374,4 cd/m²). Blue EL emission is already

detected at a device current of 0,1 mA (CIE 1931 x = 0,155 and y = 0,085) with emission peaks at 425 and 450 nm and a shoulder at 479 nm. Increasing the device current leads to a change of the EL spectrum and a greenish-blue emission is determined. Figure 5.50 shows the corresponding current-voltage-luminance characteristics and the emission spectra at different operation currents. In Table 5.17, a summary of the measurement results is listed.
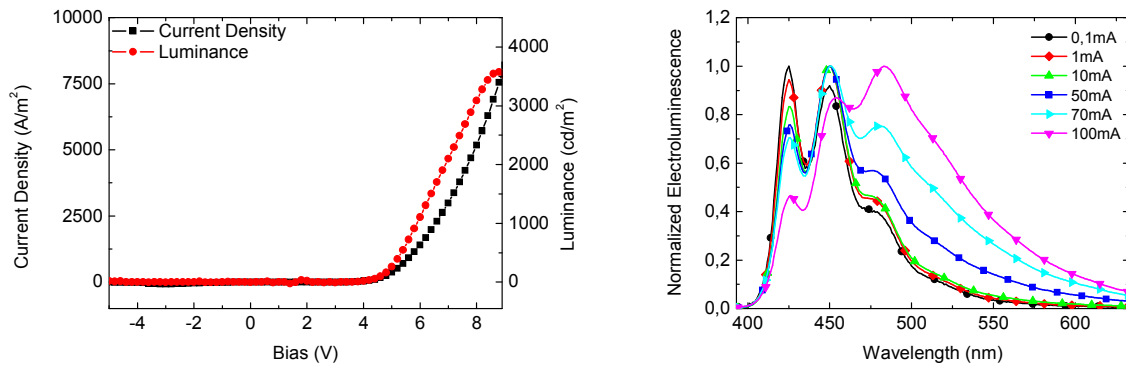


Figure 5.50: Current-voltage-luminance characteristic (left) and EL spectra (I-sweep; right) of ITO/PEDOT:PSS/PIF/PEGPF/TPBi/Ca/Al device.

Table 5.17: Key results of ITO/PEDOT:PSS/PIF/PEGPF/TPBi/Ca/Al device.

| Onset voltage | Maximum efficiency | Maximum luminance | Peak maximum | CIE 1931 coordinates | CIE 1931 diagram |
|---|---|---|---|---|---|
| ~3,6 V | 0,794 cd/A | 3.576 cd/m$^2$ | 450 nm | x = 0,155 y = 0,085 (@ 10 mA) |  |

*Overview of measurements results*

Figure 5.51 shows a summary of the maximum efficiency and luminance values and the corresponding emission colors depicted by marks in a CIE 1931 diagram (operation current: 10 mA) of the PIF and PEGPF single layer devices and the multi layer device. For purposes of comparison, the emission color of the multi layer device without a TPBi layer (at a device current of 10 mA) is also depicted by a mark in the diagram (red triangle). In Figure 5.52, the emission spectra of the devices are depicted. In analogy to the paragraph above, the EL spectra of the PIF single layer device and the multi layer device possess a high degree of similarity and are an indication, that the PIF layer is mainly responsible for the emission of the multi layer device. In comparison to the PIF single layer device, the multi layer device shows a small shift of the emission color into the light blue region, but an enhancement of the efficiency of about 40 %

(0,569 cd/A $\rightarrow$ 0,794 cd/A) is determined. If one makes a comparison between the assembled multi layer devices (with and without a TPBi layer), it is obvious, that the multi layer device with the layer configuration ITO/PEDOT:PSS/PIF/PEGPF/Ca/Al shows the best performance due to a higher device efficiency and luminance (without TPBi: 0,824 cd/A, 4.912 cd/m$^2$; with TPBi: 0,794 cd/A, 3.576 cd/m$^2$) and an emission color, which is more in the deep blue region (CIE 1931 @ 10 mA: without TPBi: x = 0,158 and y = 0,067; with TPBi: x = 0,155 and y = 0,085).

*PEGPF single layer system*
Max. eff.: 0,040 cd/A (@ 4,6 V)
Max. lum.: 374,4 cd/ m$^2$ (@ 5,2 V)
Lum. @ 5/6/7 V: 350/-/- cd/m$^2$

*PIF PEGPF multi layer system*
Max. eff.: 0,794 cd/A  (@5,8 V)
Max. lum.: 3576 cd/ m$^2$ (@8,8 V)
Lum. @ 5/6/7 V: 260,6/1105,5/2099 cd/m$^2$

*PIF single layer system*
Max. eff.: 0,569 cd/A (@ 6,4 V)
Max. lum.: 2986cd/ m$^2$ (@ 9 V)
Lum. @ 5/6/7 V: 96,2/851,9/2661 cd/m$^2$

*PIF PEGPF multi layer system (without TPBi layer)*
Max. eff.: 0,824 cd/A (@6,6 V)
Max. lum.: 4912 cd/m$^2$ (@ 8,8 V)
Lum. @ 5/6/7 V: 95,4/733,5/2201,4 cd/m$^2$
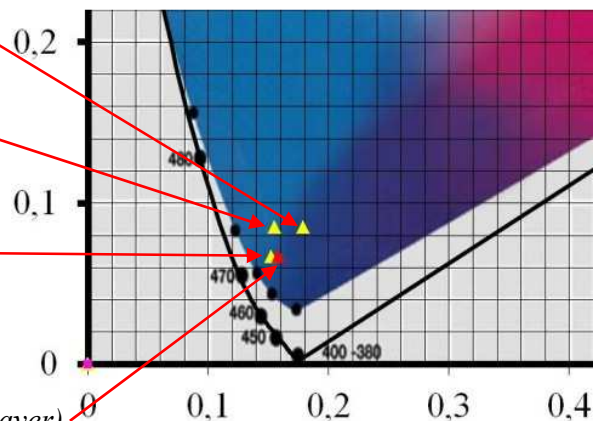
Figure 5.51: Maximum efficiency and luminance values and the corresponding applied voltage values and emission colors (CIE 1931 diagram) of the single layer systems ITO/PEDOT:PSS/PEGPF/TPBi/Ca/Al and ITO/PEDOT:PSS/PIF/TPBi/Ca/Al and the multi layer system ITO/PEDOT:PSS/PIF/PEGPF/TPBi/Ca/Al at an operation current of 10 mA. Additionally the data of the multi layer system ITO/PEDOT:PSS/PIF/PEGPF/Ca/Al from the paragraph above (see Figure 5.48) is depicted (CIE 1931 coordinates measured at 10 mA) and the luminance values at 5, 6 and 7 V are listed.

Figure 5.52: EL spectra of the single layer devices ITO/PEDOT:PSS/PEGPF/TPBi/Ca/Al and ITO/PEDOT:PSS/PIF/TPBi/Ca/Al and the multi layer device ITO/PEDOT:PSS/PIF/PEGPF/TPBi/Ca/Al. For purposes of comparison, the EL spectrum of the multi layer device without a TPBi layer (ITO/PEDOT:PSS/PIF/PEGPF/Ca/Al) is depicted too (operation current: 10 mA).
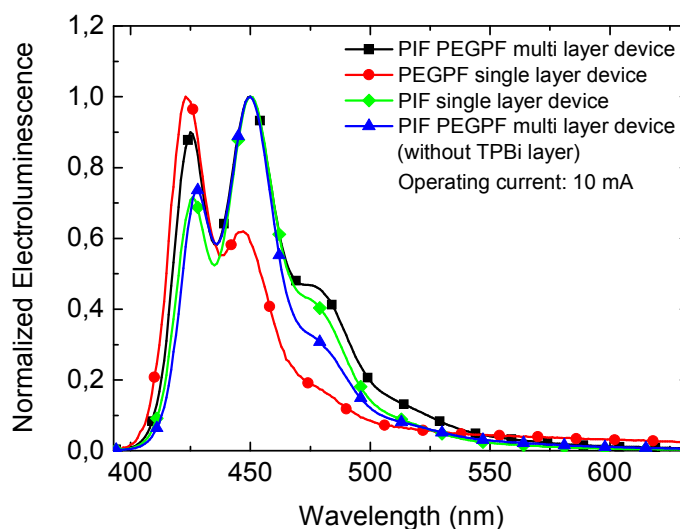
## 5.2.6  AFM investigation of multi layer OLED surface

The investigations concerning the surface energies of the PIF film and the solvent MeOH revealed (as shown in chapter 5.2.1), that the surface energy of MeOH (22,70 mN/m) is smaller than the surface energy of the PIF film (24,94 mN/m), but shows only a small difference of 2,24 mN/m. Due to the similar surface energies, the question arises, if the PEGPF film covers the PIF film homogeneously during spin coating. For maximum accuracy, the surface (without top electrode) of the multi layer device (ITO/PEDOT:PSS/PIF/PEGPF/TPBi/Ca/Al) was investigated with an AFM. The 3D AFM height image (see Figure 5.53) shows an incomplete film with droplet-like features with additional heights of 40 to 150 nm. This measurement result displays in all probability an incompletely formation of the PEGPF film.

However, the multi layer device shows an enhanced performance compared to the single layer devices, but it is up to further investigations and experiments to solve the problem of covering the PIF surface with PEGPF homogeneously, which might further improve the performance of the multi layer device.
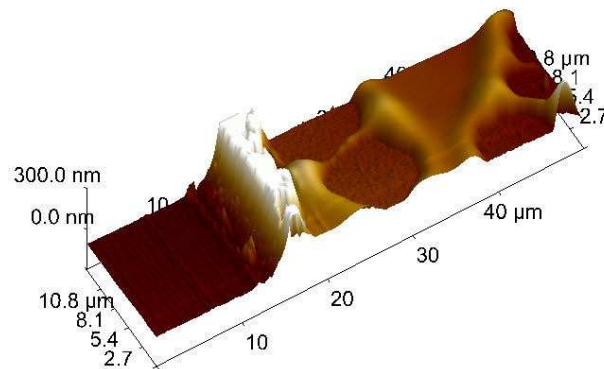
Figure 5.53: 3D AFM height image of the multi layer device surface (ITO/PEDOT:PSS/PIF/ PEGPF/TPBi; shown in chapter 5.2.5), where an incomplete film formation is found.

## 5.2.7 Summary and discussion

The novel polymer PEGylated polyfluorene (PEGPF) was investigated concerning its PL and absorption spectrum in solution and in film and the quantum yield in solution. The PL spectrum shows peaks at 423 nm (solution) and 425 nm (film), respectively. The peak maximum of the absorption spectrum is found at a wavelength of 402 nm (solution) and 400 nm (film), respectively. The calculated quantum yield is 106 %, where an error of about 10 % has to be considered.

PEGPF single layer OLEDs with the device configurations ITO/PEDOT:PSS/PEGPF/Ca/Al and ITO/PEDOT:PSS/PEGPF/TPBi/Ca/Al were fabricated. The devices show low efficiencies (without TPBi: 0,006 cd/A ; with TPBi: 0,040 cd/A) and moderate luminance values (without TPBi: ~80 cd/m$^2$; with TPBi: 374,4 cd/m$^2$).

For the assembly of multi layer devices, PEGPF was combined with a blue emitting poly(indenofluoren)-based emitter polymer (PIF). The intention was to achieve a charge carrier accumulation at the interface of the PEGPF and PIF layer to facilitate the formation of excitons and therefore to enhance the device efficiency. Two different multi layer configurations were assembled: ITO/PEDOT:PSS/PIF/PEGPF/Ca/Al and ITO/PEDOT:PSS/PIF/PEGPF/TPBi/Ca/Al. Both devices show an enhancement of the efficiency and luminance compared to the corresponding PIF and PEGPF single layer OLEDs. The device with the layer configuration ITO/PEDOT:PSS/PIF/PEGPF/Ca/Al exhibits the best performance, where an efficiency of 0,824 cd/A and a luminance of 4.912 cd/m$^2$ is determined. The similarity of the EL spectra of the PIF single layer devices and the multi layer OLEDs is an indication, that the PIF layer is mainly responsible for the emission of the multi layer devices. A 3D AFM height image of the surface of a multi layer device reveals in all probability an incomplete film formation of the PEGPF layer. Considering the good results concerning the device efficiency even with a non-homogeneous PEGPF film, it clearly indicates an immense potential of the multi layer devices.

# 6 ITO free flexible OLEDs

Today's display market is mainly represented by liquid crystal device (LCD) and plasma monitors. Both technologies require a rigid transparent substrate, for example, a glass plate. For contacting, the substrate has to be coated with a conductive material, which has to be transparent for visible light. The material most commonly used for this application is ITO. With a present sources of only 0,2 ppm [88] in the earth's crust, indium is very limited. Predicted statements reckon that in about three decades the resource will be exhausted, therefore scientists are looking for alternatives. [89]

The following chapters will report on experiments with OLEDs completely free of ITO. Instead of ITO, the combination of a high conductive PEDOT:PSS film and a thin gold layer was used as the transparent bottom electrode. Additionally, flexible instead of rigid substrates were taken to enable the manufacturing of flexible OLEDs.

**High conductive PEDOT:PSS combined with gold layer**

The used highly conductive PEDOT:PSS (HC-PEDOT:PSS) solution consisted of CLEVIOS™ PH 1000, 15 %vol isopropanol and 5 %vol dimethyl sulfoxid. To increase the conductivity of the bottom electrode, an additional gold layer was inserted between the substrate and the HC-PEDOT:PSS layer. The thicker the gold layer, the higher the conductivity, but also the lower the transparency. To find a good balance between conductivity and transparency, a series of substrates (see Figure 6.1) with different gold layer thicknesses and a HC-PEDOT:PSS layer on top were fabricated and investigated. The gold layer was evaporated by using a high vacuum vapor deposition unit ($p \leq 10^{-6}$ mbar). HC-PEDOT:PSS was applied via spin coating and afterwards heated at 120°C for 20 min in a vacuum ($p \leq 5 \cdot 10^{-3}$ mbar), resulting in a layer thickness of about 80 nm. The substrates used for this experiment were glass plates. To determine the surface resistivity, a Four-Point-Probe was used. Following this method, four measuring tip (probes) are placed equally spaced in line on the surface. A current source is used to supply current through the outer two probes, a voltmeter measures the potential difference between the inner two probes. With these data (current $I$ and potential difference $U$) it is possible to calculate the surface resistivity $\rho_s$ with the equation

$$\rho_S = \frac{\pi}{\ln(2)} \frac{U}{I} \qquad (in\ \Omega_\square).  \tag{30}$$

Table 6.1 depicts the measured sheet resistances of the different gold films with a HC-PEDOT:PSS-layer on top. Additionally, the transparency at 500 nm is named and in Figure 6.2 the transmission spectra of the individual samples are shown. For purposes of comparison, the sheet resistance of a ITO coated glass substrate (as it was used for the experiments shown in chapter 5) was investigated too and a value of 3,19 $\Omega_\square$ was determined.

HC-PEDOT:PSS, ~80 nm
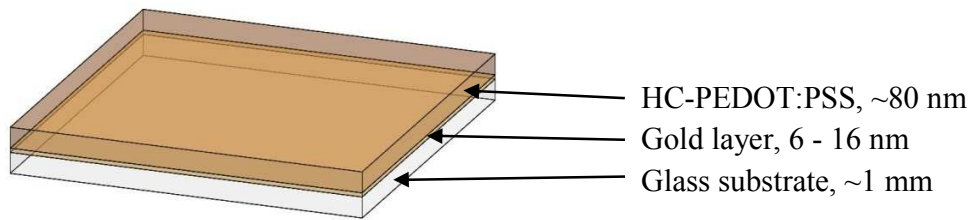Gold layer, 6 - 16 nm
Glass substrate, ~1 mm

Figure 6.1: Layer configuration of samples for sheet resistance and transparency measurements.

Table 6.1: Sheet resistance and transparency (at 500 nm) of Glass/Au/HC-PEDOT:PSS samples with different gold layer thicknesses.

| Gold layer thickness (in nm) | Sheet resistance (in $\Omega_{\square}$) | Transparency at 500 nm (in %) |
|---|---|---|
| 6 | 45,46 | 62,3 |
| 8 | 20,25 | 59,7 |
| 10 | 5,65 | 57,6 |
| 12 | 2,88 | 55,3 |
| 16 | 1,17 | 50,6 |
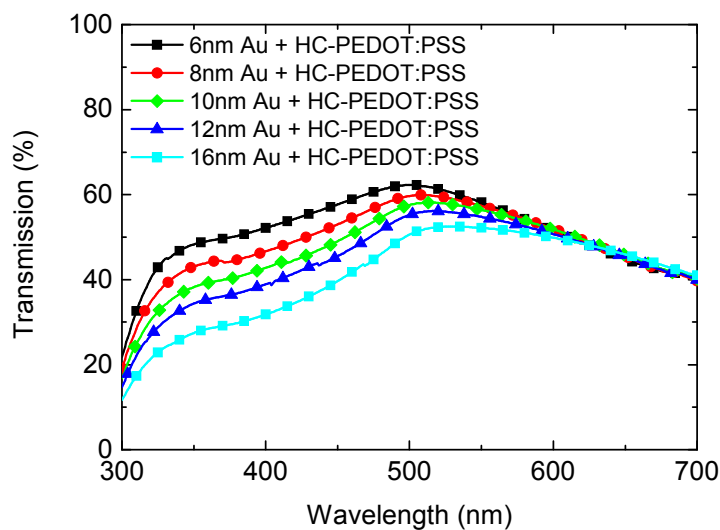


Figure 6.2: Transmission spectra of Glass/Au/HC-PEDOT:PSS samples with different gold layer thicknesses.

The combination of a 8 nm thick gold layer with a HC-PEDOT:PSS layer shows a good tradeoff between sheet resistance and transparency and was used for assembling the flexible OLEDs. To be able to assess the efficiency of the OLED and the influence of different bottom electrodes, two further flexible OLEDs were fabricated. For one device, only a HC-PEDOT:PSS layer was used as bottom electrode, for the other device, a polyester film laminated with ITO was used. The polymer PIF (already discussed in chapter 5.2.5) was chosen for the fabrication of the light

emitting layer and the combination of a 10 nm thick calcium layer covered by a 100 nm thick aluminum layer was applied as the top electrode for all flexible OLEDs.

Moreover, the behavior of the device was investigated when flipping the layer sequence of the gold and HC-PEDOT:PSS layer, so that first the HC-PEDOT:PSS layer was spin coated and afterwards the gold layer was evaporated. Building an OLED with this configuration leads to short circuits of almost all pads of the device. A reason for this can be the diffusion of gold into the light emitting layer during the deposition process, finally leading to a short circuit. To avoid this, the gold layer was evaporated first, followed by coating with HC-PEDOT:PSS.

## 6.1 Flexible OLED with ITO bottom electrode

Prior to the investigation of flexible OLEDs with a gold and HC-PEDOT:PSS layer as bottom electrode, OLEDs with a ITO coated polyester film as substrate were assembled in order to ensure comparability concerning the performance of the OLEDs. The preparation steps of the ITO coated polyester film were already explained in chapter 4.1. After depositing the PEDOT:PSS layer, spin coating of a 5 g/l PIF solution (dissolved in toluene) followed. The last step was to evaporate the top electrode.

Due to the fact that the layer thickness is determined by measuring the depth of a scratch, made with a sharp hard object on the surface of the device, it is not possible to gauge the layer thicknesses of the flexible OLED, because a scratching of the polyester film cannot be excluded.

During the operation of the flexible OLED, a strong enhancement of the luminance when changing the applied voltage by a small amount is observed, followed by a breakdown and destruction of the OLED when increasing the voltage further. From the point in which luminance starts, to the point in which the OLED is damaged, the voltage range is only 2 V. For the calibration of luminance, one should apply a voltage value which is in the middle between the onset voltage and the voltage value where the luminance reaches its maximum. When operating the device in the middle of this voltage range, a very fast degradation and intensity decrease is witnessed. To enable the possibility of calibration, the device has to be operated with an applied voltage slightly larger than the onset voltage, to prevent destruction during calibration. This leads to another difficulty: Due to the fact that the luminance at this voltage value is very small, slight measuring errors during calibration causes major problems of distortion to the measured luminance value. The used voltage for calibration was 4,4 V. For comparison, the onset voltage reaches a value of 3,8 V. Looking at the IV-characteristics (shown on the left side of Figure 6.3), it can be see that at 4,4 V, the luminance value reaches only 2,4% of its maximum. Due to this, the error of the calculated luminance value and resulting from this, the error of the calculated device efficiency is so high that these values have no explanatory power anymore. As a consequence for further investigations, the device current density is used as an appropriate comparator instead of the device efficiency and luminance.

If one considers the course of the current density curve, an enhancement immediately after applying a positive voltage to the device can be seen, which reached about 1.000 A/m$^2$ and stays the same until about 4 V. In this voltage range, no emission of light is detectable. When light

emission starts, the current density increases again and a value of 12.000 A/m$^2$ at maximum luminance is measured. Concerning the emission spectrum, the flexible OLED shows similar measurement results compared to the device ITO/PEDOT:PSS/PIF/Ca/Al (shown in chapter 5.2.5), where ITO coated glass was used as substrate and bottom electrode. Blue emission is found (CIE 1931 x = 0,157 and y = 0,076) and the emission peaks of the EL spectrum are positioned at 426 nm and 448 nm and a shoulder at about479 nm is determined. Figure 6.3 shows the current-voltage-luminance characteristics and the emission spectra at different operation currents. In Table 6.2, a summary of the measurement results is listed.
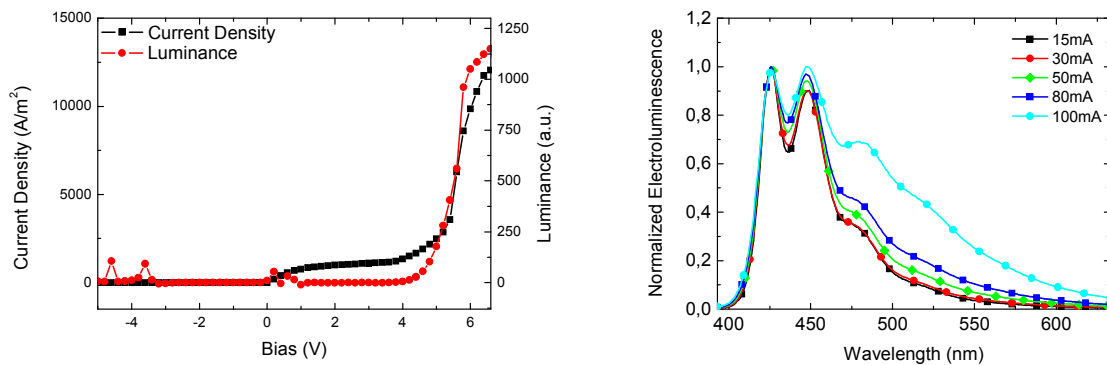


Figure 6.3: Current-voltage-luminance characteristic (left) and EL spectra (I-sweep; right) of flexible OLED with the layer configuration polyester film/ITO/PEDOT:PSS/PIF/Ca/Al.

Table 6.2: Key results of flexible OLED with the layer configuration polyester film/ITO/ PEDOT:PSS/PIF/Ca/Al.

| Onset voltage | Maximum efficiency | Maximum luminance | Peak maximum | CIE 1931 coordinates | CIE 1931 diagram |
|---|---|---|---|---|---|
| ~3,8 V | not measurable | not measurable | 426 nm | x = 0,157 y = 0,076 (@ 15 mA) |  |

## 6.2 Flexible OLED with HC-PEDOT:PSS bottom electrode

As next attempt, the behavior of a flexible OLED with the same structure as shown in chapter 6.1, but with a HC-PEDOT:PSS layer instead of a ITO layer, was investigated. As flexible substrate, again a polyester film was used. For bottom electrode structuring, two stripes of scotch tape were fixed on the edges of the foil. After coating the HC-PEDOT:PSS layer, the tape stripes were removed. The remaining assembling steps were the same as explained in chapter 6.1.

Operation of the OLED shows an unusual, almost linear, increase of the device current density depending on the applied voltage. Only when the voltage reaches a value higher than 18 V, luminance is detectable. A calibration to calculate the luminance value is not possible, because the light emission starts inhomogeneously over the whole device. In Figure 6.4, three pictures of the light emitting OLED at different applied voltages are depicted. On the left side of Figure 6.4, the start of the emission at edges of the OLED can be seen. Increasing the voltage leads to an expansion of the luminous area (middle of Figure 6.4). The area, in which the first light emission has been visible, stopped illuminating before the whole area is alight (right side of Figure 6.4). When considering the device current density (left side of Figure 6.5), it is obvious that the OLED loses its blocking property when operating in the reverse direction. This can be explained by the fact that, as mentioned above, partial areas show destruction before the whole area is lit. This damage can be the reason for current flow when operating in reverse direction. At maximal luminance, the device current density reaches a value of 8.000 A/m$^2$. To obtain this value, a voltage of about 30 V has to be applied. Comparing these results with the measurement results of the flexible OLEDs using ITO as the bottom electrode, it is obvious that a HC-PEDOT:PSS layer does not achieve the necessary conductivity for satisfying device operation. Blue emission is found (CIE 1931 x = 0,157 and y = 0,075) with emission peaks at 426 nm and 448 nm and a shoulder at about 480 nm. Figure 6.5 shows the current-voltage-luminance characteristics and the emission spectra at different operation currents. The key results of the measurements are listed in Table 6.3.



Figure 6.4: Illumination of polyester film/HC-PEDOT:PSS/PIF/Ca/Al device; left: starting of luminance at the edges of the OLED; middle: expansion of illuminating area; right: further expansion of illumination, while light emission stops in the area that was illuminated first.
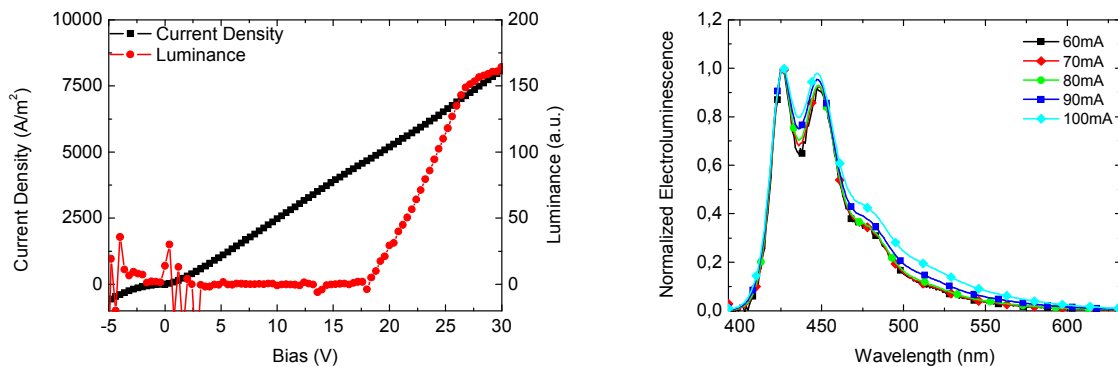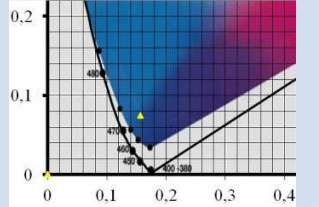


Figure 6.5: Current-voltage-luminance characteristic (left) and EL spectra (I-sweep; right) of flexible OLED, with the layer configuration polyester film/HC-PEDOT:PSS/PIF/Ca/Al.

Table 6.3: Key results of flexible OLED with the layer configuration polyester film /HC-PEDOT:PSS/PIF/Ca/Al.

| Onset voltage | Maximum efficiency | Maximum luminance | Peak maximum | CIE 1931 coordinates | CIE 1931 diagram |
|---|---|---|---|---|---|
| ~18 V | not measurable | not measurable | 426 nm | x = 0,157 y = 0,075 (@ 60 mA) | |

## 6.3 Flexible OLED with gold and HC-PEDOT:PSS bottom electrode

As the final attempt, the actually intended layer structure, where a 8 nm thick gold layer coated with HC-PEDOT:PSS is used as bottom electrode, was manufactured. This final layer structure is depicted in Figure 6.6.

Aluminum, 100 nm
Calcium, 10 nm
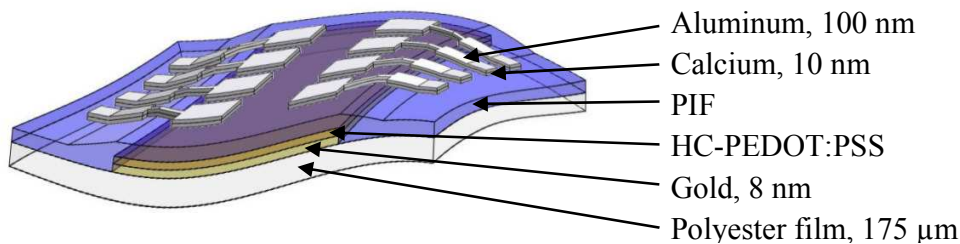PIF
HC-PEDOT:PSS
Gold, 8 nm
Polyester film, 175 µm

Figure 6.6: Assembly and thicknesses (if available) of individual layers of a flexible OLED.

In contrast to the flexible OLEDs shown in chapter 6.1 and 6.2, it was possible to perform a luminance calibration with the device presented in this paragraph.

The device shows an efficiency of 0,036 cd/A and a luminance of 419,0 cd/m$^2$. The device current reached a maximum of 11.800 A/m$^2$ which is an indication that the bottom electrode has a sufficient conductivity. The EL spectrum (CIE 1931 x = 0,156 and y = 0,088) reveals peaks at 426 nm and 448 nm and a shoulder at about 479 nm. Figure 6.7 shows the current-voltage-luminance characteristics and the emission spectra at different operation currents. The key results of the measurement are listed in Table 6.4.
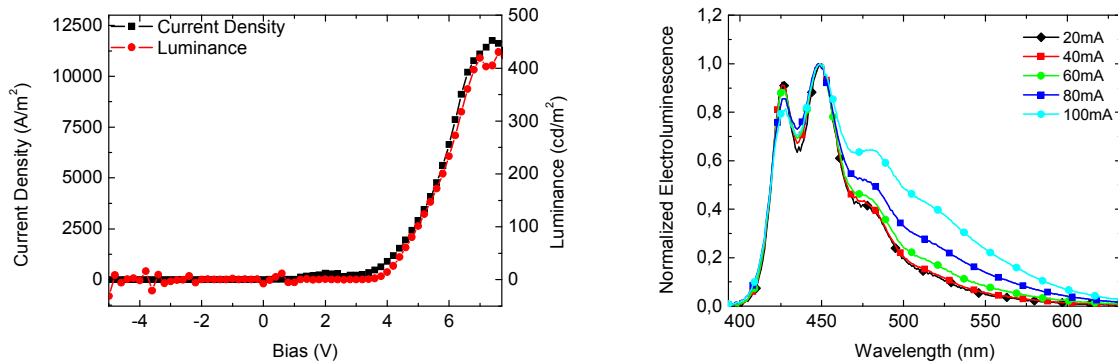
Figure 6.7: Current-voltage-luminance characteristic (left) and EL spectra (I-sweep; right) of flexible OLED with the layer configuration polyester film /Au/HC-PEDOT:PSS/PIF/Ca/Al.

Table 6.4: Key results of flexible OLED with the layer configuration polyester film/Au/HC-PEDOT/PIF/Ca/Al.

| Onset voltage | Maximum efficiency | Maximum luminance | Peak maximum | CIE 1931 coordinates | CIE 1931 diagram |
|---|---|---|---|---|---|
| ~3,3 V | 0,036 cd/A | 419,0 cd/ m$^2$ | 448 nm | x = 0,156 y = 0,088 (@ 20 mA) |  |

Furthermore, the operational stability during bending under ambient conditions was investigated. In Figure 6.8, a series of pictures depict the flexible OLED being bent further and further. Even to the point of bending the flexible OLED with a bending radius of about 5 mm (see Figure 6.9), the device shows blue emission without any interruptions of operation.
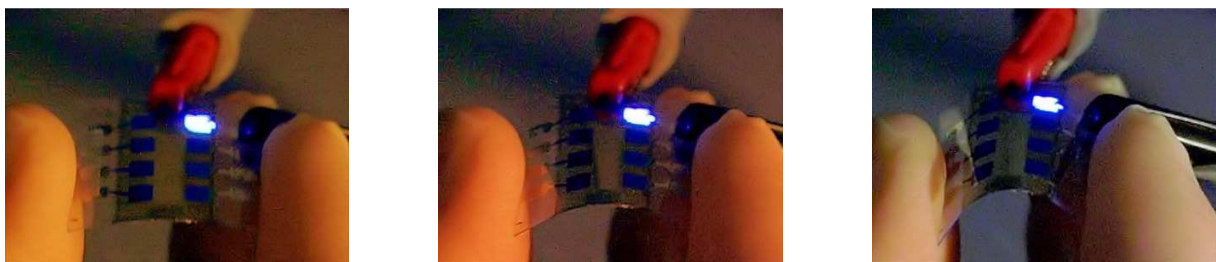


Figure 6.8: Bending of flexible OLED during operation under ambient conditions.
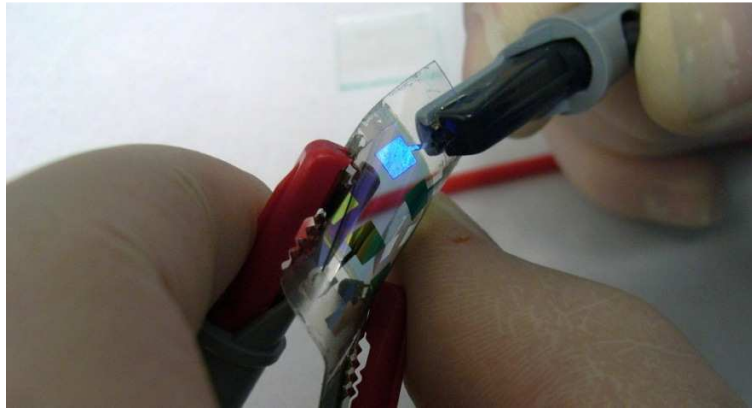
Figure 6.9: Even bending to the point of a 5 mm bending radius, the operation of the flexible OLED is not disrupted.

## 6.4  Summary and discussion

Three flexible OLEDs with different bottom electrodes were investigated, where the bottom electrode configurations are ITO, HC-PEDOT:PSS and gold coated with HC-PEDOT:PSS. Due to the limitations of the calibration procedures caused by the low stability during operation of two of the three fabricated flexible OLEDs, the device current density is used for purposes of comparison. In Table 6.5, the current densities at maximum luminance and the according applied voltage values are listed.

Table 6.5: Device current density at maximum luminance and the corresponding applied voltage values of the investigated flexible OLEDs.

| Layer configuration | Current density at maximum luminance | Corresponding applied voltage |
|---|---|---|
| polyester film/ITO/PEDOT:PSS/PIF/Ca/Al | 12.000 A/m$^2$ | 6,6 V |
| polyester film/HC-PEDOT:PSS/PIF/Ca/Al | 8.000 A/m$^2$ | 30 V |
| polyester film /Au/HC-PEDOT:PSS/PIF/Ca/Al | 11.800 A/m$^2$ | 7,7 V |

It is obvious that the combination of a gold layer coated with a HC-PEDOT:PSS film shows promising results and may be considered as an alternative to the expensive ITO. Particularly noteworthy is the fact, that not only the current density of the OLED with the gold and HC-PEDOT:PSS bottom electrode shows almost the same value as the OLED with the ITO electrode, but also during device operation, the emission is more stable compared to the other fabricated flexible OLEDs which show a fast degradation and an inhomogeneously illuminating surface, respectively. Investigations with HC-PEDOT:PSS without a gold layer reveals that the additional gold layer is of the utmost importance for satisfactory device operation.

Concerning mechanical stress, the flexible OLED with the gold and HC-PEDOT:PSS bottom electrode impresses with a stable operation, even when the device is bent to the point of a bending radius of 5 mm.

# 7 Conclusion

The focus of the presented thesis was the photo physical and electro optical investigation of two novel blue emitting polyfluorenes and their application in multi layer OLEDs. Before assembling the multi layer OLED, the polyfluorenes and their properties were thorough investigated.

The first of the two investigated polyfluorenes – fluorinated polyfluorene (fPF) – exhibited fluorine containing side chains, which made it possible to dissolve the polymer in fluorinated solvents. For the experiments, the fluorinated solvents $\alpha,\alpha,\alpha$-trifluoren (TFT) and hexafluorobenzene were used. The photo physical investigations concerning the absorbance and emission of fPF in solution and in film revealed unstructured absorption spectra with peak maxima at 386 nm (in solution) and 388 nm (in film). The photoluminescence spectrum of fPF in solution displayed a main peak at 412 nm, with vibronic replica at 435 nm and in film the spectrum had its maximum at 420 nm and a vibronic fine structure at 446 nm.

Measurements to determine the stability of the fPF EL spectrum with respect to thermal stress and UV irradiation were performed. When heating (100°C) the film under ambient conditions, a strong intensity enhancement at 540 nm was evident. Due to the fact that there is no significant spectral change when heating the film in argon, the origin of this spectral feature could be traced back to a so called Keto defect (a photo- (or electro-) oxidative degradation process). After exposure to UV irradiation, no significant change in the spectrum was detected. The measurement of the photoluminescence quantum yield of fPF in solution revealed a value of 99%. Even though the photoluminescence quantum yield was high, the single layer OLED with fPF as active layer showed poor luminance and efficiency values (7,68 cd/m$^2$; $8 \cdot 10^{-4}$ cd/A). By increasing the fPF layer thickness, an enhancement of the luminance and efficiency was achieved (257 cd/m$^2$; 0,177 cd/A).

For the first approach of assembling multi layer OLEDs, the blue emitting fPF was combined with an already determined (commercially available) red emitting polymer (MEHPPV) to enable the possibility of a color switch. Different electrode materials and thicknesses of the fPF layer were investigated. Using aluminum as top electrode material and a thick fPF layer (55 nm), a huge color switch was distinguishable by changing the applied voltage. Further investigations revealed that the origin of the color switch was the degradation of the polymer layers during operation. However, the fabrication of the multi layer devices by solution based manufacturing was quiet successful, only light dissolving (about 10 %) of the MEHPPV layer during the fPF spin coating process was observable, but due to degradation process, the color shift was not reversible.

The second approach of assembling multi layer OLEDs was to combine fPF with an already determined (commercially available) blue emitting electro active polymer (HTP) in a bilayer structure, with the target to achieve an enhancement of the device efficiency. It was successfully demonstrated that the multi layer device showed an enhancement of the device efficiency of about 35 % compared to the fPF single layer device. In addition, a blend system (mixture ration of fPF and HTP: 1:1) was fabricated to investigate if HTP can be used to improve the charge

transport in the light emitting layer and therefore to increase the efficiency or if a possible FRET between the fPF and HTP molecules can have a positive effect to the device efficiency, but an enhancement of the efficiency and luminance was not achieved.

The second investigated novel polymer was PEGylated polyfluorene (PEGPF) which was soluble in methanol (MeOH). Photo physical investigations concerning the absorbance and emission were performed. The measured absorption spectra showed a peak maximum at 402 nm (in solution) and 400 nm (in film), respectively. The PL spectrum of PEGPF in solution displayed a peak at 425 nm with a vibronic replica at 448 nm and in film, the spectrum had its maximum at 420 nm and a vibronic fine structure at 450 nm. The determination of the photoluminescence quantum yield of PEGPF in solution revealed a value of 106 %, where an error of about 10 % has to be considered. The device efficiency of the PEGPF single layer devices was low ($\leq$ 0,04 cd/A), but the luminance values reached acceptable values in the range of 300 cd/m$^2$.

For multi layer assembling, an already determined and commercially available blue emitter polymer (PIF) was combined with PEGPF with the target to increase the device efficiency. Two different assemblies of multi layer systems were fabricated and investigated: ITO/PEDOT:PSS/ PIF/PEGPF/Ca/Al and ITO/PEDOT:PSS/PIF/PEGPF/TPBi/Ca/Al. The multi layer device without a TPBi layer showed the highest luminance and efficiency of all assembled single and multi layer OLEDs (4.912 cd/m$^2$; 0,824 cd/A). In comparison to the PIF single layer device, the multi layer device exhibited an efficiency enhancement of about 30%. A 3D AFM height image of the surface of the multi layer device revealed in all probability an incomplete film formation of the PEGPF layer. Considering the good results concerning the device efficiency even with a non-homogeneous PEGPF film, it clearly indicates an immense potential of the multi layer devices.

A further topic of this thesis was the manufacturing and investigation of ITO free flexible OLEDs. Instead of the often used indium tin oxide (ITO), the combination of a 8 nm thick gold layer coated with a high conductive PEDOT:PSS (HC-PEDOT:PSS) layer was used as transparent bottom electrode. To be able to compare the performance of the device, two further flexible OLEDs – one with a HC-PEDOT:PSS layer and one with an ITO layer as bottom electrode – were investigated. The HC-PEDOT:PSS layer without a gold layer did not achieve the necessary conductivity for satisfying device operation. Very high voltages (onset voltage ~18 V) had to be applied to detect an EL signal. Using ITO as bottom electrode, the OLEDs showed a much lower onset voltage of 3,8 V, but during operation, a fast degradation was determined. The flexible OLED with a 8 nm gold layer coated with HC-PEDOT:PSS as bottom electrode displayed a device current density similar to the current density shown by the flexible OLED with an ITO electrode. This was an indication that the conductivity of the bottom electrode was high enough. Concerning mechanical stress, the OLED impressed with a stable operation, even when the device was bent (bending radius of 5 mm). Due to the promising results of the device with the gold and HC-PEDOT:PSS layer, this transparent electrode configuration may be considered as an alternative to the expensive ITO.

# 8  Appendix

Within the development and design of OLEDs, shown in chapter 5, several device configurations were tested to optimize the device efficiency. For reasons of clarity, not all the detailed information on all manufactured OLEDs was listed, but only short statements about the configurations leading to poor performance were made. In this chapter, detailed results of those measurements are shown.

**Further investigations of single layer OLEDs with fluorinated polyfluorene**

As discussed in chapter 5.1.4, the first assembled single layer OLED using fPF as light emitting layer with the layer structure ITO/PEDOT:PSS/fPF(15nm)/Ca/Al, shows poor luminance and efficiency values (7,68 cd/m$^2$, $8 \cdot 10^{-4}$ cd/A). Blue emission is found (CIE 1931 x = 0,181 and y = 0,142) with a peak maximum at 419 nm. Performing a current sweep, a distinct change of the emission spectrum is determined when increasing the device current, leading to an undesired greenish-blue emission. In Figure 8.1, on the left side, the IV characteristic and on the right side, the current sweep measurement is shown. Table 8.1 below lists the summarized results.
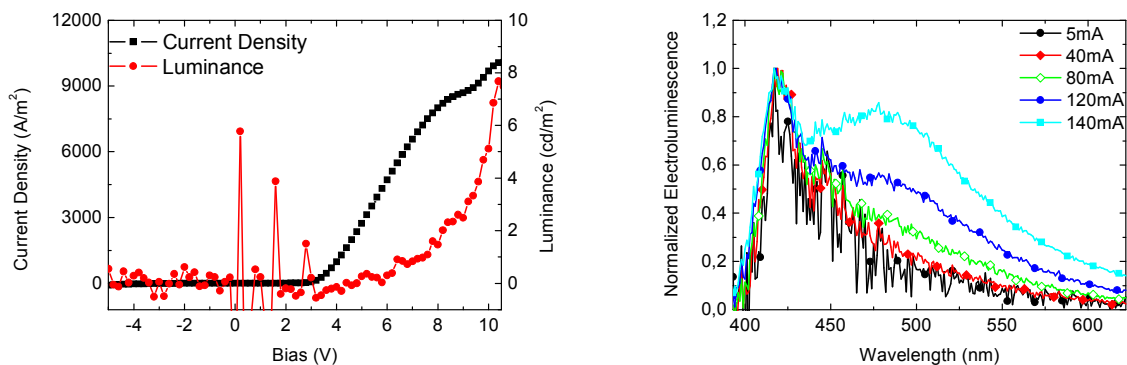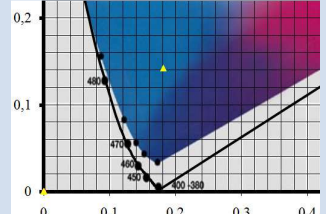


Figure 8.1: Current-voltage-luminance characteristic (left) and EL spectra (I-sweep; right) of the ITO/PEDOT:PSS/fPF(15 nm)/Ca/Al device.

Table 8.1: Key results of ITO/PEDOT:PSS/fPF (15 nm)/Ca/Al device.

| Onset voltage | Maximum efficiency | Maximum luminance | Peak maximum | CIE 1931 coordinates | CIE 1931 diagram |
|---|---|---|---|---|---|
| ~3,8 V | $8 \times 10^{-4}$ cd/A | 7,68 cd/m$^2$ | 419 nm | x = 0,181 <br> y = 0,142 <br> (@ 6 V) |  |

An attempt to improve the performance of the OLED by adding an ETL (TPBi) shows only a small enhancement of the OLED performance. The efficiency increases from $8 \cdot 10^{-4}$ to 0,012 cd/A and the luminance shows an enhancement from 7,68 to 27,72 cd/m$^2$. Blue emission is found (CIE 1931 x = 0,189 and y = 0,170) with a peak maximum at 421 nm. Figure 8.2 depicts the IV characteristic and the emission spectra at different operation currents. Table 8.2 shows a summary of the measurement results.



Figure 8.2: Current-voltage-luminance characteristic (left) and EL spectra (I-sweep; right) of the ITO/PEDOT:PSS/fPF(15 nm)/TPBi/Ca/Al device.

Table 8.2: Key results of ITO/PEDOT:PSS/fPF (15 nm)/TPBi/Ca/Al device.

| Onset voltage | Maximum efficiency | Maximum luminance | Peak maximum | CIE 1931 coordinates | CIE 1931 diagram |
|---|---|---|---|---|---|
| ~2,9 V | 0,012 cd/A | 27,72 cd/m$^2$ | 421 nm | x = 0,189 <br> y = 0,170 <br> (@ 5 V) |  |

By changing the spin parameter (new parameter: 1000 rpm for 480 s, ramp 9), the thickness of the fPF layer increases to 29 nm. The efficiency of the assembled OLED reaches a value of 0,011 cd/A and a luminance of 31,58 cd/m$^2$ is determined. Blue emission is found (CIE 1931 x = 0,190 and y = 0,177) with a peak maximum at 421 nm. Figure 8.3 depicts the IV characteristic and the emission spectra at different operation currents. Table 8.3 shows a summary of the measurement results.
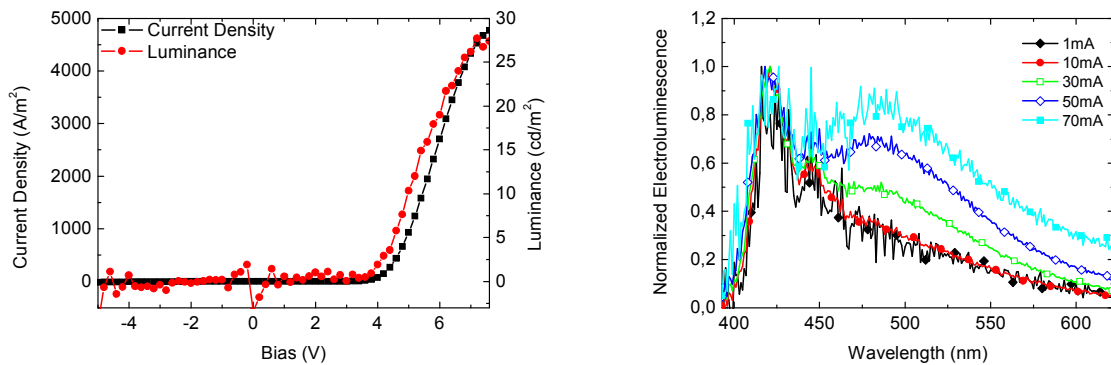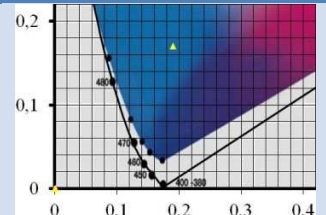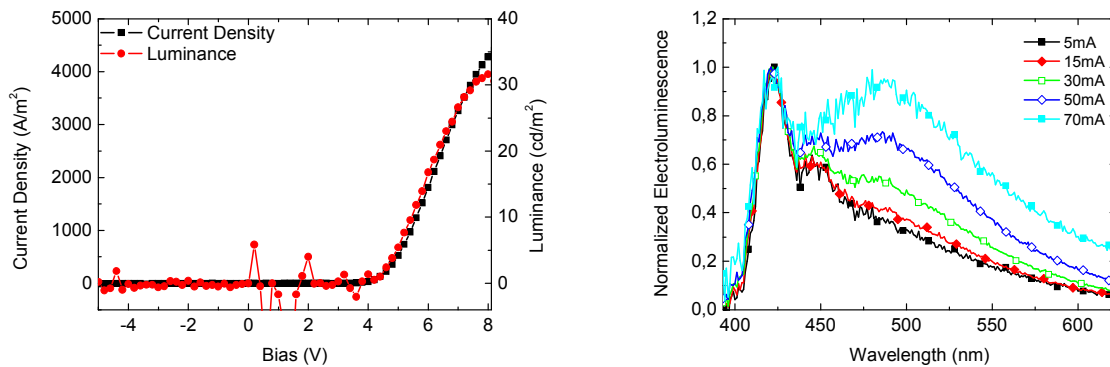


Figure 8.3: Current-voltage-luminance characteristic (left) and EL spectra (I-sweep; right) of the ITO/PEDOT:PSS/fPF(29 nm)/TPBi/Ca/Al device.

Table 8.3: Key results of ITO/PEDOT:PSS/fPF (29 nm)/TPBi/Ca/Al device.

| Onset voltage | Maximum efficiency | Maximum luminance | Peak maximum | CIE 1931 coordinates | CIE 1931 diagram |
|---|---|---|---|---|---|
| ~4,2 V | 0,011 cd/A | 31,58 cd/m$^2$ | 421 nm | x = 0,190 y = 0,177 (@ 5 V) |  |

# 9 Referees

[1] W. Mehl and B. Funk, "Dark injection of electrons and holes and radiative recombination in anthracene with metallic contacts," Phys. Lett. 25, 364 (1967).

[2] W. Helfrich and W. G. Schneider, "Recombination radiation in anthracene crystals," Phys. Rev. Lett. 14, 229 (1965).

[3] H. Shirakawa, E. J. Louis, S. C. Gau, Alan G. MacDiarmid, H. Shirakawa, E. J. Louis, S. C. Gau, and Alan G. MacDiarmid, "Electrical Conductivity in Doped Polyacetylene," Phys. Rev. Lett. 39, 1098 (1977).

[4] "Nobelprize.org," [Online]. Available: http://www.nobelprize.org/nobel_prizes/chemistry/laureates/2000/shirakawa-lecture.html. [Accessed 28 03 2012].

[5] C. W. Tang and S. A. VanSlyke, "Organic electroluminescent diodes," Appl. Phys. Lett. 51, 913 (1987).

[6] J. H. Burroughes, D. D. C. Bradley, A. R. Brown, R. N. Marks, K. Mackay, R. H. Friend, P. L. Burns, and A. B. Holmes, "Light-emitting diodes based on conjugated polymers," Nat. 347, 539 (1990).

[7] "OLED-Info.com," 25 05 2011. [Online]. Available: http://www.oled-info.com/universal-display-pholed-performance-chart-sid-2011. [Accessed 28 07 2011].

[8] "Wikipedia Picture," [Online]. Available: http://en.wikipedia.org/wiki/Atomic_orbital. [Accessed 06 10 2011].

[9] R. Trattnig, Organic Light Emitting Devices based on Phosphorescent Organometallic Complexes in Blend- and Onchain Polymer Systems, Diploma Thesis, Graz University of Technology (2009).

[10] I. Fleming, Molekülorbitale und Reaktionen organischer Verbindungen, Wiley-VCH, Weinheim (2012).

[11] "Teachers' Instructional Graphics Educational Resource," [Online]. Available: http://www.dlt.ncssm.edu/tiger/diagrams/bonding/Molecular_1s_orbitals-1.jpg. [Accessed 05 04 2012].

[12]   Peter W. Atkins and Jo A. Beran, Chemie: einfach alles, 2. Auflage, VCH Verlagsgesellschaft mbH, Weinheim (1996).

[13]   F. Neuflinger, O. Urban and M. Viehhauser, Chemie 1: Allgemeine und anorganische Chemie, 5. Auflage, Bohmann Verlag, Wien (1998).

[14]   "Università degli Studi di Firenze," [Online]. Available: http://www.scibio.unifi.it/triennali/firenze_3/legame/images/sigma-bond.jpg. [Accessed 06 10 2011].

[15]   "TutorVista.com," [Online]. Available: http://images.tutorvista.com/content/atomic-structure/bonding-p-molecular-orbitals.jpeg. [Accessed 06 10 2011].

[16]   "Wikipedia Picture," [Online]. Available: http://upload.wikimedia.org/wikipedia/commons/b/b8/Trans-Polyacetylene.svg. [Accessed 12 01 2012].

[17]   "Wikipedia Picture," [Online]. Available: http://upload.wikimedia.org/wikipedia/commons/thumb/b/ba/Pentacene_acsv.svg/800px-Pentacene_acsv.svg.png. [Accessed 16 01 2012].

[18]   S. Schuh, "Conjugated Polymer Heterostructure Based Light Emitting Diodes," Bachelor Thesis, Graz University of Technology (2009).

[19]   "Wikipedia Picture," [Online]. Available: http://upload.wikimedia.org/wikipedia/commons/4/48/Benzol.png. [Accessed 07 10 2011].

[20]   "University of Calgary - Department of chemistry," [Online]. Available: http://www.chem.ucalgary.ca/courses/351/Carey5th/Ch11/ch11-4-1.html. [Accessed 07 04 2012].

[21]   "Theoretischen Chemie der Universität Bonn," [Online]. Available: http://www.thch.uni-bonn.de/tc/teaching/tc1/downloads/TC_I_2011/Teil06.pdf. [Accessed 06 04 2012].

[22]   Hermann Haken and Hans C. Wolf, Molekülphysik und Quantenchemie, 5. Auflage, Springer, Berlin Heidelberg New York (2006).

[23]   "Globe of herbs," [Online]. Available: http://www.globeofherbs.com/supplement/beta-carotene/. [Accessed 26 11 2011].

[24]   C. Kittel, Einführung in die Festkörperphysik, 14. Auflage, Oldenbourg Wissenschaftsverlag GmbH, München (2005).

[25]  Lüdecke, Lüdecke, Thermodynamik: Physikalisch-chemische Grundlagen der thermischen Verfahrenstechnik, Springer-Verlag, Berlin Heidelberg (2000).

[26]  "Prinzip des Peierls-Isolators," [Online]. Available: http://www.physik.uni-wuerzburg.de/EP4/teaching/SS09/FOKUS/Hipke_MIT.pdf. [Accessed 28 11 2011].

[27]  C. Winder, Sensitization of Low Bandgap Polymer Bulk Heterojunction Solar Cells, Diploma Thesis, University of Linz (2001).

[28]  H. S. Nalwa, Handbook of Advanced Electronic and Photonic Materials and Devices, Academic Press, San Diego (2001).

[29]  Robert Morrison and Robert Boyd, Organic Chemistry, 5th edition, Prentice Hall of India (1989).

[30]  "IUPAC GOLDBOOK," [Online]. Available: http://goldbook.iupac.org/R05333.html. [Accessed 10 04 2012].

[31]  S. Nau, Efficiency and Stability of Poly(indenofluorene)-based Homo- and Copolymers, Master Thesis, Graz Univerity of Techology (2011).

[32]  E. Zojer, Electronic Structure and Nature of Excitation Processes in Conjugated Organic Materials - Theoretical Concepts and Experimental Studies, Dissertation, Graz University of Technology (1999).

[33]  A. Kammoun, Organische Leuchtdioden aus Polymeren und niedermolekularen Verbindungen für großflächige OLED-Anzeigen, 1. Auflage, Cuvillier Verlag, Göttingen (2008).

[34]  J. S. Wilson, A. S. Dhoot, A. J. A. B. Seeley, M. S. Khan, A. Köhler and R. H. Friend, Spin-dependent exciton formation in pi-conjugated compounds, Nat. 413, 828 (2001).

[35]  M. Wohlgenannt, Kunj Tandon, S. Mazumdar, S. Ramasesha and Z. V. Vardeny, "Formation cross-sections of singlet and triplet excitons in pi-conjugated polymers," Nat. 409, 494 (2000).

[36]  Yong Cao, Ian D. Parker, Gang Yu, Chi Zhang and Alan J. Heeger, "Improved quantum efficiency for electroluminescence in semiconducting polymers," Nat. 397, 414 (1999).

[37]  Z. Shuai, D. Beljonne, R. J. Silbey, and J. L. Brédas, "Singlet and Triplet Exciton Formation Rates in Conjugated Polymer Light-Emitting Diodes," Phys. Rev. Lett. 84, 131 (2000).

[38] M. Graber, Weitreichender Elektronentransfer in biologischen Systemen, Dissertation, University of Basel (2008).

[39] R. A. Marcus, "On the Theory of ElectronTransfer Reactions. VI. Unified Treatment for Homogeneous and Electrode Reactions," J. Chem. Phys. 43, 679 (1965).

[40] "Delaware Mineralogical Society," [Online]. Available: http://www.delminsociety.net/motm/images/images_mar2007/Jablonski_energy_diagram.j pg. [Accessed 13 10 2011].

[41] L. Bergmann and C. Schaefer, Festkörper, 2 Auflage, Walter de Gruyter, Berlin New York (2005).

[42] H. Mustroph and S. Ernst, "Das Franck-Condon-Prinzip," Chem. Unserer Zeit, 45, 256 (2011).

[43] M. Gaal, Conjugated polymer optoelectronic devices: Imprinted lasers by means of soft lithography and blue stable light emitting devices, Diploma Thesis, Graz University of Technology (2003).

[44] G. Heimel, M. Daghofer, J. Gierschner, E. J. W. List, A. C. Grimsdale, K. Müllen, D. Beljonne, J. Brrédas, E. Zojer, "Breakdown of the mirror image symmetry in the optical absorption/emission spectra of oligo(para-phenylene)s," J. Chem. Phys. 122, 054501-1 (2005).

[45] B. Wardle, Principles and Applications of Photochemistry, 1st edition, John Wiley & Sons, Chichester (2009).

[46] J. R. Lakowicz, Principles of Fluorescence Spectroscopy, 3rd edition, Springer Science+Business Media, New York (2006).

[47] P. Suppan, Chemistry and light, The Royal Society of Chemistry, Chambridge (1994).

[48] T.-R. Park, "Photoluminescence quenching by phonons and polarons in sodium cryptand sodide," Solid State Commun. 91, 949 (1994).

[49] R. Plessow, Entwicklung und Charakterisierung einer Methode zur Untersuchung von Makromolekülen mit Hilfe zeitaufgelöster laserinduzierter Fluoreszenz und Anregungs-Emissionsspektroskopie, 1. Auflage, Cuvillier Verlag, Göttingen (2004).

[50] Martin Pope, and Charles E. Swenberg, Electronic processes in organic crystals and polymers, Oxford University Press, New York Oxford (1998).

[51]  V. G. Kozlov, P. E. Burrows, G. Parthasarathy, and S. R. Forrest, "Optical properties of molecular organic semiconductor thin films under intense electrical excitation," Appl. Phys. Lett. 74, 1057 (1999).

[52]  E. J. W. List, U. Scherf, K. Müllen, W. Graupner, C.- H. Kim, and J. Shinar, "Direct evidence for singlet-triplet exciton annihilation in pi-conjugated polymers," Phys. Rev. B 66, 235203-1 (2002).

[53]  V. M. Agranovich, "Theory of Excitons," Nauka, Russia (1968).

[54]  Markus Sauer, Johan Hofkens, and Jörg Enderlein, Handbook of Fluorescence Spectroscopy and Imaging, Wiley-VCH Verlag & Co., Weinheim (2011).

[55]  Bergmann and Schaefer, Gase, Nanosysteme, Flüssigkeiten, 2. Auflage, Walter de Gruyter GmbH & Co. KG, Berlin (2006).

[56]  G. Kaune, Röntgenografische Charakterisierung von Indium-Zinn-Oxid-Dünnschichten, Diploma Thesis, University of Technology Chemnitz (2005).

[57]  Jiao Li, Juncheng Liu, Congjie Gao, Jinling Zhang, and Hanbin Sun, "Influence of MWCNTs Doping on the Structure and Properties of PEDOT:PSS Films," Int. J. of Photoenergy 2009, Article ID 650509 (2009).

[58]  H. Scheiber, Structure To Property Relationships in Blue Light Emitting Conjugated Polymers, Dissertation, Graz University of Technology (2008).

[59]  Rico Meerheim, Mauro Furno, Simone Hofmann, Björn Lüssem, and Karl Leo, "Quantification of energy loss mechanisms in organic light-emitting diodes," Appl. Phys. Lett. 97, 253305-1 (2010).

[60]  W. Demtröder, Experimentalphysik 3, 4. Auflage, Springer-Verlag, Berlin Heidelberg (2010).

[61]  Stefan Sax, Nicole Rugen-Penkalla, Alfred Neuhold, Sebastian Schuh, Egbert Zojer, Emil J. W. List, and Klaus Müllen, "Effcient blue light emitting polymer heterostructure devices: The fabrication of ion and defect free multilayer structures from orthogonal solvents," Adv. Mater. 22, 2087 (2010).

[62]  Shin-Rong Tseng, Hsin-Fei Menga, Chi-Hung Yeh, Huan-Chung Lai, Sheng-Fu Horng, Hua-Hsien Liao, Chain-Shu Hsu, Li-Chi Lin, "High-efficiency blue multilayer polymer light-emitting diode fabricated by a general liquid buffer method," Synthetic Met. 158, 130 (2008).

[63]  S. Sepeur, Nanotechnologie, Vincentz Network GmbH & Co. KG, Hannover (2008).

[64]  "Krüss - Advancing Surface Science," [Online]. Available:
      http://www.kruss.de/de/theorie/messungen/kontaktwinkel/modelle/equation-of-state.html.
      [Accessed 17 05 2012].

[65]  "Wikipedia Picture," [Online]. Available:
      http://upload.wikimedia.org/wikipedia/commons/0/04/Beer_lambert.png. [Accessed 2011
      11 22].

[66]  J. M. Hollas, Modern spectroscopy, 4th edition, John Wiley & Sons, Chichester (2004).

[67]  J. E. Cantle, Atomic absorption spectrometry, Elsevier Scientific Publishing Company,
      Amsterdam (1982).

[68]  "Recording Fluorescence Quantum Yields," [Online]. Available:
      http://www.horiba.com/us/en/scientific/products/fluorescence-spectroscopy/application-
      notes/quantum-yields/. [Accessed 23 11 2011].

[69]  H. L. Hartman, SME Mining Engineering Handbook, 2nd edition, Society for Mining
      Metal (1992).

[70]  "WolframAlpha," [Online]. Available:
      http://www.wolframalpha.com/input/?i=surface+tension+of+%CE%B1%2C%CE%B1%2
      C%CE%B1-Trifluorotoluene&a=ClashPrefs_*Chemical.Alpha%2CAlpha%2CAlpha
      Trifluorotoluene.ChemicalProperty.SurfaceTension-. [Accessed 22 01 2012].

[71]  "Surface tension values of some common test liquids for surface energy analysis,"
      [Online]. Available: http://www.surface-tension.de/. [Accessed 22 01 2012].

[72]  U. Scherf and D. Neher, Polyfluorenes, Springer-Verlag, Berlin Heidelberg (2008).

[73]  "Wikipedia Picture," [Online]. Available:
      http://en.wikipedia.org/wiki/File:Benzotrifluoride.png. [Accessed 15 09 2011].

[74]  "Wikipedia Picture," [Online]. Available:
      http://en.wikipedia.org/wiki/File:Hexafluorobenzene.svg. [Accessed 15 09 2011].

[75]  Stefan Kappaun, Christian Slugovc and Emil J. W. List, "Optically Active Chemical
      Defects in Polyfluorene-Type Polymers and Devices," Adv. Polym. Sci. 212, 273 (2008).

[76]   Emil J. W. List, Roland Guentner, Patricia Scanducci de Freitas, and Ullrich Scherf, "The Effect of Keto Defect Sites on the Emission Properties of Polyfluorene-Type Materials," Adv. Mater. 14, 374 (2002).

[77]   V. Bulovic, V. B. Khalfin, G. Gu, and P. E. Burrows, "Weak microcavity effects in organic light-emitting devices," Phys. Rev. 58, 3730 (1998).

[78]   A. Dodabalapur, L. J. Rothberg, R. H. Jordan, T. M. Miller, R. E. Slusher, and Julia M. Phillipse, "Physics and applications of organic microcavity light emitting diodes," J. Appl. Phys. 80, 6954 (1996).

[79]   "starkeffects.com," [Online]. Available: http://www.starkeffects.com/images/fabry-perot-basic.gif. [Accessed 13 01 2012].

[80]   S. Schuh, unpublished results, Graz University of Technology (2009).

[81]   Jin-Kyun Lee, Hon Hang Fong, Alexander A. Zakhidov, Georgia E. McCluskey, Priscilla G. Taylor, Mitkel Santiago-Berrios, Héctor D. Abruna, Andrew B. Holmes, George G. Malliaras, and Christopher K. Ober, "Semiperfluoroalkyl Polyfluorenes for Orthogonal Processing in Fluorous Solvents," Macromolecules 43, 1195 (2010).

[82]   Robert K. Boyd, Cecilia Basic, and Robert A. Bethem, Trace Quantitative Analysis by Mass Spectrometry, John Wiley & Sons Ltd, Chichester (2008).

[83]   Craig Grimes, Gopal K. Mor, TiO2 Nanotube Arrays: Synthesis, Properties, and Applications, Springer Science+Business Media, New York (2009).

[84]   Lambert M. Surhone, Miriam T. Timpledon, and Susan F. Marseken, Pegylation, Vdm Verlag Dr. Müller, Saarbrücken (2010).

[85]   "Wikipedia Picture," [Online]. Available: http://en.wikipedia.org/wiki/File:Polyethylene_glycol.png. [Accessed 15 09 2011].

[86]   S. Schuh, unpublished results, NanoTecCenter Weiz Forschungsgesellschaft mbH (2010).

[87]   S. Nau, unpublished results, NanoTecCenter Weiz Forschungsgesellschaft mbH (2010).

[88]   "Rutherford - Lexicon der Elemente," [Online]. Available: http://www.uniterra.de/rutherford/ele049.htm. [Accessed 23 09 2011].

[89]   "ALL-MET, Informationen zu Edelmetallen und mehr," [Online]. Available: http://www.all-met.info/indium_.html. [Accessed 23 09 2011].